博士論文

Effect of Surface Oxidation in Cesium Chemisorption onto Nuclear Structural Materials

(原子炉構造材料へのセシウム化学吸着における表面酸化の影響)

I Wayan Ngarayana

Nuclear Material and Maintenology Laboratory
Energy and Environmental Science
School of Engineering
Nagaoka University of Technology
2022

(This page intentionally left blank)

Declaration by student

I hereby declare that the work presented herein is original work done by me and has not been published or submitted elsewhere for the requirement of a degree program. Any literature or work done by others and cited in this dissertation has been acknowledged and listed in the bibliography section.

Nagaoka, June 2022

I Wayan Ngarayana
Nuclear Material & Maintenology Laboratory
Energy & Environmental Science
School of Engineering
Nagaoka University of Technology

(This page intentionally left blank)

Effect of Surface Oxidation in Cesium Chemisorption onto Nuclear Structural Materials

(原子炉構造材料へのセシウム化学吸着における表面酸化の影響)

A Dissertation

Submitted in partial fulfillment for the Ph.D. degree in engineering to the department of Energy and Environmental Science, School of Engineering, Nagaoka University of Technology

By

I Wayan Ngarayana

(S17508081)

Nagaoka University of Technology

Date

June 2022

Supervisor

Tatsuya Suzuki

Advisor

Kenta Murakami

(This page intentionally left blank)

Effect of Surface Oxidation in Cesium Chemisorption onto Nuclear Structural Materials

(原子炉構造材料へのセシウム化学吸着における表面酸化の影響)

Abstract

This study examines the effect of surface oxidation in Cs chemisorption onto modern nuclear structural materials. The examination is conducted using 4 types of materials; SS 304, SS 321, Inconel 600, and X-750 by following a liquid-solid reaction to simulate leakage parts to the environment. Although these materials have a similar oxide film during normal operation, matrix composition differences and temperature changes during severe accidents may alter their oxide structures which may contribute to the Cs chemisorption behavior. The diverse pre-oxide films are prepared from well-polished SS 304, SS 321, Inconel 600, and X-750 specimens following annealing procedures. The pre-oxide specimens are coated with liquified $CsOH\cdot(H_2O)_x$ and treated at 300–1050 ^{o}C in the air, then soaked in water. Water-soluble Cs_2FeO_4 and Cs_2CrO_4 are identified from pre-soaked specimens. Analytical identification confirms that Cs_2FeO_4 decomposes to be $CsFeO_{2.5}$ in a high pH environment. However, $CsFeO_{2.5}$ could react with Cr_2O_3 to form a more stable Cs_2CrO_4. Well-chemisorbed Cs-Al-Ti-Si-O compounds could be identified from post-soaked specimens. The formation of Cs-Si-O compounds in the deeper part of the oxide layer is observed but never be formed on or below the Cr-rich layer. This study concludes that oxidation, solute Al, Ti & Si, and Cs chemisorption have a triangle relationship. Solute Al, Ti & Si could enhance the oxidation resistance of stainless steels and Ni-based alloys and tend to react with Cs to form stable compounds which could be well-chemisorbed. Oxidation resistance improvement reduces the interaction between CsOH precursor with the oxide film and holds the outer oxide growth mechanism which could bury chemisorbed Cs compounds in deeper parts of the oxide film.

Keywords: cesium, retention, chemisorption, SS 304, SS 321, Inconel 600, X-750, solute elements, oxidation.

(This page intentionally left blank)

Acknowledgments

I would like to express my sincere gratitude to my advisor, Prof. Kenta Murakami, and my supervisor, Prof. Tatsuya Suzuki who led me to do the experiment presented in this dissertation. Many thanks to Dr. Thi Mai Dung Do for a lot of advice and experimental procedure improvement. Without them, this manuscript will not be completed properly.

I am grateful to all professors, especially those who engage with Nuclear System Safety Engineering Department such as Tsuneo Suzuki, Suematsu Hisayuki, Kazuhiko Takase, Weihua Jiang, Yuichi Otsuka, Hironori Katagiri, Ohta Tomoko, and many more that cannot be mentioned one by one. Special thanks also to Prof. Sato Isamu from Tokyo City University for the advice from the mid-term to the final presentations. My sincere gratitude to Dr. Shoji Takada, Dr. Etsuo Ishitsuka, and all members of the High Temperature Engineering Test Reactor (HTTR) department, Japan Atomic Energy Agency (JAEA), that have given their support, help, and opportunity to learn HTGR technology more deeply during my internship program. All of them have provided me with a lot of knowledge and experimental skill improvement which are very useful in the preparation of this dissertation as well as for my personal life and future career.

I am grateful to my senior, Dr. Luu Vu Nhut and Dr. Phornsakorn Prak Tom who teach me to use Focus Ion Beam (FIB), Nguyen Ba Vu Chinh, Dr. Chu Minh Ngo, and other colleagues in Nuclear Material and Maintenology Laboratory, who given support and help.

Last but not least, I would like to express my sincere appreciation to my beloved parents, my little family, brothers and sisters, colleagues, and friends for encouraging and supporting me throughout my study.

(This page intentionally left blank)

Announcement of Publication Related to This Manuscript

The contents of this manuscript are related to my previous academic activities including article publication, and presentations both oral and poster at several events while studying at the Nagaoka University of Technology. Because of that, some ideas, images, tables, and writing style duplication occur in several parts of this manuscript. These academic activities are listed below:

Conference activities:

1. I Wayan Ngarayana, Kenta Murakami, et al., Nuclear Power Plant Maintenance Optimization: Models, Methods & Strategies, Symposium of Emerging Nuclear Technology and Engineering Novelty, 4-5 July 2018. (Oral Presentation).
2. I Wayan Ngarayana & Kenta Murakami, High Temperature Gas Cooled Reactor Regulation Development – Operation & Maintenance Perspective, GIGAKU Conference, 5 – 6 October 2018. (Poster Presentation).
3. I Wayan Ngarayana & Kenta Murakami, Fuzzy FMEA Expert Judgment Methodology Development to Support HTGR Regulation, The Second 2019 Fukushima Research Conference (FRC), 10 – 12 July 2019. (Poster Presentation).
4. I Wayan Ngarayana & Kenta Murakami, Graded Approach Establishment for HTGR Maintenance Activities Using Modified Fuzzy FMEA & Expert Judgment Methodology, International Conference on Emerging Nuclear Energy Systems, 6 – 9 October 2019. (Oral Presentation).
5. I Wayan Ngarayana, Kenta Murakami, & Thi-Mai Dung Do, Cesium Chemisorption Phenomenon onto Ni-based Alloys Material, AESJ Student Network, 17 September 2020 (Poster Presentation).
6. I Wayan Ngarayana, Kenta Murakami, & Thi-Mai Dung Do, Oxidation-related Cesium Chemisorption onto Reactor Coolant Boundaries Materials, AESJ Annual Meeting, 17-19 March 2021 (Oral Presentation).
7. I Wayan Ngarayana, Kenta Murakami, & Thi-Mai Dung Do, Cesium Retention Mechanism Related to Oxidation of Reactor Coolant Boundaries Materials, ICONE28, 4-6 August 2021. (Oral Presentation).

8. I Wayan Ngarayana, Kenta Murakami, & Thi-Mai Dung Do, Effect of Titanium on Cs Chemisorption of Stainless Steel, AESJ Fall Meeting, 8-10 September 2021. (Oral Presentation).

Publications:

公表の方法及び時期 Main Publication:

1. 査読中, Journal of Nuclear Science and Technology, "Role of Solute Titanium and Oxidation to the Cesium Chemisorption onto Stainless Steels", (I Wayan Ngarayana, Kenta Murakami, Tatsuya Suzuki, Thi-Mai-Dung Do).
2. 2022, Journal of Nuclear Science and Technology, DOI: 10.1080/00223131.2022.2029608, "Effect of surface oxidation on the cesium chemisorption behavior of SS 304, Inconel 600 and X-750", (I Wayan Ngarayana, Kenta Murakami, Thi-Mai-Dung Do).
3. 2019, Journal of Physics: Conf. Series 1198 (2019) 022005, doi:10.1088/1742-6596/1198/2/022005, pp. 022005 "Nuclear Power Plant Maintenance Optimization: Models, Methods & Strategies", (I Wayan Ngarayana, Thi-Mai-Dung Do, Kenta Murakami, Masahide Suzuki).

参考論文 Associated Publications:

1. 2021, IOP Conference Series: Earth and Environmental Science, DOI: 10.1088/1755-1315/753/1/012038, Volume 753 pp. 012038, "Predicting the future of Indonesia: energy, economic and sustainable environment development", (I Wayan Ngarayana, Jepri Sutanto, Kenta Murakami).
2. 2020, Mechanical Engineering Journal, DOI:10.1299/jsmeicone.2019.27.2330, "Establishment of reasonable 2-D model to investigate heat transfer and flow characteristics by using scale model of vessel cooling system for HTTR", (Shoji Takada, I Wayan Ngarayana, Yukihiro Nakatsuru, Atuhiko Terada, Kenta Murakami, Kazuhiro Sawa).
3. 2020, ICENES (International Conference on Emerging Nuclear Energy Systems) Proceeding; (Committee also has a plan to publish the articles in Journal of Physic, Conference Series.). "Graded Approach Establishment for the HTGR

Maintenance Activities Using Modified Fuzzy FMEA & Expert Judgement Methodology", (I Wayan Ngarayana, Kenta Murakami).

4. 2018, Proceeding of Sein (National Seminar of Nuclear Energy Infrastructure) ISSN: 2621-3125 pp. 385-394 "Resilience Engineering, Management System and Leadership Spectrum Approach for the High-risk Organization", (I Wayan Ngarayana, Jepri Sutanto, Suzie Darmawati).
5. 2017, SENTEN Proceeding, ISSN: 2355-7524, pp. 12-13, "Preliminary Implementation of Standardization Based Nuclear Energy Clearing House: Case Study of Generation IV NPPs", (I Wayan Ngarayana, Sigit Santosa).
6. 2017, 12th Annual Meeting on Testing and Quality Standardization (AMTEQ), pp. 183-189, "Standardization as the Operational Basis of Nuclear Technology Clearinghouse", (I Wayan Ngarayana, Suzie Darmawati).

(This page intentionally left blank)

Contents

List of Figures

(This page intentionally left blank)

List of Tables

(This page intentionally left blank)

Abbreviations

Al	:	Aluminum
B	:	Boron
BWR	:	Boiling Water Reactor
C	:	Carbon
Cr	:	Chromium
CRDM	:	Control Rod Driving Mechanism
CREST	:	Chemical Reaction with Steel
Cs	:	Cesium
CVCS	:	Chemical and Volume Control System
EDS	:	Energy Dispersive Spectroscopy
Fe	:	Ferro (Iron)
FIB	:	Focus Ion Beam
FP	:	Fission Product
GCR	:	Gas-cooled Graphite Moderated Reactor
GFR	:	Gas-cooled Fast Reactor
HAXPES	:	Hard X-ray Photoelectron Spectroscopy
HTGR	:	High Temperature Gas Reactor
I	:	Iodine
IAEA	:	International Atomic Energy Agency
ICDD	:	International Centre for Diffraction Data
INL	:	Idaho National Laboratory
JAEA	:	Japan Atomic Energy Agency
K	:	Kelvin
kV	:	kilo Volt
LFR	:	Lead-cooled Fast Reactor
LWGR	:	Light Water-cooled Graphite Moderated Reactor
LWR	:	Light Water Reactor
Mn	:	Manganese
Mo	:	Molybdenum

MSR	:	Molten Salt Reactor
MW	:	Megawatt
MWe	:	Megawatt Electric
Ni	:	Nickel
NPP	:	Nuclear Power Plant
O	:	Oxygen
ODS	:	Oxide Dispersion Strengthened alloys
OM	:	Optical Microscope
ORNL	:	Oak Ridge National Laboratory
PHWR	:	Pressurized Heavy Water Reactor
PWR	:	Pressurized Water-cooled Reactor
RPV	:	Reactor Pressure Vessel
RT	:	Room Temperature (~25 °C)
SA	:	Severe Accident
SEM	:	Scanning Electron Microscopy
SFR	:	Sodium-cooled Fast Reactor
Si	:	Silicon
SS	:	Stainless Steel
SSC	:	Stress Corrosion Cracking
TEM	:	Transmission Electron Microscope
TeRRa	:	Test bench for Fission Product Release and tRansport
TG-DTA	:	Thermogravimetry – Differential Thermal Analysis
Ti	:	Titanium
XRD	:	X-ray Diffraction
ZAP	:	Quantitative EDS correction related to the effects of atomic number (Z), absorption (A), and fluorescence excitation (F)

Chapter 1

Introduction

The true sign of intelligence is not knowledge, but imagination.

~Albert Einstein

Chapter 1

Introduction

1.1 Background

Nuclear Power Plant (NPP) is one of the most reliable carbon-free energy suppliers (Zohuri and McDaniel, 2019, p. 135). NPP can compete directly with fossil-fueled power plants regarding their reliability, energy capacity, and cost of generation (Matsuo, Nagatomi, and Murakami, 2011). By the end of 2020, 393,241 MW of electric capacity had been generated from 443 in-operation NPPs around the world (IAEA, 2021). Climate change issues and the effort to reduce greenhouse gas emissions are predicted to give a positive trend to the electrical capacity of nuclear energy due to the construction of the new NPPs, particularly in some countries such as China and Arabian countries. British Petroleum estimated the energy mix from nuclear energy will grow by 5% in 2035 (BP, 2017).

Several nuclear accidents had been faced by modern mankind's society since the first artificial nuclear chain reaction at Chicago Pile No. 1 in 1942 (Koizumi, Okawa and Mori, 2021, p. 39). Some of the famous accidents such as the Three Mile Island in the USA (1979), the Chernobyl disaster (1986) in the Soviet Union, and the Fukushima Daiichi NPPs accident in Japan (2011) (Koizumi, Okawa and Mori, 2021, pp. 56–61). Nuclear accidents become very scary compared with other types of accidents because of their radiation and radioactive materials releases which could potentially endanger human health (Lewandowski, Co-investigator and Lewandowski, 2015, p. 323). Various efforts for NPP's safety improvement to reduce the accident probability and its severity are ongoing in many ways. Some of these ways, such as regulation strengthening, operation & maintenance enhancement, and the development of advanced technologies. Nevertheless, due to the nature of nuclear reactors which contain huge amounts of nuclear and radioactive materials, the utilization of nuclear energy always carries radiation risks. Radioactive materials which are commonly called source terms could be transported to unintended areas and potentially endanger the workers, public, and environment.

1.1.1 Role of Cs in Source Terms Transport

The source terms issues are scoping very wide areas starting from radioactive generation as the fission products (FPs) and/or activated elements, in-vessel & ex-vessel transport, up to the environment when the accident happens (Vogel, 1985). Source terms transport understanding is important both for accident contingency and preparedness, as well as the basis for the design and material selection, operation & maintenance, and during the decommissioning (Rainer Moormann, Werner Schenk, 2001; Brinkmann *et al.*, 2006; Moormann, 2008). Moreover, contingency and emergency preparedness for post-severe accidents can be optimized if appropriate source terms transport prediction can be made (Raimond *et al.*, 2013).

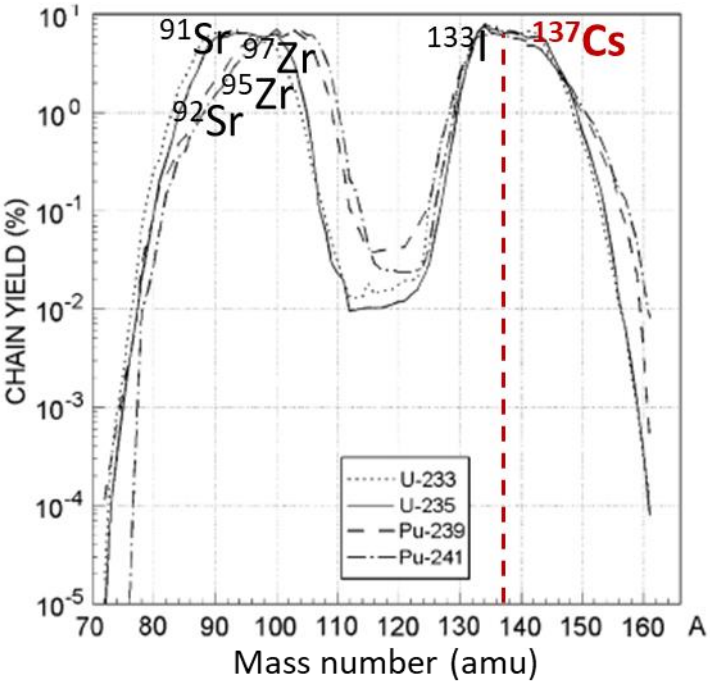

Figure 1.1 Fission products yield of U-233, U-235, Pu-239, and Pu-241.

The scope of in-vessel source terms transport is started from radioactive generation on the fuel matrix up to primary cooling system boundaries, coolant storage and/or purification system, and other related systems (Sehgal, 2012, pp. 90–178). Source terms generation is different for each type of reactor depending on several factors, such as type of fuel, burn up, neutron flux, etc. Each FP has a specific yield, or formation probability as shown in Figure 1.1 (Sehgal, 2012, p. 433). These FPs are generally categorized as gaseous (such as xenon, krypton, argon, oxygen, etc.) and non-gaseous

nuclides. The non-gaseous nuclides furthermore can be classified into volatile, semi-volatile, low-volatile, and non-volatile fission products (Sehgal, 2012, pp. 433–434). Some well-known volatile FPs in water-cooled reactors such as iodine, cesium, bromine, rubidium, tellurium, antimony, and silver. Together with noble gasses, volatile nuclides have a high possibility to migrate from the fuel matrix. Molybdenum, rhodium, barium, palladium, and technetium are classified as semi-volatile nuclides because they have high levels of release but are chemically sensitive which increases their retention probability. Low-volatile nuclides such as strontium, yttrium, niobium, ruthenium, lanthanum, cerium, and europium with low but significant levels of release, especially for high burn-up fuels. Meanwhile, non-volatile nuclides such as zirconium, neodymium, and praseodymium have very low release probabilities.

Source terms volatility vary depending on the type of reactor. In the case of High Temperature Gas-cooled Reactor (HTGR), ^{3}H, ^{14}C, Ag, Sr, I, Cs, and Te are considered to be important source terms, although their release probability could be said much lower compared with water-cooled reactors (Kissane, 2009). HTGR could produce a very long life of ^{14}C radioactive due to a large amount of graphite structural materials in its core. ^{14}C could be released as the dust into the coolant and/or environment (Idaho National Laboratory (INL), 2010). The other type of reactors such as the Gas-cooled Fast Reactor (GFR) and the Sodium-cooled Fast Reactor (SFR) consider Cs, I, Pd, and Tc to be important source terms (Chersola, Lomonaco and Marotta, 2015; Pradeep *et al.*, 2016). Lead-cooled Fast Reactor (LFR) and Molten Salt Reactor (SMR) identified the significance of Xe, Kr, and Po, while Cs is estimated to be strongly retained in the coolant (Cinotti *et al.*, 2011; Mohsin, Qureshi and Ashfaq, 2019). Nevertheless, in the case of water and/or air ingress accident, Cs can interact with water causing the formation of CsOH which may be released into the environment (Rainer Moormann, Werner Schenk, 2001; Moormann, 2008; Kissane, 2009; Moormann and Hilpert, 2017; C. Li *et al.*, 2019).

Cs becomes one of the most important source terms because of its volatility, huge inventory, and long half-life (Roki *et al.*, 2008). Around 161 kg Cs isotopes especially dominated by ^{137}Cs with 30.1 years half-life are produced on the core of 900 MWe PWR just after shutdown. That makes it become the most radiotoxic element for the long period after the accident (Sehgal, 2012, p. 430). The release of Cs had been

identified mainly as CsI, CsOH, Cs_2MoO_4, Cs_2Te, etc. (Roki *et al.*, 2015; Moormann and Hilpert, 2017). The different formation of Cs compounds has been observed to change Cs volatility (Osaka *et al.*, 2016; Fidelma Giulia Di Lemma *et al.*, 2017; Miyahara *et al.*, 2019).

1.1.2 Cs Chemisorption Studies

Source terms particularly Cs transport, are generally modeled starting from the inventory prediction. Source terms inventory can be predicted based on the Bateman equation (Jeong and Chang, 2008). During normal operation, most source terms should be trapped in the fuel matrix. However, the rest could be released due to the defects of the fuel matrix. The source terms release is strongly influenced by other physical parameters such as temperature, oxidation-reduction, interactions with the cladding and structural elements, fuel burn-up, fuel type, and the other environmental conditions which correlate with the type of the reactor. A part of source terms could be absorbed and deposited on the cladding, fuel assembly, and/or other core structural materials, while the rest may migrate alongside the cooling system. Chemical and Volume Control System (CVCS) or the other system depending on the type of reactor, furthermore purifies the source terms from the coolant (Aggarwal, 1995, pp. 1–1; Hashemian, 2011). However, some of the source terms may be deposited and retained physically and/or chemically on the cooling boundaries materials. Source terms deposition may increase the radiation level and contribute to radiation safety, especially during maintenance and decommissioning activities. Appropriate design and material selection may reduce the source terms retention and decrease radiation levels during these activities.

Source terms transport mechanism changes drastically during the accident. In the case of LWR, when the temperature core reaches ~1000 K, Cs including some other source terms are released in gaseous phases (Brillant, Marchetto and Plumecocq, 2013). Gaseous chemical reactions could happen between source terms which then form certain compounds. A part of source terms may interact and be absorbed by the structural materials around the core in a high temperature environment. But the rest migrate to the cooler areas pushed by the convection flow of steam and/or coolant. Several mechanisms may happen to the source terms during the migration, affecting their particle's size to get bigger in the cooler areas. These mechanisms include the formation of supersaturated

vapors, nucleation, the form of aerosol, and agglomeration. Source terms may condensate to the structural material when reaching a supersaturated vapors environment. The other parts deposit on the cooler area after becoming relatively large size particles. These mechanisms furthermore are illustrated in Figure 1.1 (Sehgal, 2012, p. 457).

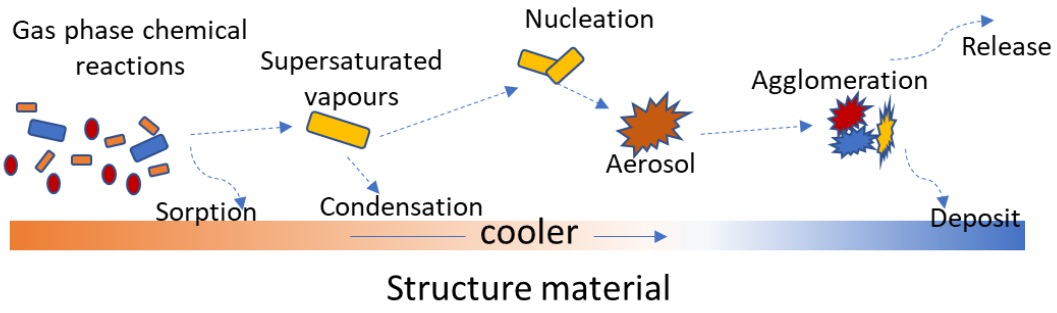

Figure 1.2 Source terms transport and interaction with structural materials.

Physical phenomena, including fluid and thermodynamics properties related to the source terms transport modeling as illustrated in Figure 1.2 have been well-established. Nevertheless, high uncertainty still exists due to the chemistry-related phenomena (JAEA, 2019). This happened because most available codes are made following the integral approaches (Klein-Heßling *et al.*, 2014) by simplifying the above physicochemical interaction. Therefore, a ton of work is being conducted to solve these chemistry-related phenomena. These interactions could produce new compounds and change their volatility. Some new compounds may become more volatile and easy to migrate (Knebel, Jokiniemi and Bottomley, 2019). Some of them may also become less volatile by being chemically deposited onto the structural material. These chemically deposited compounds furthermore are called chemisorption (Lind *et al.*, 2020).

As one of the most important source terms, Cs chemisorption phenomena following gas-solid reactions at high temperatures have been identified in a long history. Sandia National Laboratory reacted cesium hydroxide (CsOH) vapor with SS 304 at a temperature around 1000 ^{o}C by following a gas-solid reaction to simulate Light Water Reactor (LWR) Severe Accident (SA). That study showed cesium oxides are deposited in the oxide layer and predicted as $Cs_2Si_4O_9$ (Sallach and Elrick, 1985). A more realistic integral experiment using the Phébus facility simulating the near-real LWR SA phenomenon indicates the importance of Cs chemisorption on the FPs transport

mechanism (Haste, Payot, and Bottomley, 2013). Intensive research after the Fukushima accident reveals that minor elements in the reactor core, both from FPs as well as from the structural materials are affecting Cs chemisorption significantly. CREST (Chemical Reaction with Steel) experiment by evaporating CsOH onto SS 304 at around 615–1000 ^{o}C confirms that cesium chemisorption is related to the concentration of solute silicon (Si) (Nakajima *et al.*, 2018) (Nishioka *et al.*, 2019). Other studies that establish the relationship between Si concentration with cesium oxides are performed using Hard X-ray Photoelectron Spectroscopy (HAXPES) and SEM/EDS on the specimens treated at 800 ^{o}C (Kobata *et al.*, 2018). Experimental studies related to other elements, such as molybdenum (Mo) and boron (B) are also investigated. The effect of Mo in SS 316 is studied from 800–1000 ^{o}C under Ar/H_2 and 5% H_2O atmospheric environment. Mo-enriched Cs species are found deposited at 800 ^{o}C but re-vaporized at 1000 ^{o}C (F.G. Di Lemma *et al.*, 2017). By using TeRRa (Test bench for Fission Product Release and tRansport) apparatus in a high temperature environment, B is found could react with Cs forming low volatile compounds on the SS materials (Miwa *et al.*, 2020). These findings could improve SA code uncertainty nearly one order of magnitude smaller (JAEA, 2019) thus spurring the need for further experiments to find the other elements that may also contribute to the Cs transport. These findings raise awareness of the important role of structural materials and their constituent elements.

Although great improvements related to the source terms chemistry have been made, however, treatment related to the liquid-solid interaction, especially at low temperatures is still insufficient (Lind *et al.*, 2020). Liquid-solid interaction could happen when supersaturated Cs particles change into an aerosol (Sehgal, 2012) and then condensed as a liquid droplet (Mishra et al., 2019). The liquid droplet interaction with the structural materials is important, especially to simulate leak parts to the environment (Watanabe, Yamada, and Ohsaki, 2009) (Firnhaber *et al.*, 1996). Therefore, the work to explore chemistry aspects related to the liquid-solid interaction phenomenon is still widely questionable.

1.1.3 Nuclear Structural Materials

NPP is a massive structure that consists of wide varieties and millions of tons of materials, depending on the type of reactor. For example, the topmost material of land-based NPP

is concrete, while a floating NPP is iron-based alloys. A huge amount of graphite constructs the core of Gas and Light Water-cooled Graphite Moderated Reactors (GCR & LWGR), while similar materials could not be found in typical Boiling Water Reactor (BWR), Pressurized Water Reactor (PWR) as well as Pressurized Heavy Water Reactor (PHWR).

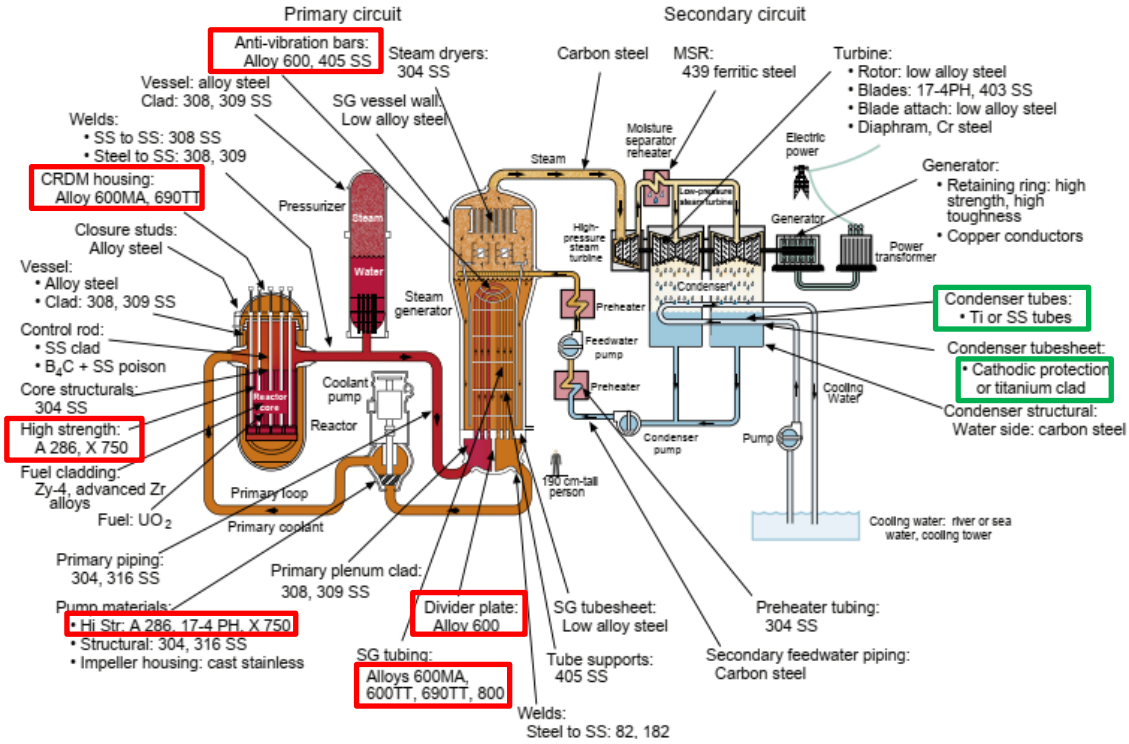

Figure 1.3 Alloys used for the structural material of typical PWR.

Concrete for land-based NPPs is composed of cement paste and aggregate. Cement pastes consist of 50-60% calcium silicate hydrates, 20% calcium hydroxide, and the rest are clinkers, ettringite, and pore structures. As a material taken from nature, aggregate contains elements that greatly vary depending on the source of excavation. However, aggregate is generally dominated by quartz (SiO_2), feldspars such as albite ($NaAlSi_3O_8$) and microcline ($KAlSi_3O_8$), and Al_2O_3, Fe_2O_3, CaO, MgO, etc. (Kaminski *et al.*, 2019).

Iron base alloys including carbon steel, galvanized iron, and Stainless Steel (SS) are the second-largest structural materials after concrete for typical 1000 MWe land-based PWR (Bryan and Dudley, 1974). In addition to being able to meet the established standards, iron is chosen because it is relatively cheap compared to other alloys (Hoffelner,

2013, p. 91). As reported by Oak Ridge National Laboratory (ORNL), a typical PWR is constructed of around 88.5% carbon steel, 5.6% SS, 3.4% galvanized iron, and the rest are nickel, copper, aluminum, brass, bronze, and other types of alloys (Bryan and Dudley, 1974). Carbon steels are used mainly as the Reactor Pressure Vessel (RPV) and piping materials. Several types of SS and Nickel base alloys as shown in Figure 1.3 are utilized on several systems, structures, and components (SSCs), especially around primary cooling system boundaries (Busby, 2019, p. 9). Up to 10 tons of aluminum is used for several components around the reactor core (Piippo T. Laitinen, 1997; Degueldre, 2017; Lumley, 2018), making the aluminum corrosion should be considered especially during loss of cooling accident (Chen *et al.*, 2008).

Table 1.1 Candidate materials for Generation IV Reactors.

Reactor	***F-M steel***	***Austenitic SS***	***ODS steel***	***Inconel***	***Graphite***	***Refractory***	***Ceramics***
GFR	P	P	P	P	-	P	P
Pb-LFR	P	P	S	-	-	S	S
MSR	-	-	-	P	P	S	S
SFR	P	P	P	-	-	-	-
SCWR	P	P	S	S	-	-	-
VHTR	S	-	-	P	P	S	P
Note: P = primary option, S = secondary option							

The requirement for safety improvement and the development of the advanced NPP, particularly generation IV and fusion reactor technologies with higher operating temperature and displacement damage, demand new structural materials (Yvon, 2017). The efforts for advanced materials development are ongoing all over the world by following several techniques such as matrix modification into austenitic phase by adding solute elements, the use of nickel-base alloys instead of iron, utilization of refractory alloys and intermetallic, the development of ceramics materials, and adding nano features such as Oxide Dispersion Strengthened alloys (ODS) (Hoffelner, 2013, pp. 82–83). In addition, there are several other considerations in material selection for advanced NPP, such as operating pressure, type of fuel & coolant, and corrosion rate. Based on these

considerations, the structural material candidates for future commercial generation IV NPPs are shown in Table 1.1 (Murty and Charit, 2008).

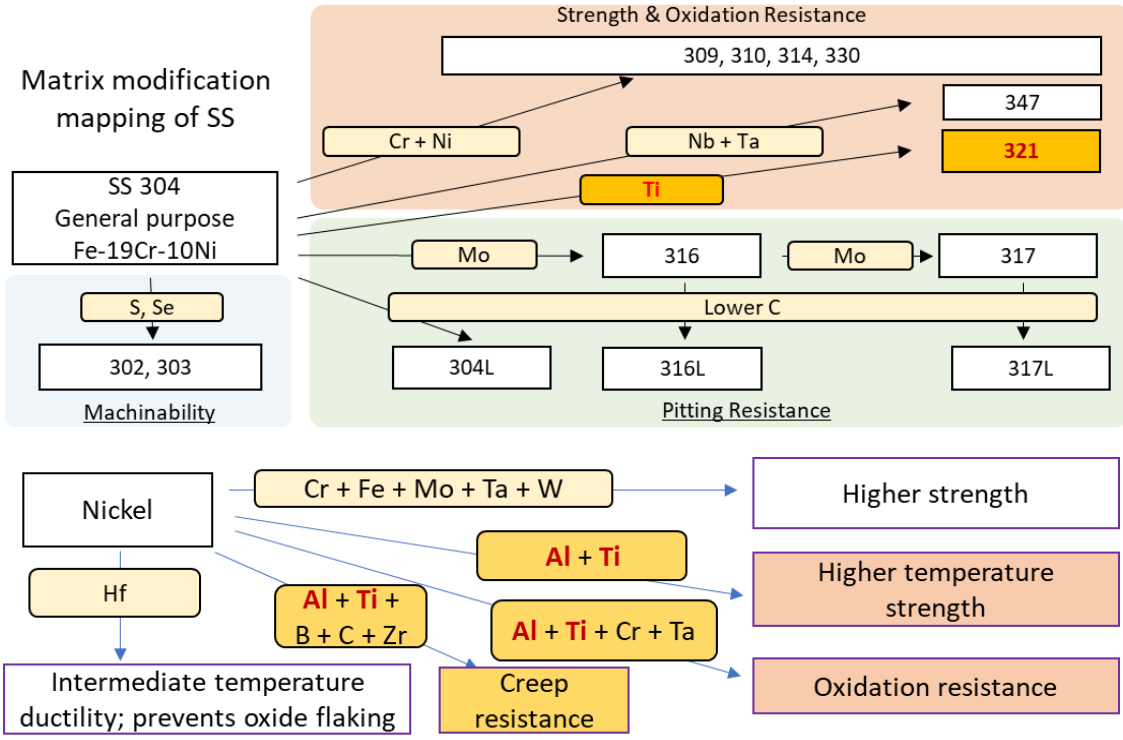

Figure 1.4 SS and Ni-based alloys enhancement through matrix modification.

Various types of steel, Inconel, refractory materials, graphite, and ceramics may dominate the structural material of the future advanced NPPs. Austenitic SS and Ferritic-Martensitic steels (F-M steels) are well-known materials that are widely utilized for current fossil and nuclear power plants. These materials are still becoming a proven candidate for next-generation NPPs. As illustrated in Figure 1.4, Several SS variants are developed from the basic grade of SS 304. High temperature resistance SS 310 is developed by increasing Cr and Ni content, good swelling resistance of SS 316 and D9 are produced by adding Ni, Mo, and Ti, and weld stabilized SS 316L is invented by reducing carbon content (Hoffelner, 2013, p. 98; Susan Jackson, 2016, p. 307). Similar to SS, Inconel 600 is also commonly used as a standard material for corrosion resistance and high temperature environment (Hoffelner, 2013, p. 107). Due to stress corrosion cracking (SSC) which was found during the utilization, furthermore, improvement is made by developing the newer type of Inconel (Feron and Staehle, 2016, p. 100), including X-750 with a higher concentration of solute Ti and Al.

Refractory elements including Ti and Al might be largely required for future material improvement. Ti and Al could increase high temperature strength, reduce the austenitic steel's tendency to suffer intergranular, and improve corrosion-resistant (Callister and Rethwisch, 2013, pp. 410–416; Hoffelner, 2013, pp. 97–100; Lahiri, 2017, p. 137). Ti and Al are easy to migrate to the surface and oxidize (Wei gao, 2008, pp. 279–283). The formed oxide film of Ti and Al on the surface could reduce oxygen diffusion to the matrix and then increase the oxidation resistance. Ti is also able to increase oxidation resistance by reacting with carbon (C) that may be soluble and/or diffuse to the matrix by forming TiC. This reaction indirectly maintains chromium oxide layer integrity by reducing the C precipitation on it (Yvon, 2017, p. 598). Ti and C interaction could form fine-scale carbides, carbonitrides, and intermetallic phases, then increase the high temperature strength. Ti and Al may also change the crystal structure by forming γ' and greatly increase the swelling resistance and creep properties of Ni-base alloys (Wei gao, 2008; Susan Jackson, 2016; Was and Ukai, 2019). On the other side, Ti can be used to increase the corrosion-resistant of RVP by dissolving TiO_2 into the coolant (Takashi Mawatari, Yasushi Yamamoto, Osamu Shibasaki, Takahito Hara, Yusuke Horayama, 2021).

1.1.4 Cs Chemisorption Consideration in Advanced Reactors

Although advanced reactors are designed much safer compared with current LWRs, consideration should be made, especially for worker safety. Appropriate operation & maintenance programs should be prepared to ensure that future commercial operations achieve the highest safety and reliability levels. Operation & maintenance activities contribute to the second largest cost for the entire NPP lifetime (Mari, 2014). Based on the power generation costs assessment, maintenance activities even become the biggest cost of overall NPP lifetime in Japan (Matsuo, Shimogori and Suzuki, 2015). Inappropriate operation & maintenance may affect reactor reliability. Peach Bottom HTGR in the USA had faced reliability issues, resulting in being less economical which caused it to be decommissioned faster than it should be (International Atomic Energy Agency (IAEA) - NS-R-1, 2012). Because of that, good maintenance program preparation is important to achieve the highest level of safety, reliability & availability, and profitability.

As mentioned by (Nakano *et al.*, 2014), during 32 operation cycles (1 cycle = 1.5 years) and 20 days after the shutdown of 300 MW direct cycle HTGR, around 7180 GBq ^{137}Cs could be plate-out from the core. In the case of water and/or air ingress accidents, Cs may interact with water which causes the release of CsOH (Rainer Moormann, Werner Schenk, 2001; Moormann, 2008; Kissane, 2009; Moormann and Hilpert, 2017; C. Li *et al.*, 2019).

Appropriate structural materials should be selected during the design and construction period by considering safety margin, economical aspects, source terms retention, and chemisorption probability. High source terms retention is expected on the fuel matrix to limit the release. Because of that, such kind of fuel, i.e., TRISO (TRi-structural ISOtropic) is designed for this purpose (Kugeler, K., Nabielek, H., Buckthorpe and Editors: Scheuermann, W., Haneklaus, N., Fütterer, 2017). Typical TRISO fuel consists of four layers with three kinds of materials and gives a small diffusion coefficient for several volatile FPs which makes their release last longer. These layers from inside to outside are; the low-density pyrolytic carbon (PyC) layer, high-density PyC, silicon carbide (SiC), and the last is high-density PyC (Demkowicz, Liu and Hunn, 2019). Low-density PyC has two main functions, as the retention barrier for gaseous materials by allowing the kernel to swell under irradiation and providing void volume, and protection of the next layer from the recoiling fission products. Inner high-density PyC forms an impenetrable barrier to gaseous fission products and slows down the metallic fission products transport to the SiC layer. SiC layer is the main fission product barrier both for gaseous and metallic fission products. And the last layer, the outer high-density PyC puts positive pressure on the SiC layer and helps to contain internal gas pressure. On the other hand, several components such as turbines, pumps, heat exchangers, etc., which should be maintained periodically should have low radioactivity to make them can be accessed by the worker safely. To fulfill this requirement, source terms retention, and chemisorption on these components should be designed to be as low as possible. That can be archived by selecting appropriate structural materials during design and construction.

Long operations with short shutdown periods must be achieved to get the maximum profit. To reach that condition, the maintenance division shall prepare an accurate maintenance program. They must be able to determine maintenance strategies, including whether a component should undergo preventive or corrective maintenance,

and how maintenance should be carried out, whether time-based, conditional, planned, or unplanned-based maintenance (International Atomic Energy Agency (IAEA), 2018). Besides that, they also must predict the radiation level of each component and determine whether maintenance activities can be conducted directly or remotely; and for how long they can be there. Low radiation exposure due to the low source terms retention on the frequently accessed components reduces the risk of worker radiation exposure and may decrease operating and maintenance costs. This is also likely to provide benefits at the time of decommissioning. Because of that, unless in the fuel, it is important to ensure source terms chemisorption, particularly Cs in the nuclear structural materials is kept as small as possible.

1.2 Study Objectives

Typical Cs chemisorption experimental studies are conducted on a supersaturated environment following a high temperature gas-solid reaction. However, supersaturated Cs particles may change into an aerosol (Sehgal, 2012, p. 460) and then condense as the liquid droplet (Mishra *et al.*, 2019). The liquid droplet interaction with the structural materials is important, especially to simulate leakage parts to the environment (Watanabe, Yamada, and Ohsaki, 2009) (Firnhaber *et al.*, 1996). Solid-liquid interaction especially at lower temperatures is classified as high significance but with low knowledge availability (Lind *et al.*, 2020).

The pre-existing oxide film may play an important role during the interaction, but it is not intensively explored in previous studies (Elrick *et al.*, 1984), (Sallach *et al.*, 1986) since it is impossible to know the exact nature of the oxide when the structural material is exposed to Cs due to the rapid temperature and atmosphere changing during a severe accident. Cs exposure with almost no oxidation and with sufficient oxide formation at certain temperatures is the simplest comparison that might be done. Oxide formation of all alloys is relatively similar at the operating temperature of LWR. However, the differences might be more obvious at higher temperatures, especially due to the matrix composition differences.

Because of that, the main objective of this study is to investigate the correlation between Cs chemisorption and oxidation due to matrix composition differences by following liquid Cs and solid materials interaction.

1.3 Thesis Outline

This dissertation consists of 6 chapters that describe every step of the study.

Chapter 1 is the introduction section, which explains the study background, motivation, and study objectives.

Chapter 2 presents the experimental methodology development. This includes the literature survey related to the previous methods & models that have been established for the gas-solid interaction-related chemisorption studies, apparatus setup, temperature & environmental setting, and the preliminary tests.

Chapter 3 describes the identification of the effect of solute elements and temperature on the oxide film growth. This chapter includes the pre-oxide film formation identification of four materials that are used in this study, SS 304, SS 321, Inconel 600, and X-750.

Chapter 4 explains the experimental result related to the precursor & specimens' interaction. This chapter presents the differences in Cs amount on unoxidized and oxidized specimens, the formation of Cs compounds identification on each type of specimen at each temperature treatment, including analytical tests related to the formation and decomposition of newly formed Cs compounds.

Chapter 5 discusses the Cs chemisorption identification and its relationship with minor solute elements, including compound prediction which is analyzed through synthesis.

Chapter 6 presents the summary and conclusion of the study, then followed by a recommendation for the avenues for future works.

1.4 References

Aggarwal, S. K. (1995) Effect of Aging on the PWR Chemical and Volume Control System. Washington.

BP (2017) 'BP Energy Outlook Energy 2017', BP Statistical Review of World Energy, p. 52. doi: 10.1017/CBO9781107415324.004.

Brillant, G., Marchetto, C. and Plumecocq, W. (2013) 'Fission product release from nuclear fuel II. Validation of ASTEC/ELSA on analytical and large scale experiments', Annals of Nuclear Energy. Elsevier Ltd, 61, pp. 96–101. doi: 10.1016/j.anucene.2013.03.045.

Brinkmann, G. et al. (2006) 'Important viewpoints proposed for a safety approach of HTGR reactors in Europe: Final results of the EC-funded HTR-L project', Nuclear Engineering and Design, 236(5–6), pp. 463–474. doi: 10.1016/j.nucengdes.2005.11.017.

Bryan, R. H. and Dudley, I. T. (1974) Estimated Quantities of Materials Contained in a 1000-MW(e) PWR Power Plant, ORNL Technical Report. Tennessee.

Busby, J. T. (2019) 'Overview of Structural Materials in Water-Cooled Fission Reactors', in Structural Alloys for Nuclear Energy Applications. Elsevier, pp. 1–22. doi: 10.1016/B978-0-12-397046-6.00001-0.

Callister, W. D. and Rethwisch, D. G. (2013) Materials Science and Engineering 9th Edition. 9th Edition, Wiley. 9th Edition. Wiley. doi: 10.1016/j.str.2011.03.005.

Chen, D. et al. (2008) 'Corrosion of aluminium in the aqueous chemical environment of a loss-of-coolant accident at a nuclear power plant', Corrosion Science, 50(4), pp. 1046–1057. doi: 10.1016/j.corsci.2007.11.034.

Chersola, D., Lomonaco, G. and Marotta, R. (2015) 'The VHTR and GFR and their use in innovative symbiotic fuel cycles', Progress in Nuclear Energy. Elsevier Ltd, 83, pp. 443–459. doi: 10.1016/j.pnucene.2014.12.005.

Cinotti, L. et al. (2011) 'Lead-cooled system design and challenges in the frame of Generation IV International Forum', Journal of Nuclear Materials. Elsevier B.V., 415(3), pp. 245–253. doi: 10.1016/j.jnucmat.2011.04.042.

Degueldre, C. A. (2017) The analysis of nuclear materials and their environments, The Analysis of Nuclear Materials and Their Environments. doi: 10.1007/978-3-319-58006-7.

Demkowicz, P. A., Liu, B. and Hunn, J. D. (2019) 'Coated particle fuel: Historical perspectives and current progress', Journal of Nuclear Materials, 515, pp. 434–450. doi: 10.1016/j.jnucmat.2018.09.044.

Elrick, R. et al. (1984) Reaction between some Cesium-Iodine compounds and the reactors materials 304 stainless steel, Inconel 600 and Silver/ Volume I Cesium Hydroxide Reactions. Albuquerque, NM (USA).

Feron, D. and Staehle, R. W. (2016) Stress Corrosion Cracking of Nickel Based Alloys in Water-Cooled Nuclear Reactors: The Coriou Effect, Stress Corrosion Cracking of Nickel Based Alloys in Water-Cooled Nuclear Reactors: The Coriou Effect. doi: 10.1016/C2014-0-01194-X.

Firnhaber, M. et al. (1996) 'International Standard Problem ISP37: VANAM M3. A Multicompartment Aerosol Depletion Test with Hygroscopic Aerosol Material'. Moulineaux: Committee on the Safety of Nuclear Installations OECD Nuclear Energy Agency.

Hashemian, H. M. (2011) 'On-line monitoring applications in nuclear power plants', Progress in Nuclear Energy. Elsevier Ltd, 53(2), pp. 167–181. doi: 10.1016/j.pnucene.2010.08.003.

Haste, T., Payot, F. and Bottomley, P. D. W. (2013) 'Transport and deposition in the Phébus FP circuit', Annals of Nuclear Energy. Elsevier Ltd, 61, pp. 102–121. doi: 10.1016/j.anucene.2012.10.032.

Hoffelner, W. (2013) Materials for Nuclear Plants, Materials for Nuclear Plants. London: Springer London. doi: 10.1007/978-1-4471-2915-8.

IAEA (2021) 'Nuclear Power Reactors in the World'. Viena: IAEA.

Idaho National Laboratory (INL) (2010) HTGR Mechanistic Source Terms White Paper. Idaho. doi: 10.2172/989901.

International Atomic Energy Agency (IAEA) (2018) Maintenance Optimization Programme for Nuclear Power Plants. Vienna. Available at: http://www.iaea.org/Publications/index.html.

International Atomic Energy Agency (IAEA) - NS-R-1 (2012) Advances in High Temperature Gas Cooled Reactor Fuel Technology. Vienna.

JAEA (2019) Fission Product Chemistry Database ECUME Version 1 . 1, JAEA-Data/Code 2019-017. Tokai-mura. doi: 10.11484/jaea-data-code-2019-017.

Jeong, H. and Chang, S. H. (2008) 'Development of a method of evaluating an inventory of fission products for a pebble bed reactor', Annals of Nuclear Energy, 35(12), pp. 2161–2171. doi: 10.1016/j.anucene.2008.10.001.

Kaminski, M. D. et al. (2019) 'A case study of cesium sorption onto concrete materials and evaluation of wash agents: Implications for wide area recovery', Journal of Environmental Chemical Engineering. Elsevier, 7(3), p. 103140. doi: 10.1016/j.jece.2019.103140.

Kissane, M. P. (2009) 'A review of radionuclide behaviour in the primary system of a very-high-temperature reactor', Nuclear Engineering and Design, 239(12), pp. 3076–3091. doi: 10.1016/j.nucengdes.2009.09.012.

Klein-Heßling, W. et al. (2014) 'Conclusions on severe accident research priorities', Annals of Nuclear Energy, 74(C), pp. 4–11. doi: 10.1016/j.anucene.2014.07.015.

Knebel, K., Jokiniemi, J. and Bottomley, P. D. (2019) 'A review of revaporisation behaviour of radioactive Cs deposits and its impact on the source term in severe nuclear accidents from Phébus FP results and single effect testing', Journal of Nuclear Science and Technology. Taylor & Francis, 56(9–10), pp. 772–789. doi: 10.1080/00223131.2018.1558130.

Kobata, M. et al. (2018) 'Chemical form analysis of reaction products in Cs-adsorption on stainless steel by means of HAXPES and SEM/EDX', Journal of Nuclear Materials. Elsevier B.V, 498, pp. 387–394. doi: 10.1016/j.jnucmat.2017.10.035.

Koizumi, Y., Okawa, T. and Mori, S. (eds) (2021) Fundamentals of Thermal and Nuclear Power Generation, Fundamentals of Thermal and Nuclear Power Generation. Oxford: Elsevier. doi: 10.1016/C2018-0-04630-7.

Kugeler, K., Nabielek, H., Buckthorpe, D. and Editors: Scheuermann, W., Haneklaus, N., Fütterer, M. (2017) The High Temperature Gas-cooled Reactor: Safety considerations of the (V)HTR-Modul. doi: 10.2760/270321.

Lahiri, A. K. (2017) Applied Metallurgy and Corrosion Control, Applied Metallurgy and Corrosion Control. doi: 10.1007/978-981-10-4684-1.

Di Lemma, F.G. et al. (2017) 'Experimental investigation of the influence of Mo contained in stainless steel on Cs chemisorption behavior', Journal of Nuclear Materials, 484, pp. 174–182. doi: 10.1016/j.jnucmat.2016.11.031.

Di Lemma, Fidelma Giulia, et al. (2017) 'Prediction of chemical effects of Mo and B on the Cs chemisorption onto stainless steel', Energy Procedia. Elsevier B.V., 127, pp. 29–34. doi: 10.1016/j.egypro.2017.08.092.

Lewandowski, C. M., Co-investigator, N. and Lewandowski, C. M. (2015) Probabilistic Safety Assessment in the Chemical and Nuclear Industries, The effects of brief mindfulness intervention on acute pain experience: An examination of individual difference. doi: 10.1017/CBO9781107415324.004.

Li, C. et al. (2019) 'Chemical Forms of Important Fission Products in Primary Circuit of HTR-PM under Conditions of Normal Operation and Overpressure and Water Ingress Accidents: A Study with a Chemical Thermodynamics Approach', Science and Technology of Nuclear Installations, 2019, pp. 1–12. doi: 10.1155/2019/4251280.

Lind, T. et al. (2020) 'A summary of fission-product-transport phenomena during SGTR severe accidents', Nuclear Engineering and Design, 363(April), p. 110635. doi: 10.1016/j.nucengdes.2020.110635.

Lumley, R. N. (ed.) (2018) Fundamentals of Aluminium Metallurgy. Melbourne: Elsevier. doi: 10.1016/C2016-0-02117-4.

Mari, C. (2014) ‘The costs of generating electricity and the competitiveness of nuclear power’, Progress in Nuclear Energy, 73, pp. 153–161. doi: 10.1016/j.pnucene.2014.02.005.

Matsuo, Y., Nagatomi, Y. and Murakami, T. (2011) ‘Thermal and Nuclear Power Generation Cost Estimates Using Corporate Financial Statements in Japan’, pp. 1–20.

Matsuo, Y., Shimogori, K. and Suzuki, A. (2015) ‘Major Issues Regarding Nuclear Power Generation Costs Assessment in Japan’, IEEJ Energy Journal, 10, No.2, pp. 47–90.

Mishra, G. et al. (2019) ‘Hygroscopic growth of CsI and CsOH particles in context of nuclear reactor accident research’, Journal of Aerosol Science. Elsevier Ltd, 132(January), pp. 60–69. doi: 10.1016/j.jaerosci.2019.03.008.

Miwa, S. et al. (2020) ‘Boron chemistry during transportation in the high temperature region of a boiling water reactor under severe accident conditions’, Journal of Nuclear Science and Technology. Taylor & Francis, 57(3), pp. 291–300. doi: 10.1080/00223131.2019.1671913.

Miyahara, N. et al. (2019) ‘Chemical reaction kinetics dataset of Cs-I-B-Mo-O-H system for evaluation of fission product chemistry under LWR severe accident conditions’, Journal of Nuclear Science and Technology. Taylor & Francis, 56(2), pp. 228–240. doi: 10.1080/00223131.2018.1544939.

Mohsin, M. H., Qureshi, K., and Ashfaq, T. (2019) ‘Safety assessment of MSR concept using INPRO methodology’, Progress in Nuclear Energy. Elsevier, 117(December 2017), p. 103099. doi: 10.1016/j.pnucene.2019.103099.

Moormann, R. (2008) ‘Fission Product Transport and Source Terms in HTRs: Experience from AVR Pebble Bed Reactor’, Science and Technology of Nuclear Installations, 2008, pp. 1–14. doi: 10.1155/2008/597491.

Moormann, R. and Hilpert, K. (2017) ‘Chemical Behavior of Fission Products in Core Heatup Accidents in High-Temperature Gas-Cooled Reactors’, Nuclear Technology, 94(1), pp. 56–67. doi: 10.13182/nt91-a16221.

Murty, K. L. and Charit, I. (2008) 'Structural materials for Gen-IV nuclear reactors: Challenges and opportunities', Journal of Nuclear Materials. Elsevier B.V., 383(1–2), pp. 189–195. doi: 10.1016/j.jnucmat.2008.08.044.

Nakajima, K. et al. (2018) 'An experimental investigation for atmospheric effects on Cs chemisorption onto stainless steel', Progress in Nuclear Science and Technology, 5(0), pp. 168–170. doi: 10.15669/pnst.5.168.

Nakano, M. et al. (2014) 'Core design and safety analyses of 600 MWt, 950 °c high temperature gas-cooled reactor', Nuclear Engineering and Design. Elsevier B.V., 271, pp. 560–563. doi: 10.1016/j.nucengdes.2013.12.032.

Nishioka, S. et al. (2019) 'An experimental investigation of influencing chemical factors onCs-chemisorption behavior onto stainless steel', Journal of Nuclear Science and Technology. Taylor & Francis, 00(00), pp. 1–8. doi: 10.1080/00223131.2019.1633968.

Osaka, M. et al. (2016) Results and Progress of Fundamental Research on Fission Product Chemistry - Progress Report in 2015. Tokai-mura. doi: 10.11484/jaea-review-2016-026.

Piippo T. Laitinen, P. (1997) Corrosion behavior of zinc and aluminum in simulated nuclear accident environments, Radiation and Nuclear Safety.

Pradeep, A. et al. (2016) 'Estimation of evaporation rate of cesium from hot sodium pool to inert cover gas of typical SFR', Annals of Nuclear Energy. Elsevier Ltd, 92, pp. 431–439. doi: 10.1016/j.anucene.2016.01.051.

Raimond, E. et al. (2013) 'Use of Phébus FP and other FP programs for atmospheric radioactive release assessment in case of a severe accident in a PWR (deterministic and probabilistic approaches developed at IRSN)', Annals of Nuclear Energy. Elsevier Ltd, 61, pp. 190–198. doi: 10.1016/j.anucene.2013.05.035.

Rainer Moormann, Werner Schenk, K. V. (2001) 'Source term estimation for small-sized HTRs: Status and further needs, extracted from German safety analyses', Nuclear Technology, 135(3), pp. 183–193. doi: 10.13182/NT01-A3215.

Roki, F.-Z. et al. (2015) ‘Improvements in the assessment of the thermodynamic properties of condensed and gaseous phases of the CsOH compound’, The Journal of Chemical Thermodynamics. Academic Press, 80, pp. 147–160. doi: 10.1016/j.jct.2014.08.021.

Roki, F. Z. et al. (2008) ‘Thermodynamic study of the CsOH(s,l) vaporization by high temperature mass spectrometry’, The Journal of Chemical Thermodynamics, 40(3), pp. 401–416. doi: 10.1016/j.jct.2007.09.013.

Sallach, R. A. et al. (1986) Reaction between some cesium-iodine compounds and the reactor materials 304 stainless steel Inconel 600 and silver. Volume II. Cesium iodide reactions. Albuquerque, NM (USA). Available at: https://play.google.com/store/books/details?id=tYxWAAAAMAAJ.

Sallach, R. A. and Elrick, R. M. (1985) ‘Chemical reactions of CsOH, CsI and Te vapors with oxidizing reactor materials’. Available at: https://inis.iaea.org/search/search.aspx?orig_q=RN:19023555 (Accessed: 7 April 2021).

Sehgal, B. R. (2012) Nuclear Safety in Light Water Reactors, Nuclear Safety in Light Water Reactors. Elsevier. doi: 10.1016/C2010-0-67817-5.

Susan Jackson, A. S. (2016) Structural Alloys for Power Plants: Operational Challenges and High-temperature Materials, Journal of Chemical Information and Modeling. doi: 10.1017/CBO9781107415324.004.

Takashi Mawatari, Yasushi Yamamoto, Osamu Shibasaki, Takahito Hara, Yusuke Horayama, J. T. (2021) ‘Evaluation of TiO2 Deposition on Structure Surfaces and Water Radiolysis for the Corrosive Environment in a Reactor Pressure Vessel’, in ICONE28. ASME.

Vogel, R. C. (1985) ‘Source term research and prognosis’, Nuclear Engineering and Design, 89(2–3), pp. 513–525. doi: 10.1016/0029-5493(85)90087-1.

Was, G. S. and Ukai, S. (2019) Austenitic stainless steels, Structural Alloys for Nuclear Energy Applications. Elsevier Inc. doi: 10.1016/B978-0-12-397046-6.00008-3.

Watanabe, A., Yamada, K. and Ohsaki, M. (2009) 'FP Aerosol Trapping Effect Along the Leakage Paths of Degraded Containment Penetrations During a Severe Accident (II) Decontamination Factor at the Containment Penetrations and Its Application to Actual Plant', Transactions of the Atomic Energy Society of Japan, 8(4), pp. 332–343. doi: 10.3327/taesj.J08.052.

Wei gao, Z. L. (2008) Developments in high-temperature corrosion and protection of materials. Edited by W. Gao and Zhengwei Li. Corwall: Woodhead Publishing Limited. Available at: https://www.sciencedirect.com/book/9781845692193/developments-in-high-temperature-corrosion-and-protection-of-materials.

Yvon, P. (2017) Structural Materials for Generation IV Nuclear Reactors, Structural Materials for Generation IV Nuclear Reactors. Elsevier. doi: 10.1016/C2014-0-03589-7.

Zohuri, B. and McDaniel, P. (2019) Advanced Smaller Modular Reactors, Advanced Smaller Modular Reactors. doi: 10.1007/978-3-030-23682-3.

(This page intentionally left blank)

Chapter 2

Methodology Development

(This page intentionally left blank)

Fundamental research is what I do when I have no idea about what I am doing.

~Wernher Von Braun

(This page intentionally left blank)

Chapter 2

Methodology Development

2.1 Introduction

Most Cs chemisorption experimental studies were conducted to solve severe accident-related phenomena, especially at elevated temperatures; such as (Auvinen *et al.*, 2000; Do *et al.*, 2017; Kobata *et al.*, 2018; Miwa *et al.*, 2018; Nakajima *et al.*, 2018; Rizaal *et al.*, 2021). These studies are generally performed by reproducing the accident conditions based on the real recorded data, or from the accident code models analysis. Several types of apparatus starting from the simple to the complicated systems, which can be used to carry out mechanistic and/or integral source terms transport studies have been developed.

Although various types of apparatus exist, they are typically constructed by following Figure 2.1. Typical apparatus for source terms studies consists of gas inlet, heater, and gas outlet i.e., implemented by CREST and TeRRa facilities (Miradji F.; et al., 2019; Miwa *et al.*, 2020). Various types of the gasses such as oxygen, hydrogen, nitrogen, argon, air, steam, etc. are installed on the gas inlet. The composition and flow rate of these gasses could be adjusted based on the experimental objectives. The heater itself is usually designed to produce a temperature gradient from hotter to cooler regions. Source terms precursor then be evaporated in the hotter regions while the target specimens are put just after the precursor at the colder regions. By following that arrangement and utilizing gas flow, the gaseous precursor could interact with the specimens. Furthermore, gas trapping fluid and/or mass spectroscopy may be installed on the gas outlet if they are important to fulfill the study objectives.

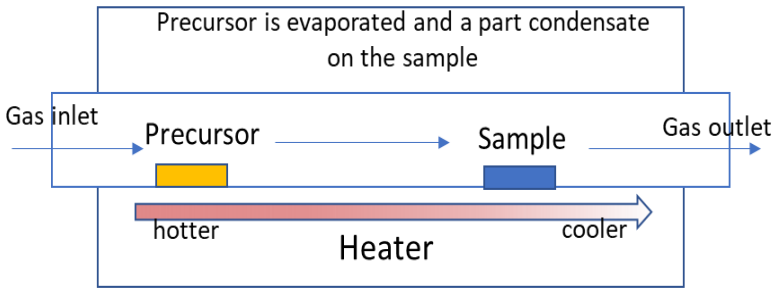

Figure 2.1 Typical heater utilized for source terms transport studies.

Interaction between precursor and specimens in the gaseous phase as illustrated in Figure 2.1, could be calculated by assuming absorption rate (N) as the first-order reaction by multiplying the mass transfer coefficient in the gaseous phase (k_G) with the difference between bulk gaseous source terms concentration (C_g) and source terms concentration at the interface between the gas and solid phase (C_w). Furthermore, the source terms may condensate and deposit, which is considered as the solid phase that can be modeled based on the penetration theory accompanied by chemical reactions. The absorption rate in the solid phase can be calculated as the multiplication between Hatta number (β), mass transfer coefficient of reactant in the solid phase (k_S), and reactant concentration in the solid phase (C_i). Those mechanisms and models were described by (Nakajima *et al.*, 2019) as can be illustrated in Figure 2.2.

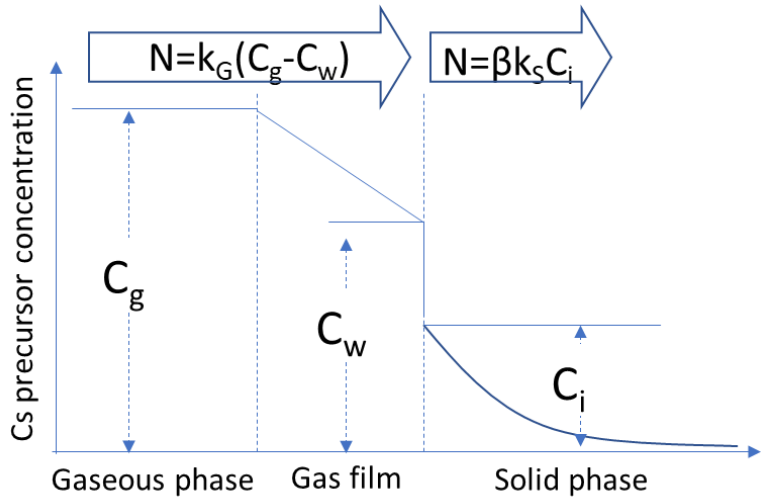

Figure 2.2. Typical absorption rate model for Cs chemisorption quantification.

CsOH must be in the liquid phase if the deposition region's temperature is ≥ 272 °C (Gurvich *et al.*, 1997; Kissane, 2009; Gouëllo *et al.*, 2018), and remain in the liquid for at least up to ~1000 °C. At ≥ 1000 °C, the CsOH evaporation goes very fast, making all of it become a gaseous phase.

Even though typical apparatus and existing chemisorption models consideration could be utilized for liquid-solid interaction, however, some limitations exist. The typical experiments are usually conducted by using a limited amount of precursor, and with a short period of treatment. As a result, source terms that could be deposited on the target

specimens become very limited. Characterization of limited Cs deposition is difficult even by using special techniques.

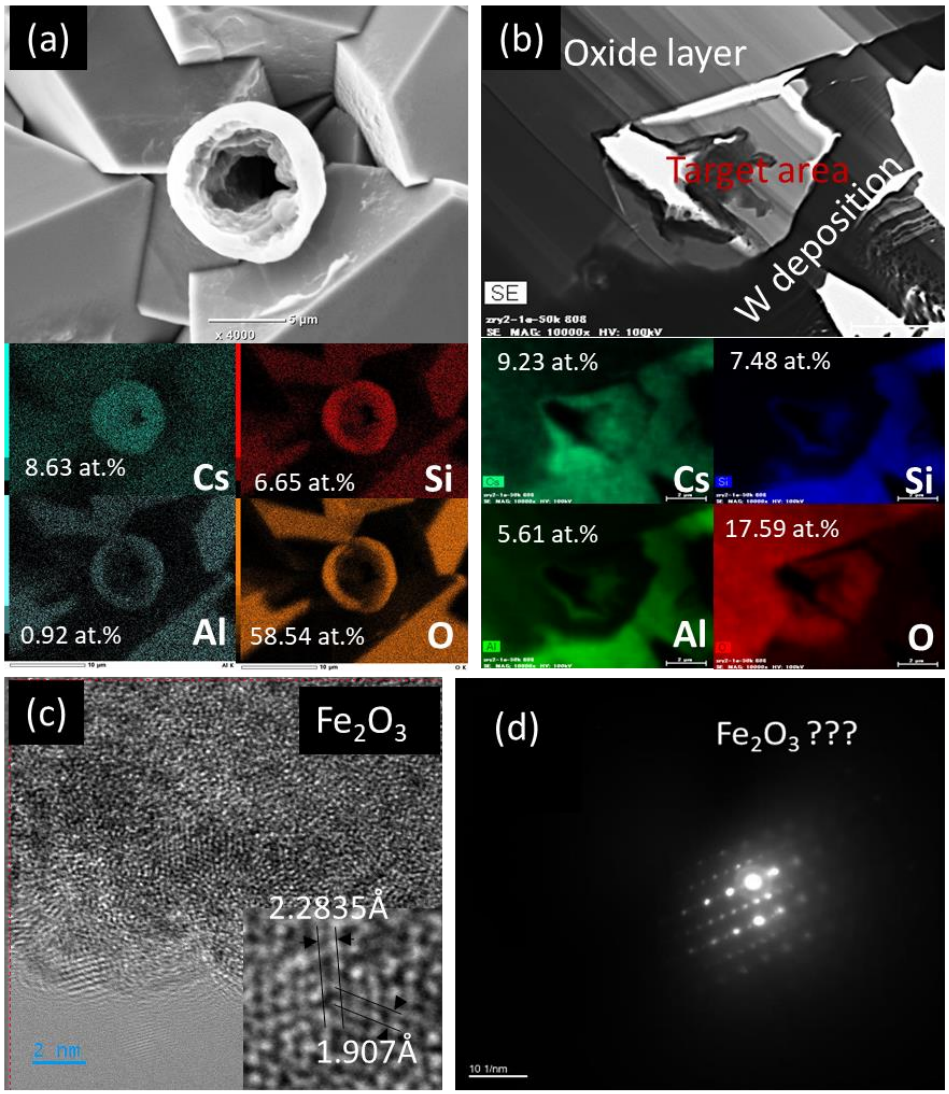

Figure 2.3. Characterization of chemisorbed Cs compounds on the surface of SS 304 which is produced by following gas-solid reaction using (a) SEM/EDS, (b) TEM/EDS, (c) high-resolution TEM, and (d) electron diffraction.

Figure 2.3 shows SEM and Transmission Electron Microscope (TEM) characterization of Cs chemisorption onto SS 304 which was produced by gas-solid interaction in Japan Atomic Energy Agency (JAEA) facilities. By utilizing SEM/EDS as shown in Figure 2.3 (a), overlapping between Cs, Si and O are visible, indicating the existence of the formation of Cs-Si-O compounds. To examine the exact crystal structures of these Cs compounds, TEM specimens were prepared by using a Focused Ion Beam

(FIB) machine, which can be observed as shown in Figure 2.3 (b). Even though the existence of Cs-Si-O compounds can be observed by TEM/EDS characterization, both high-resolution TEM and electron diffraction are unable to identify Cs-related structures as shown in Figures 2.3 (c) and (d). Most of the structures are identified as Fe_2O_3, which is a common structure of the SS outer oxide layer. This happens because the formation of Cs compounds is not isolated and clustered as a single crystal but composed of several different chemical compounds as a multi-crystal formation which is dominated by Fe_2O_3. Observation of the Fe_2O_3 compound from this specimen indicates that oxidation could not be ruled out even from gas-solid interactions which were conducted in relatively short periods.

2.2 Experimental Design

After considering the above difficulties, the preliminary evidence related to oxidation, and considering the objectives of this study, then the simplified approach is designed by involving some parameters that may have a direct or indirect correlation with Cs chemisorption. Base and solute elements, especially Fe, Ni, Cr, Al, Ti, and Si directly contribute to the oxidation behavior of an alloy. Alloy's elements may interact with Cs and affect the Cs' transport behavior. Beyond these two things, temperature and environmental conditions may also contribute significantly. To observe these parameters, this study was designed by following some steps, choosing appropriate precursor and materials, observing the effect of base and solute elements on the oxide film growth, identifying the correlation of different oxide films on the CsOH precursor interaction, and recognizing Cs chemisorption on each specimen. Although the most interesting part of liquid-solid chemisorption studies is in low temperature, in this study the wide temperature ranges are considered. It is performed to capture a wider scope of the phenomenon that may occur.

2.2.1 Precursor and Material Selection

Liquid CsOH with solid materials interaction could happen in several ways depending on the type of reactor and environment conditions (normal operation and various accident scenarios). In the case of LWR, CsOH may be condensed and/or dissolved in water when

interacting with materials (Firnhaber *et al.*, 1996; Sehgal, 2012, pp. 456–457; van Dorsselaere *et al.*, 2017). In non-water-cooled reactors, CsOH could be formed especially in case of water ingress, as postulated to be a typical accident in High Temperature Gas Reactor (HTGR) (Merwe, 2009; Humrickhouse, 2011; Liu *et al.*, 2016; Kugeler, K., Nabielek, H., Buckthorpe and Editors: Scheuermann, W., Haneklaus, N., Fütterer, 2017; Ding *et al.*, 2018). Liquid CsOH interaction furthermore occurs in several SSCs, especially those located in the cooler regions. However, considering that the objective of this study is limited to the relationship between solute elements, oxide film, and CsOH chemisorption speciation in some intended temperatures, then the detailed effects of water-related, and air ingress are ruled out.

2.2.1.1 Received CsOH Precursor

Cesium hydroxide hydrate ($CsOH{\cdot}H_2O$) is chosen as the precursor by considering CsOH as one of the most important compounds which may be formed and migrate both during normal operation and accident conditions (Martín-Fuertes *et al.*, 2007; Roki *et al.*, 2015; C. Li *et al.*, 2019; Nishioka *et al.*, 2019). $CsOH{\cdot}H_2O$ precursor is provided by Combi-Blocks Inc. with ~95% purity.

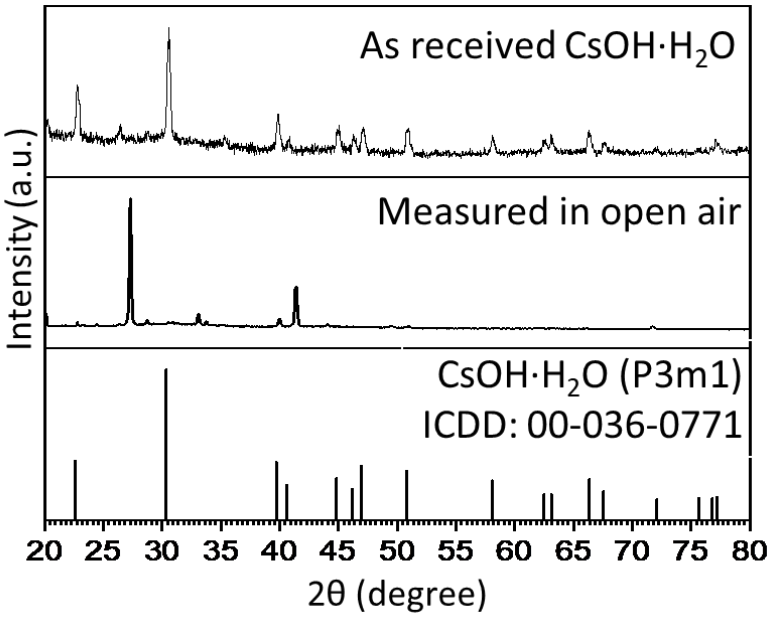

Figure 2.4. XRD peaks changing of received CsOH precursor when measured in an open-air environment.

$CsOH{\cdot}H_2O$ is sensitive to humidity, making its characterization should be done in a vacuum or inert gas environment. As shown in Figure 2.4, the received $CsOH{\cdot}H_2O$ precursor is identified to match with the International Centre for Diffraction Data (ICDD) card number 00-036-0771, with the rest peaks related to the surface water. However, when the precursor is put in the open-air environment, its peaks are changed gradually with relatively stable peaks that could be archived after 30 minutes. Those changes indicate crystal structure transformation caused by moisture absorption.

2.2.1.2 Selected Structural Materials

Four types of alloys that are commonly used for nuclear structural materials are chosen. These alloys consist of Fe-based and Ni-based alloys. Both respective Fe-based and Ni-based alloys are composed of almost similar elements except for the existence of some minor solute elements, especially Al and Ti. These elements improve the oxidation properties of both SS and Ni-based alloys.

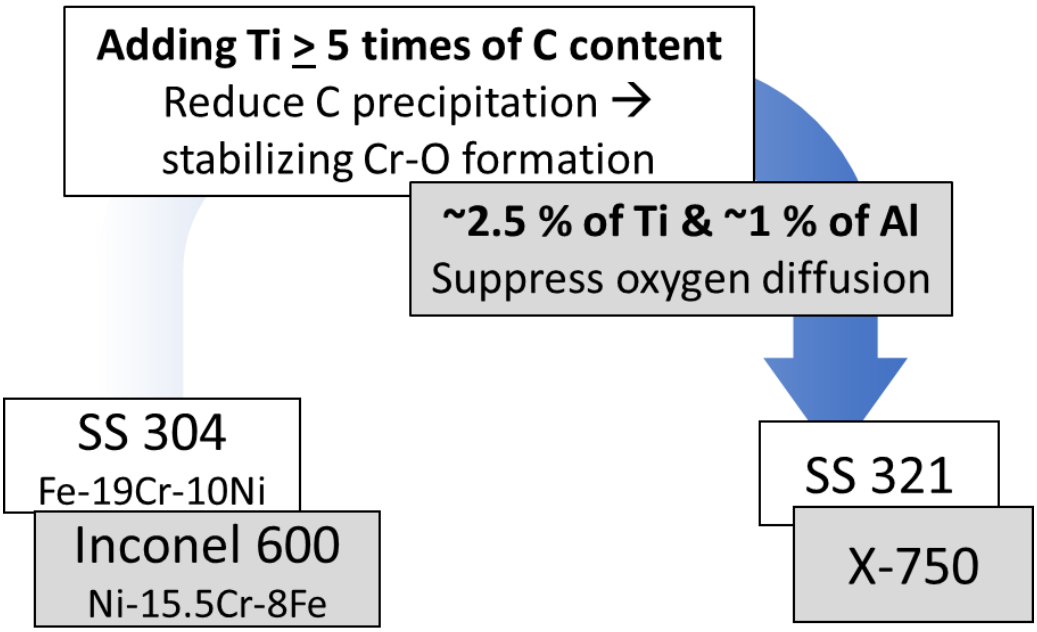

Figure 2.5. Effects of Al and Ti on the oxidation properties of SS 304 & SS 321, and Inconel 600 & X-750.

As illustrated in Figure 2.5, SS 304 and SS 321 are chosen because of some reasons. SS 304 is a proven alloy that is widely used in various types of reactors (Murty and Charit, 2008; Yvon, 2017). A huge amount of SS 304 can be found as the structural

material alongside LWR's cooling boundaries. SS 321 is also used on a limited part of current NPPs. However, SS 321 may be important for advanced reactors that require a higher operating temperature environment and better oxidation resistance properties (Williams, 2011, p. 226; Susan Jackson, 2016, pp. 113, 119–124). SS 304 and SS 321 consist of similar elemental composition, except for the existence of Ti for around ~5 times its carbon content to stabilize the formation of the chromium oxide layer (Lahiri, 2017, pp. 24–25).

Inconel 600 and X-750 are chosen as the representation of Ni-base alloys. Inconel 600 can be found on many parts of current LWR components, starting from the Control Rod Driving Mechanism (CRDM), steam generator, and turbine (Griffiths, 2019, p. 356). Except for the Ni and Fe elements as their basis and the availability of a small amount of Al and Ti, the concentration of the other solute elements between Inconel 600 and selected SS are almost similar. That similarity opens the possibility for a comparative study between them. X-750 on the other hand also can be found in current nuclear reactors, especially in the bolt, pump, and some parts of core structural materials (Hoffelner, 2013, p. 107; Was, 2017, p. 963). X-750 can be said to be an improvement of Inconel 600 due to its better oxidation resistance, high temperature strength, swelling resistance and creep properties. These property improvements are archived by increasing the concentration of solute Al and Ti to be ~1 wt.% and ~2.5 wt.% respectively (Ezugwu, 2004).

2.2.2 Specimens Preparation

2.2.2.1 Specimen of Nuclear Structural Materials

Selected SS 304, SS 321, Inconel 600, and X-750 materials are provided by Nilaco Corporation with the detailed composition shown in Table 2.1. The specimens are cut with the size of about 10 mm x 10 mm x 0.5 mm using a low-speed cutting machine. These specimens are then polished and grounded by following several steps starting by using 40-, 30-, 15-, 10- and 5-μm silicon carbide paper, then using 3-μm diamond and 0.05-μm alumina polishing suspension. Furthermore, all these specimens are cleaned using distilled water and ethanol after being polished by employing an ultrasonic cleaner for 180 seconds, respectively. Moreover, all specimens are dipped in acetone for around 2 seconds to remove any potential impurities.

Table 2.1 Element concentration on selected materials by manufacturer.

	Weight (%)			
	SS 304	**SS 321**	**Inconel 600**	**X-750**
Fe	balance	balance	6 - 10	5 - 9
Cr	17 - 19	17 - 19	14 - 17	14 - 17
Ni	8 -11	9 - 12	≤ 72	≤ 70
Mn	≤ 2	≤ 2	≤ 1	≤ 1
Ti	-	5	≤ 0.3	2.25 – 2.75
Si	≤ 1	≤ 1	≤ 0.5	≤ 1
Al	-	-	≤ 0.3	0.4 - 1

2.2.2.2 Specimens to Synthesis Cs Compounds

The additional analytical experimental procedure is conducted to identify the formation and decomposition of Cs-Fe-Cr-O compounds and to predict the chemisorbed tiny Cs-Al-Ti-Si-O particles. By assuming these compounds are formed due to the reaction between CsOH precursor with the oxides of respective elements, then Fe_3O_4, Cr_2O_3, Al_2O_3, SiO_2, and TiO_2 alongside $CsOH{\cdot}H_2O$ are used as the precursors. These oxide precursors are provided by Nilaco Corporation with ~99.9% purities.

2.2.3 Oxidation of Prepared Specimens

As explained by (Noguchi and Yakuwa, 2016), the oxide thickness (x) growth is typically considered following parabolic rate constant (k_p), which correlated with time (t) by following equation:

$$x = k_p \cdot \sqrt{t}$$

Oxide growth is self-controlled by the thickness of oxide film since it is directly related to oxygen diffusion to the matrix. Oxygen diffusion can be modeled following Fick's first law:

$$J = -D\frac{dc}{dx};$$

Where:

J is diffusion flux,

D is diffusivity, and

$\frac{dc}{dx}$ is the concentration gradient.

Furthermore k_p, is declared by combining Fick's first law with Wagner's theory. Then elements migration of the alloy to the outer part, and oxygen diffusion from the environment to the matrix can be expressed following:

$$k_p = \frac{1}{RT}\int_{\mu_M''}^{\mu_M'} D_M \, d\mu_M, \text{ and } k_p = \frac{1}{RT}\int_{\mu_0''}^{\mu_0'} D_O \, d\mu_O;$$

Where:

R is the ideal gas constant,

T is absolute temperature,

μ_M and μ_O represent the chemical potential of metal (M) and oxygen on the interface between metal and oxide scale (suffix [`]) and between oxide scale and atmosphere (suffix ["]).

By considering metal migration is much slower compared with oxygen diffusion, and the stoichiometric composition of the formed metal oxide ($M_\alpha O_\beta$) is small.

$$\alpha \cdot \mu_M + \beta \cdot \mu_O = \mu_{M_\alpha O_\beta} \approx const.;$$

Then the chemical potential of oxygen is expressed as:

$$\mu_O = \frac{1}{2}\left(\mu_{O_2}^{\cdot} + RTlnP_{O_2}\right)$$

Furthermore, the parabolic rate constant can be re-written as:

$$k_p = \frac{\beta}{2\alpha}\int_{P_{O_2}''}^{P_{O_2}'} D_M dlnP_{O_2} \text{ or } k_p = \frac{1}{2}\int_{P_{O_2}'}^{P_{O_2}''} D_O dlnP_{O_2}$$

Since k_p is proportional to the diffusion coefficient (D_M & D_O) and oxygen partial pressure (P_{O_2}) gradient, furthermore k_p is declared following the Arrhenius equation.

$$k_p \approx D_o \Delta P_{O_2} exp\left(\frac{-Q}{RT}\right)$$

Finally, the oxide thickness growth can be written as:

$$x = D_o \Delta P_{O_2} exp\left(\frac{-Q}{RT}\right)\sqrt{t}.$$

From the above equation, the growth of oxide film strongly relates to oxygen diffusivity, oxygen partial pressure, activation energy (Q), temperature, and time.

Based on the above theoretical explanation, pre-oxidized specimens in this study are prepared by choosing temperature as the variable parameter. Temperature is chosen as a variable parameter because it is easy to control. Oxide film also can be grown in

relatively short periods. Six different formations of pre-oxide films from each specimen are prepared in an air environment at 300, 450, 600, 750, 900, and 1050 °C annealing temperatures. All the processes are performed on a muffle furnace. These processes produce 28 types of specimens with different pre-oxide formations from 4 types of materials, as illustrated in Table 2.2.

Table 2.2. Prepared specimens to be exposed with CsOH Precursor.

	RT.	**300 °C**	**450 °C**	**600 °C**	**750 °C**	**600 °C**	**1050 °C**
SS 304	√	√	√	√	√	√	√
SS 321	√	√	√	√	√	√	√
Inconel 600	√	√	√	√	√	√	√
X-750	√	√	√	√	√	√	√

Although oxide film variation may exist between dry and wet environments (Pedeferri, 2018, pp. 423–445, 589–610), however, they typically have a similarity that is strongly affected by oxygen potential (Noguchi and Yakuwa, 2016; Sequeira, 2019). Based on that fact, the prepared pre-oxidized specimens must be appropriate to represent various environmental conditions that may occur.

2.2.4 Cs Exposure Procedures

Liquid CsOH and solid materials interaction may happen in various ways depending on the normal operation or accident scenarios. In the case of a severe accident, saturated gaseous CsOH becomes liquid droplets and interacts with the material structure (Auvinen *et al.*, 2000; Roki *et al.*, 2008; Mishra *et al.*, 2019, 2020). CsOH could be dissolved by the coolant, flow through the leakage parts, and react with the structural materials (Firnhaber *et al.*, 1996; Watanabe, Yamada and Ohsaki, 2009; Deason, 2013). These mechanisms may happen in various temperatures and environmental conditions. To avoid a complicated study that involves too many parameters, this liquid CsOH and solid materials interaction is conducted following a simplified procedure. That procedure is designed by considering the scope of the study to observe the correlation between Cs chemisorption with the oxidation and solute elements.

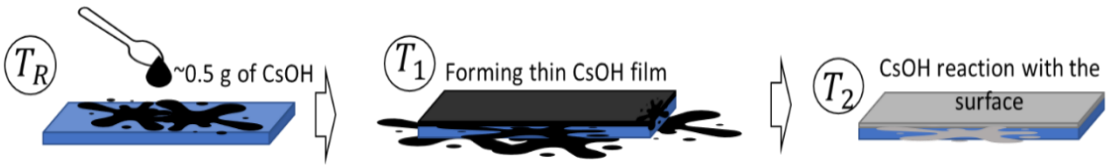

Figure 2.6. CsOH coating and solid-liquid interaction procedures.

As illustrated in Figure 2.6, liquid CsOH and solid structural material interaction are designed by directly putting CsOH precursor on the surface of target materials, which then be annealed at a CsOH melting temperature of 272 °C (Gurvich *et al.*, 1997; Kissane, 2009; Gouëllo *et al.*, 2018). By following this mechanism, a thin film of CsOH on the surface of the target material as shown in Figure 2.7 can be produced. Furthermore, CsOH-coated specimens are then treated at their respective target temperature.

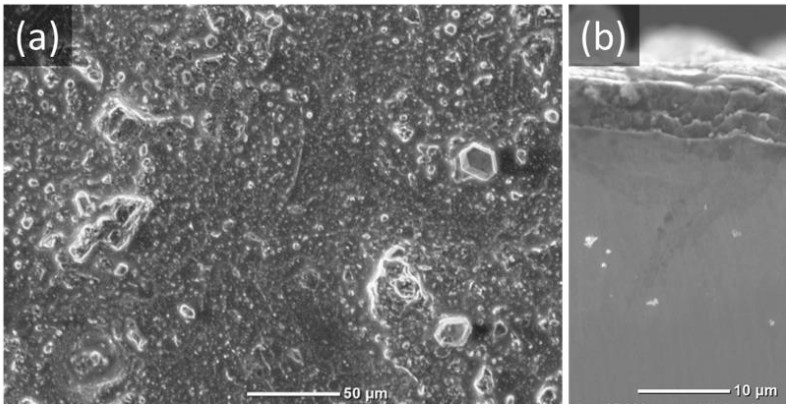

Figure 2.7. CsOH film on specimens treated at 272 °C for 1 hour, which is observed by (a) surface, and (b) cross-sectional SEM.

CsOH precursor exposure is carried out together with unoxidized specimens which were divided into 6 groups according to their temperature treatment (300, 450, 600, 750, 900, and 1050 °C). Each group consisted of 8 specimens composed of 4 unoxidized specimens from each type of material and 4 pre-oxidized specimens which are annealed at the same temperature as their CsOH precursor exposure temperature.

CsOH precursor with the specimen's interaction is performed following three steps as illustrated by Figure 2.8. These steps are started by putting CsOH precursor on the surface of specimens, forming a thin CsOH film on the target specimens, then precursor and specimen reaction at the respective temperatures. Around 0.5 grams of CsOH be put carefully on the surface of each specimen and arranged in such a way to

make it relatively uniform. All the CsOH-covered specimens from the same group are then placed in the heater on a flat surface with about 3 cm between each specimen. The heater temperature then firstly be set from room temperature (T_R) to reach the CsOH melting point at 272 °C, (T_1) for ~30 minutes and maintained for 1 hour. The purpose of this procedure is to form a thin CsOH layer on each target specimen. Thereafter, the temperature is increased to respective points (T_2) and maintained for 6 hours. Six different T_2 with wide temperature ranges, starting from 300, 450, 600, 750, 900, and 1050 °C are chosen to capture the wide temperature range of normal operation and severe accident environment. Six hours of temperature treatment are carried out to give appropriate time for crystallization of newly formed compounds, so they become easier to be identified by XRD. Finally, the specimens are taken out from the heater after reaching RT which needs about 3 hours or more depending on the T_2. All of these processes are conducted in an air environment with ~20% of oxygen.

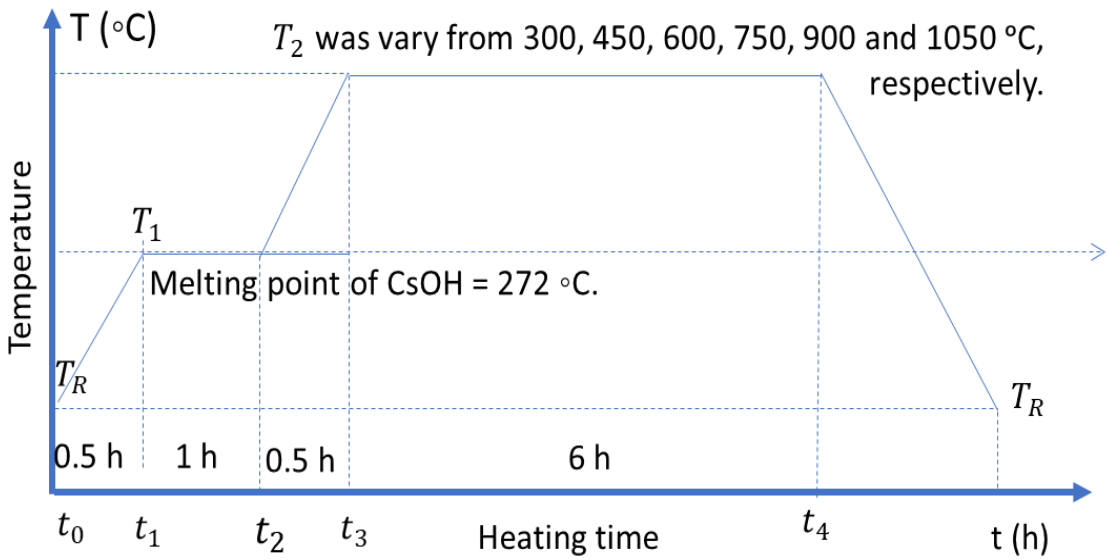

Figure 2.8. Temperature setting during CsOH and specimens' interaction.

The remaining CsOH precursor and reaction time at each temperature treatment must be varied due to the CsOH evaporation rate differences. These conditions contribute to the amount of chemisorbed Cs that should be considered during the analysis. Because of that, preliminary tests as shown in Appendix A are conducted to evaluate these parameters.

2.2.5 Soaking Procedure

Cs may retain on the surface physically and/or chemically. Physical retention happens such as by adhesion. In another way, physical retention may be followed by a chemical reaction that makes Cs chemically adsorbed and well retained in the material. That phenomenon is known as chemisorption (Job and Rüffler, 2016, p. 392).

Several possibilities may happen with the precursor and/or the newly formed Cs compounds during the CsOH exposure. Some of them such as both CsOH precursor and the newly formed Cs-related and/or -unrelated compounds evaporate at different rates depending on the temperature treatment; a part of the CsOH precursor remain on the surface, and the new compounds including Cs- and non-Cs-related compounds are formed but do not retain strongly. All these non-chemisorption-related compounds should be removed. This process is important to ensure identified Cs compounds in specimens are firmly well-chemisorbed.

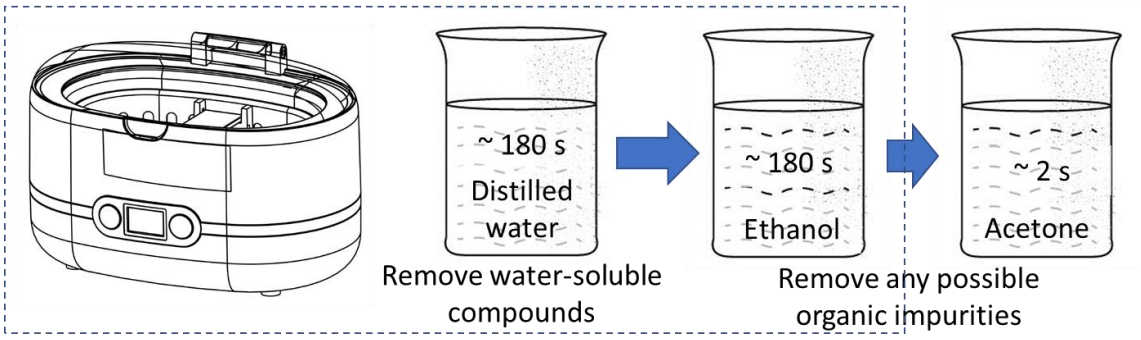

Figure 2.9. Schematic procedure during soaking to remove CsOH residual and non-chemisorbed Cs compounds.

Cs chemisorption identification is conducted by following the soaking mechanism using an ultrasonic cleaner, distilled water, ethanol, and acetone following the procedure shown in Figure 2.9. Each specimen is firstly put in a beaker glass containing ~200 ml distilled water and then stirred on an ultrasonic cleaner for 180 seconds. After that, the specimen is stirred again on ~200 ml ethanol for 180 seconds. The last mechanism is to dip the specimens in the ~200 ml acetone for around 2 seconds. Each specimen is treated using the new distilled water and ethanol to make sure the soluble compounds do not contaminate the other specimens. However, acetone is used

for several specimens considering the remaining soluble compounds and impurities during the dipping should be very low.

Distilled water is used because of CsOH precursors, and some newly formed compounds are easily dissolved in water as commonly happens in LWR, including such scenarios of other types of reactors. While ethanol and acetone are good solvents for organic compounds which may exist on the specimens as an impurity during the handling. It is expected that all Cs compounds, and other impurities, can be removed during the soaking.

2.2.6 Synthesis of Cs Compounds

2.2.6.1 Cs-Fe-Cr-O Compounds

Cs_2FeO_4 is formed at lower temperatures, especially from specimens treated at 300 – 600 °C. While Cs_2CrO_4 exists from specimens treated up to 900 °C. Although as suggested by (Kopelev, Popov and Val'kovskii, 1994), Cs_2FeO_4 may be decomposed to be $CsFeO_{2.5}$, however, it is not clear why $CsFeO_{2.5}$ cannot be observed from the main specimens in this experiment. Therefore, an analytical test for Cs-Fe-Cr-O compounds is conducted to identify the formation and decomposition of Cs_2FeO_4, observing the characteristic of Cs_2CrO_4, and reacting between $CsFeO_{2.5}$ with chromium oxides. This observation is conducted following 3 steps; identifying the formation and decomposition of Cs_2FeO_4, observing the characteristic of Cs_2CrO_4, and reacting between $CsFeO_{2.5}$ with Cr_2O_3.

2.2.6.1.1 Cs-Fe-O Compounds

Cs_2FeO_4 is assumed to be formed by following the chemical reaction:

$$6\ CsOH{\cdot}H_2O + Fe_3O_4 + 2.5\ O_2 \rightarrow 3\ Cs_2FeO_4 + 9\ H_2O.$$

Because of that, 5.54 g of $CsOH{\cdot}H_2O$ is mixed with 1.19 g of Fe_3O_4 with a molar ratio = 6:1.

2.2.6.1.2 Cs-Cr-O compounds

Cs_2CrO_4 is assumed to comply with the following chemical reaction:

$$4\ CsOH{\cdot}H_2O + Cr_2O_3 + 1.5\ O_2 \rightarrow 2\ Cs_2CrO_4 + 6\ H_2O.$$

Based on that reaction, 6.717 g of $CsOH{\cdot}H_2O$ is mixed with 1.519 g of Cr_2O_3 with a molar ratio = 4:1.

2.2.6.1.3 Reaction between $CsFeO_{2.5}$ and Cr_2O_3

Chromium oxides, in the form of Cr_2O_3 and may also in the form of $NiCr_2O_4$ and $FeCr_2O_4$ spinel are predicted could react with cesium iron oxides, particularly $CsFeO_{2.5}$ to be more stable Cs_2CrO_4, which make it cannot be observed from main specimens. To validate this hypothesis, the reaction is assumed to follow:

$$4\ CsFeO_{2.5} + Cr_2O_3 + 0.5\ O_2 \rightarrow 2\ Cs_2CrO_4 + 2\ Fe_2O_3.$$

Meanwhile, $CsFeO_{2.5}$ is produced by the following reaction:

$$3\ CsOH{\cdot}H_2O + Fe_3O_4 + O_2 \rightarrow 3\ CsFeO_{2.5} + 4.5\ H_2O.$$

Because of that, 6.717 g of $CsOH{\cdot}H_2O$ is mixed with 3.087 g of Fe_3O_4 and then treated at 600 °C for 6 hours. Furthermore, the formed $CsFeO_{2.5}$ is then reacted with 1.519 g of Cr_2O_3.

All those mixtures are added with ~1 ml distilled water as the solvent on ceramic mortals then stirred for ~2 minutes. These mixed precursors are furthermore divided into 6 parts and treated at 6 different temperatures in the same environment with the procedure explained in Section 2.2.4.

2.2.6.2 Cs-Al-Ti-Si-O Compounds

Tiny particles of Cs compounds containing Al and Ti, including some also related to Si are observed on the specimens of the main experiment which are treated at 300 and 450 °C. These particles are only around 2 μm, which makes them difficult to be analyzed using currently utilized techniques. These particles might be fabricated to be TEM samples by using the FIB machine. However, that option is not visible, because the available FIB machine in our laboratory is not equipped with EDS. This makes it difficult to find those small Cs particles during fabrication. Another technique, such as Raman spectroscopy is also unable to detect those small particles due to high background intensity. Therefore, an alternative indirect characterization by simulating the formed Cs compounds is utilized to solve this problem.

Four different mixtures are prepared according to the approximate composition of each Cs compound detected by point analysis of quantitative EDS. The average atomic ratio of Cs, Al, Si, and Ti in SS 304, SS 321, Inconel 600, and X-750 are about 3.35/2.72/1, 4.45/1.26/1/6.69, 2.52/3.23/1/0.5, and 2.80/3.13/0.10/12.76 respectively. Since the atomic ratio is proportional to the molar ratio, the mass of each precursor for the additional experiment furthermore can be determined. The mass of each precursor used during the synthesis is shown in Table 2.3. These precursors which are representing Cs compounds in each specimen then mixed in the ceramic mortar. Around ~1ml distillate water is added as a solvent, then stirred for around 2 minutes to increase the solution homogeneity.

Table 2.3. Precursor composition to simulate Cs compounds found in each post-soaked material.

Simulated Cs particles in	**$CsOH{\cdot}H_2O$ (g)**	**Al_2O_3 (g)**	**SiO_2 (g)**	**TiO_2 (g)**
SS 304	5.62	2.77	0.60	-
SS 321	7.47	1.28	0.60	5.34
Inconel 600	4.23	3.29	0.60	0.39
X-750	4.70	3.19	0.06	10.19

Synthesizing procedure is conducted following the same environment and temperature setting as in the main experiment as explained in Section 2.2.4. Mixed precursors are placed on Pt crucible, then heated at CsOH melting point, 272 ^{o}C for 1 hour. Thereafter, the heater is set to the intended temperatures, at 300, 450, 600, 750, 900, and 1050 °C, and maintained for 6 hours. The temperature changes from room temperature (RT) to 272 ^{o}C and each target temperature is set for 30 minutes. Meanwhile, the cooling period from target temperatures to RT varied from ~3 hours or more. All these procedures are conducted without flow in an air environment.

2.3 Characterization Techniques

Specimen characterization is performed for each step using XRD and SEM/EDS, supported by Optical Microscope (OM), plasma coater, and ion milling machine for cross-sectional fabrication. Thermogravimetry – Differential Thermal Analysis (TG-DTA) is also utilized to support the analytical tests.

Metallographic OM manufactured by Nikon is used for the preliminary characterization, especially during specimen preparation. OM is used particularly to ensure all prepared specimens are polished properly. Color information from OM indicates their electron excitation is applied to support the identification of oxide compounds (Fox, 2007, p. 27; Orna, 2013).

Formed Cs compounds and other related oxides are identified using MiniFlex 600 XRD machine from Rigaku. The machine is operated at 40 kV accelerating voltage and 15 mA emission current with Cu-Kα radiation (λ = 0.154059 nm). Data acquisition is performed from 20° to 80° 2θ with the size of 1.250° and 2.5 seconds per step collection time. X-ray penetration depth (P.D.) as shown in Table 2.4 is predicted based on the mass attenuation coefficient (MAC). X-ray penetration depth is important to predict the detection limit of XRD that is used to measure bulk specimens.

Table 2.4. The penetration depth of X-rays for each target specimen.

Material	**Density (g/cm^3)**	**Penetration depth (μm)**
Stainless Steel	8.00	21.105
Inconel	8.47	22.148
Fe_2O_3	5.24	39.809
Cr_2O_3	5.22	50.013
NiO	6.67	85.323
$CsOH{\cdot}H_2O$	3.68	47.073
$CsFeO_2$	4.96	17.085
Cs_2CrO_4	4.13	20.758

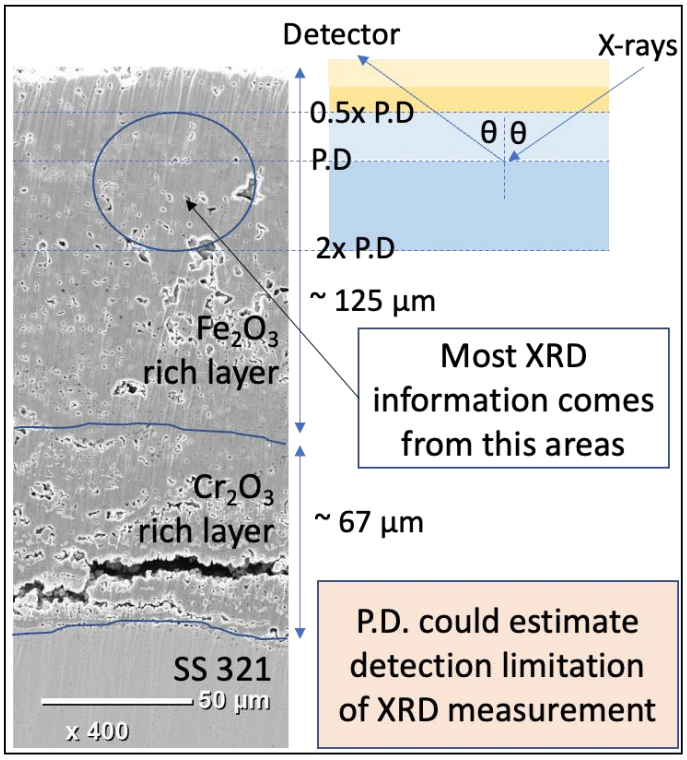

Figure 2.10. X-ray penetration depth during XRD measurement of bulk specimens.

Elements distribution, surface, and cross-sectional morphology observation are performed using SEM Jeol JCM-6000Plus equipped with EDS equipped with embedded software that can carry out quantitative analysis using the atomic number, absorption, and fluorescence (ZAF) correction method (Williams and Carter, 2009, p. 488), with a detection limit of ~0.15 at.%. The machine is operated at 15 kV acceleration voltage and 7.475 nA irradiation current in a high vacuum environment. Electron penetration analysis by using CASINO (Monte Carlo Simulation of Electron Trajectory) code is also conducted to define the detection limit of quantitative EDS measurement as shown in Figure 2.11. Based on CASINO simulation (Drouin *et al.*, 2007), the spatial resolution of utilized SEM/EDS is around 0.46 μm^2 with penetration depth for each material varies, as shown in Table 2.5.

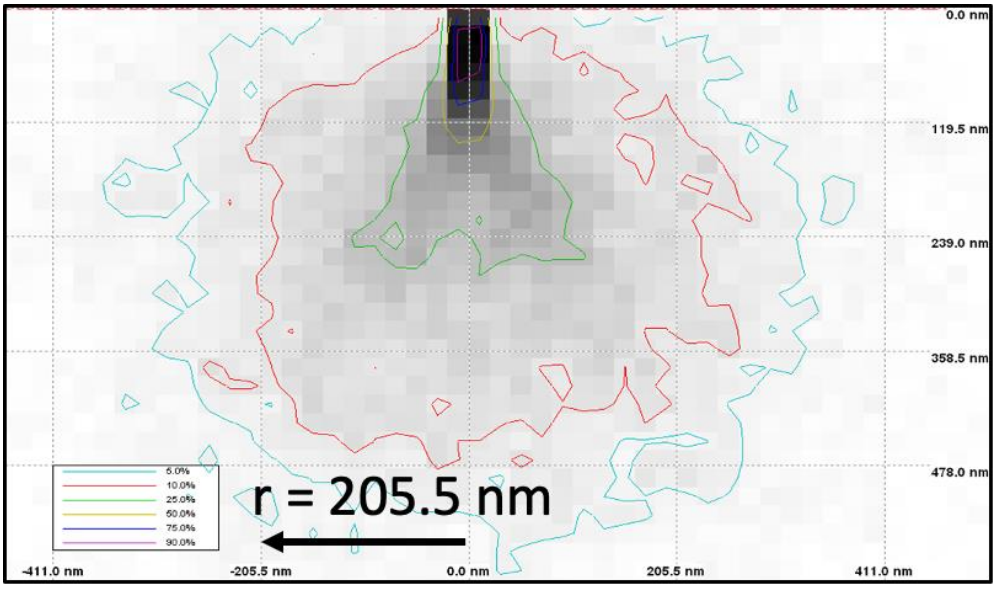

Figure 2.11. CASINO simulation to predict electron penetration depth during SEM/EDS characterization.

Table 2.5. Electron penetration depth for each material during SEM/EDS characterization.

Material	**Penetration depth (nm)**
Stainless steel	239
Inconel	242
CsOH	400
Fe_2O_3	800
Cr_2O_3	752

TG-DTA 2000SA/MS 9610 manufactured by Bruker is utilized to analyze mass changes due to temperature, which is closely related to several physicochemical mechanisms, such as dehydration, chemical reaction, decomposition, evaporation, etc. That machine is operated in an air environment between RT and 1050 °C with a changing temperature of 5 °C/minute. Analysis of TG-DTA graphs is conducted following the guidelines mentioned by (Gabbott, 2008; Wagner, 2018).

Ion milling IM4000Plus equipped with argon-ion source operated at 6 kV acceleration voltage is used for cross-sectional fabrication. Gold plasma coater (Sputter Coater (Au) SC-701) and resin are also utilized for some specimens to help cross-sectional fabrication and to increase conductivity during SEM/EDS observation.

2.4 Summary

The experimental procedures are designed by considering the objectives of this study and the previous experiment techniques. The simplified procedures consisted of some major steps, starting from material and precursor selections, growing pre-oxide film, CsOH precursor exposure, and Cs chemisorption identification. Additional analytical tests are also conducted to identify the characteristics of newly identified Cs compounds detailly.

$CsOH{\cdot}H_2O$ provided by Combi-Blocks Inc. with ~95% purity is chosen as the precursor. $CsOH{\cdot}H_2O$ characteristics are measured using XRD and TG-DTA to get basic information for post-CsOH and materials interaction analysis.

Four types of common nuclear structural materials are chosen. These materials have several similarities and differences regarding their constituent elements and oxidation characteristics, especially those related to solutes Al and Ti. These four selected alloys are SS 304, SS 321, Inconel 600 & X-750 provided by Nilaco Corporation. These alloys are cut with the size of around 10 mm x 10 mm x 0.5 mm and appropriately polished.

Twenty-eight types of pre-oxidized specimens are prepared from 4 selected materials. These pre-oxidized specimens are prepared by an annealing mechanism using a muffle furnace in an air environment.

Cs exposure is performed group by group. Each group consists of 4 unoxidized and 4 pre-oxidized specimens from each material, that are annealed at respective temperatures. Each specimen furthermore is exposed to ~0.5 g of CsOH precursor and then put on the heater in an air environment without flow. The heater temperature is set at 272 °C to form a thin CsOH layer on the surface before being treated at the respective point like their annealing temperatures during pre-oxidized specimens' preparation.

Soaking is performed for all specimens using the ultrasonic cleaner in distilled water, ethanol, and acetone to remove any CsOH residual and/or the newly formed compounds which may exist but are not well-chemisorbed.

All specimens of each step are characterized using OM, XRD, surface, and cross-sectional SEM/EDS support by ion milling, Au Sputter Coater, and TG-DTA.

2.5 References

Auvinen, A. et al. (2000) 'Vaporisation rates of CsOH and CsI in conditions simulating a severe nuclear accident', Journal of Aerosol Science, 31(9), pp. 1029–1043. doi: 10.1016/S0021-8502(00)00027-6.

Deason, W. (2013) Characterization of Fission Product Transport in a Gen. IV Gas-Cooled Fast Reactor Plant Utilizing Vented Fuel.

Ding, H. et al. (2018) 'Development of emergency planning zone for high temperature gas-cooled reactor', Annals of Nuclear Energy. Elsevier Ltd, 111, pp. 347–353. doi: 10.1016/j.anucene.2017.08.039.

Do, T. M. D. et al. (2017) 'Vaporization and deposition of cesium dimolybdate, $Cs_2Mo_2O_7$', Journal of Nuclear Science and Technology, 54(3), pp. 330–336. doi: 10.1080/00223131.2016.1273146.

van Dorsselaere, J. P. et al. (2017) 'The ASTEC Integral Code for Severe Accident Simulation', Nuclear Technology, 165(3), pp. 293–307. doi: 10.13182/NT09-A4102.

Drouin, D. et al. (2007) 'CASINO V2.42—A Fast and Easy-to-use Modeling Tool for Scanning Electron Microscopy and Microanalysis Users', Scanning, 29(3), pp. 92–101. doi: 10.1002/sca.20000.

Ezugwu, E. O. (2004) 'High Speed Machining of Aero-Engine Alloys', Journal of the Brazilian Society of Mechanical Sciences and Engineering, 26(1), pp. 1–11. doi: 10.1590/S1678-58782004000100001.

Firnhaber, M. et al. (1996) 'International Standard Problem ISP37: VANAM M3. A Multicompartment Aerosol Depletion Test with Hygroscopic Aerosol Material'. Moulineaux: Committee on the Safety of Nuclear Installations OECD Nuclear Energy Agency.

Fox, M. A. (2007) Colour Chemistry, Glossary for the Worldwide Transportation of Dangerous Goods and Hazardous Materials. Cambridge: Royal Society of Chemistry (RSC Paperbacks). doi: 10.1039/9781847550590.

Gabbott, P. (2008) Principles and applications of thermal analysis. Blackwell Pub.

Gouëllo, M. et al. (2018) 'A Scoping Study of the Chemical Behavior of Cesium Iodide in the Presence of Boron in the Condensed Phase (650 °C and 400 °C) Under Primary Circuit Conditions', Nuclear Technology. Taylor & Francis, 203(1), pp. 66–84. doi: 10.1080/00295450.2018.1429111.

Griffiths, M. (2019) Ni-Based Alloys for Reactor Internals and Steam Generator Applications, Structural Alloys for Nuclear Energy Applications. Elsevier Inc. doi: 10.1016/b978-0-12-397046-6.00009-5.

Gurvich, L. V. et al. (1997) 'Thermodynamic properties of alkali metal hydroxides. Part II. Potassium, rubidium, and cesium hydroxides', Journal of Physical and Chemical Reference Data, 26(4), pp. 1031–1110. doi: 10.1063/1.555996.

Hoffelner, W. (2013) Materials for Nuclear Plants, Materials for Nuclear Plants. London: Springer London. doi: 10.1007/978-1-4471-2915-8.

Humrickhouse, P. W. (2011) HTGR Dust Safety Issues and Needs for Research and Development. Idaho. doi: 10.2172/1023483.

Job, G. and Rüffler, R. (2016) Physical Chemistry from a Different Angle, Springer. Cham: Springer International Publishing. doi: 10.1007/978-3-319-15666-8.

Kissane, M. P. (2009) 'A review of radionuclide behaviour in the primary system of a very-high-temperature reactor', Nuclear Engineering and Design, 239(12), pp. 3076–3091. doi: 10.1016/j.nucengdes.2009.09.012.

Kobata, M. et al. (2018) 'Chemical form analysis of reaction products in Cs-adsorption on stainless steel by means of HAXPES and SEM/EDX', Journal of Nuclear Materials. Elsevier B.V, 498, pp. 387–394. doi: 10.1016/j.jnucmat.2017.10.035.

Kopelev, N. S., Popov, A. I. and Val'kovskii, M. D. (1994) 'Properties of the products of CsxFeO2+0.5x thermal decomposition', Journal of Radioanalytical and Nuclear Chemistry Letters, 188(2), pp. 99–108. doi: 10.1007/BF02164943.

Kugeler, K., Nabielek, H., Buckthorpe, D. and Editors: Scheuermann, W., Haneklaus, N., Fütterer, M. (2017) The High Temperature Gas-cooled Reactor: Safety considerations of the (V)HTR-Modul. doi: 10.2760/270321.

Lahiri, A. K. (2017) Applied Metallurgy and Corrosion Control, Applied Metallurgy and Corrosion Control. doi: 10.1007/978-981-10-4684-1.

Li, C. et al. (2019) 'Chemical Forms of Important Fission Products in Primary Circuit of HTR-PM under Conditions of Normal Operation and Overpressure and Water Ingress Accidents: A Study with a Chemical Thermodynamics Approach', Science and Technology of Nuclear Installations, 2019, pp. 1–12. doi: 10.1155/2019/4251280.

Liu, P. et al. (2016) 'Study on air ingress of the 200 MWe pebble-bed modular high temperature gas-cooled reactor', Annals of Nuclear Energy, 98, pp. 120–131. doi: 10.1016/j.anucene.2016.07.029.

Martín-Fuertes, F. et al. (2007) 'Analysis of source term aspects in the experiment Phebus FPT1 with the MELCOR and CFX codes', Nuclear Engineering and Design, 237(5), pp. 509–523. doi: 10.1016/j.nucengdes.2006.07.006.

Merwe, J. J. Van Der (2009) Modelling Silver Transport in Spherical HTR Fuel. University of Pretoria. Available at: https://repository.up.ac.za/bitstream/handle/2263/28777/Complete.pdf?sequence=6&isAllowed=y.

Miradji F.; et al. (2019) 'Modelling of Cesium Chemisorption Under Nuclear Power Plant Severe Accident Conditions', in The 9th European Review Meeting on Severe Accident Research (ERMSAR2019). Prague.

Mishra, G. et al. (2019) ‘Hygroscopic growth of CsI and CsOH particles in context of nuclear reactor accident research’, Journal of Aerosol Science. Elsevier Ltd, 132(January), pp. 60–69. doi: 10.1016/j.jaerosci.2019.03.008.

Mishra, G. et al. (2020) ‘Study on CCN activity of fission product aerosols (CsI and CsOH) and their effect on size and other properties’, Atmospheric Research. Elsevier, 236(November 2019), p. 104816. doi: 10.1016/j.atmosres.2019.104816.

Miwa, S. et al. (2018) ‘Release and transport behaviors of non-gamma-emitting fission products and actinides in steam and hydrogen atmospheres’, Nuclear Engineering and Design. Elsevier, 326 (October 2017), pp. 143–149. doi: 10.1016/j.nucengdes.2017.11.017.

Miwa, S. et al. (2020) ‘Boron chemistry during transportation in the high temperature region of a boiling water reactor under severe accident conditions’, Journal of Nuclear Science and Technology. Taylor & Francis, 57(3), pp. 291–300. doi: 10.1080/00223131.2019.1671913.

Murty, K. L. and Charit, I. (2008) ‘Structural materials for Gen-IV nuclear reactors: Challenges and opportunities’, Journal of Nuclear Materials. Elsevier B.V., 383(1–2), pp. 189–195. doi: 10.1016/j.jnucmat.2008.08.044.

Nakajima, K. et al. (2018) ‘An experimental investigation for atmospheric effects on Cs chemisorption onto stainless steel’, Progress in Nuclear Science and Technology, 5(0), pp. 168–170. doi: 10.15669/pnst.5.168.

Nakajima, K. et al. (2019) ‘Study on chemisorption model of cesium hydroxide onto stainless steel type 304’, International Conference on Nuclear Engineering, Proceedings, ICONE, 2019-May. doi: 10.1299/mej.19-00564.

Nishioka, S. et al. (2019) ‘An experimental investigation of influencing chemical factors onCs-chemisorption behavior onto stainless steel’, Journal of Nuclear Science and Technology. Taylor & Francis, 00(00), pp. 1–8. doi: 10.1080/00223131.2019.1633968.

Noguchi, M. and Yakuwa, H. (2016) ‘Lecture on Fundamental Aspects of High Temperature Corrosion and Corrosion Protection Part 1: Basic Theory’. Ebara Engineering Review, pp. 1–11. Available at: https://www.ebara.co.jp/about/technologies/abstract/detail/__icsFiles/afieldfile/2017/03/08/252_P31_1.pdf.

Orna, M. V. (2013) The Chemical History of Color, Springer. Berlin, Heidelberg: Springer Berlin Heidelberg (SpringerBriefs in Molecular Science). doi: 10.1007/978-3-642-32642-4.

Pedeferri, P. (2018) Corrosion Science and Engineering. Pedeferri,. Cham: Springer International Publishing (Engineering Materials). doi: 10.1007/978-3-319-97625-9.

Rizaal, M. et al. (2021) ‘Revaporization Behavior of Cesium and Iodine Compounds from Their Deposits in the Steam–Boron Atmosphere’, ACS Omega, 6(48), pp. 32695–32708. doi: 10.1021/acsomega.1c04441.

Roki, F.-Z. et al. (2015) ‘Improvements in the assessment of the thermodynamic properties of condensed and gaseous phases of the CsOH compound’, The Journal of Chemical Thermodynamics. Academic Press, 80, pp. 147–160. doi: 10.1016/j.jct.2014.08.021.

Roki, F. Z. et al. (2008) ‘Thermodynamic study of the CsOH(s,l) vaporization by high temperature mass spectrometry’, The Journal of Chemical Thermodynamics, 40(3), pp. 401–416. doi: 10.1016/j.jct.2007.09.013.

Sehgal, B. R. (2012) Nuclear Safety in Light Water Reactors, Nuclear Safety in Light Water Reactors. Elsevier. doi: 10.1016/C2010-0-67817-5.

Sequeira, C. A. C. (2019) High Temperature Corrosion. Hoboken, NJ, USA: John Wiley & Sons, Inc. doi: 10.1002/9781119474371.

Susan Jackson, A. S. (2016) Structural Alloys for Power Plants: Operational Challenges and High-temperature Materials, Journal of Chemical Information and Modeling. doi: 10.1017/CBO9781107415324.004.

Wagner, M. (2018) Thermal Analysis in Practice Fundamental Aspects.

Was, G. S. (2017) 'Fundamentals of Radiation Materials Science', in Fundamentals of Radiation Materials Science. Second Edi. New York, NY: Springer New York, pp. 3–76. doi: 10.1007/978-1-4939-3438-6_1.

Watanabe, A., Yamada, K. and Ohsaki, M. (2009) 'FP Aerosol Trapping Effect Along the Leakage Paths of Degraded Containment Penetrations During a Severe Accident (II) Decontamination Factor at the Containment Penetrations and Its Application to Actual Plant', Transactions of the Atomic Energy Society of Japan, 8(4), pp. 332–343. doi: 10.3327/taesj.J08.052.

Williams, A. D. (2011) Power Plant Life Management and Performance Improvement, Power Plant Life Management and Performance Improvement. doi: 10.1533/9780857093806.3.420.

Williams, D. B. and Carter, C. B. (2009) Transmission Electron Microscopy, Kobunshi. Boston, MA: Springer US. doi: 10.1007/978-0-387-76501-3.

Yvon, P. (2017) Structural Materials for Generation IV Nuclear Reactors, Structural Materials for Generation IV Nuclear Reactors. Elsevier. doi: 10.1016/C2014-0-03589-7.

(This page intentionally left blank)

Chapter 3

Oxidation of Nuclear Structural materials

(This page intentionally left blank)

Learning is about seeing things from a different perspective.

~Bob Selden

(This page intentionally left blank)

Chapter 3

Oxidation of Nuclear Structural Materials

3.1 Introduction

Oxidation is one of the important issues for nuclear structural materials. Oxidation can be defined as the spontaneous tendency of a metallic component to its original state which is thermodynamically stable (Pedeferri, 2018, p. 2). The Oxidation processes are closely related to the reduction mechanism followed by electron transfer between chemical species (Lahiri, 2017, pp. 178–180; Sequeira, 2019, p. 162). Oxidation is the process when an atom loses its electrons and increases its oxidation state. The reduction happens when an atom gains an electron and decreases its oxidation state. The oxidation and reduction mechanism may then be accompanied by the chemical reaction between those atoms to achieve a more stable thermodynamic position. The metal alloys that are usually used as structural material tends to corrode through the process of losing electrons then followed by a reaction with the surrounding atoms, which undergo a reduction process such as oxygen, hydrogen, acid compounds, and so on (Sequeira, 2019, pp. 196–339). Because the focus of attention lies on how to protect the structure of the material from corrosion, the mechanism that involves the reduction and oxidation processes is simply known as the oxidation mechanism (Noguchi and Yakuwa, 2016).

Oxidation may occur at any environmental condition affected by several factors, such as temperature, condensation, oxidation products and deposits, flow regime, and active-passive related parameters. Oxidation reaction rate increase doubles every 10 °C (Pedeferri, 2018, p. 113), which makes it one of the most influential factors. The increase of the oxidizing agent concentration, such as acid, carbon dioxides, etc. could accelerate the oxidation mechanism. While the oxidation products and deposition may be either beneficial or harmful for the materials, which depends on whether they can provide protection or accelerate the oxidation process. Flow rate can also have a positive and negative impact on the oxidation process. The flow rate may give a positive impact when it can facilitate passive film formation and avoid the deposit of oxidizing agents that could be hazardous for pitting. However high flow rate is dangerous when it can erode the protective layer and affect the mechanical wear.

Oxidation in nuclear structural materials varies greatly depending on the type of reactor and the operating environment (Hoffelner, 2013). However, it is generally affected by the above factors. The oxidation rate of the nuclear structural material under normal operation should be designed within the limit of the safety margin (Murty, 2013, p. 370; Chapman and Hess, 2018). Limiting oxidation rate can be performed either by adjusting the operating temperature and pressure, reducing the concentration of oxidizing agent which dissolved in the coolant, and/or adding a certain additive (Guentay *et al.*, 2005; Murty, 2013, pp. 322, 396). With all these efforts, the thickness of oxide film during normal operation could be maintained to be very thin. Slight differences in the oxide layer may occur in every part of the structural materials that are affected by the condition of the coolant, such as in the liquid, saturation vapor, water ingress accident, etc.

Rapid oxidation growth occurs during severe accidents (Clément *et al.*, 2003; Sehgal, 2012, pp. 94–95; Klein-Heßling *et al.*, 2014; Was and Ukai, 2019, p. 340). Rapid oxidation happens due to large temperature changing and complex environmental conditions. The temperature of LWR's core may exceed 2000 °C, followed by the melting process of the fuel and the surrounding structural materials (Sehgal, 2012, p. 132). Complex environmental conditions with a mixture of water vapor, air, hydrogen, fission products, and so on may happen and flow out following the leakage part of the reactor to the environment, which could be followed by significant oxidation. However, it is very difficult to predict the level of oxidation in each part of structural materials immediately after the accident. Because of that, variations of pre-oxidized specimens in this study are simply modeled on the air environment which is strictly controlled by temperature.

3.2 Oxidization Variation of Structural Materials

Pre-oxide film differences may contribute to the Cs chemisorption. Because of that, pre-oxide film identification should be an important step to build a solid foundation for the Cs chemisorption analysis. For that purpose, 28 different pre-oxide films are prepared from 4 types of materials as shown in Figures 3.1 and 3.2. These figures show that elemental composition differences and annealing temperature, contribute to the oxide film formation differences.

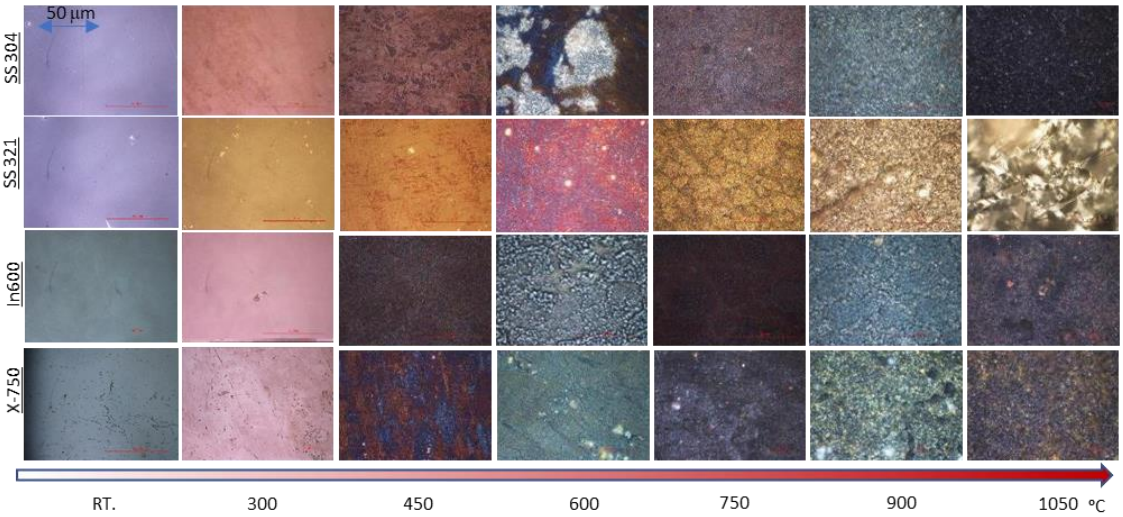

Figure 3.1. Optical examination of the prepared specimens.

Optical photographs in Figure 3.1 are taken using OM at 100 magnifications. That figure shows both color and surface morphologies differences between materials at each annealing temperature. These differences indicate the variation in the chemical compounds of oxides (Fox, 2007, pp. 27–28; Orna, 2013, pp. 29–44). Color information can be used as the first insight for the oxide compounds prediction. This is possible because each color variation represents a different quantum state, which is related to the amount of absorbed or released energy that furthermore affects the photon wavelength (Orna, 2013). The color of each compound and its correlation with the oxidation state moreover is described by (Eastaugh *et al.*, 2013) which is used in this study as the basis for preliminary identification.

Photographs of surface SEM characterization with 2000 times magnification are shown in Figure 3.2. SEM characterization can be used to distinguish the oxide film variation. The oxide film variation identification from the SEM photograph is performed based on the brightness differences, which are caused by the electron absorption and diffraction variations (Lahiri, 2017, p. 531). In addition, more precise identification can be conducted based on EDS mapping and point analysis (JEOL, 2012). However, since the element overlapping on the bulk samples may occur in the absence of chemical bonds, then the results of the SEM/EDS analysis cannot be used directly to judge the formation of chemical compounds.

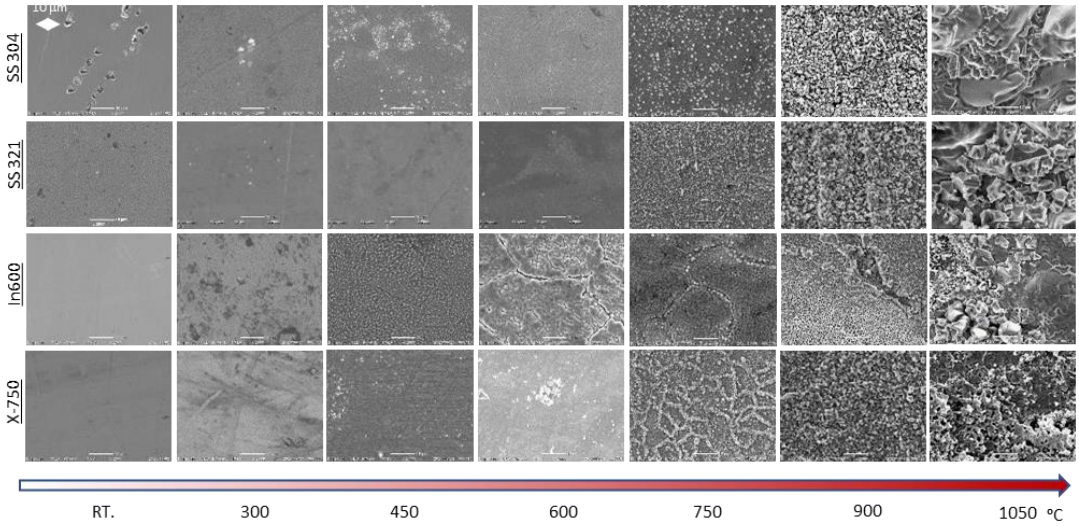

Figure 3.2. Surface morphology of pre-oxide specimens observed by SEM.

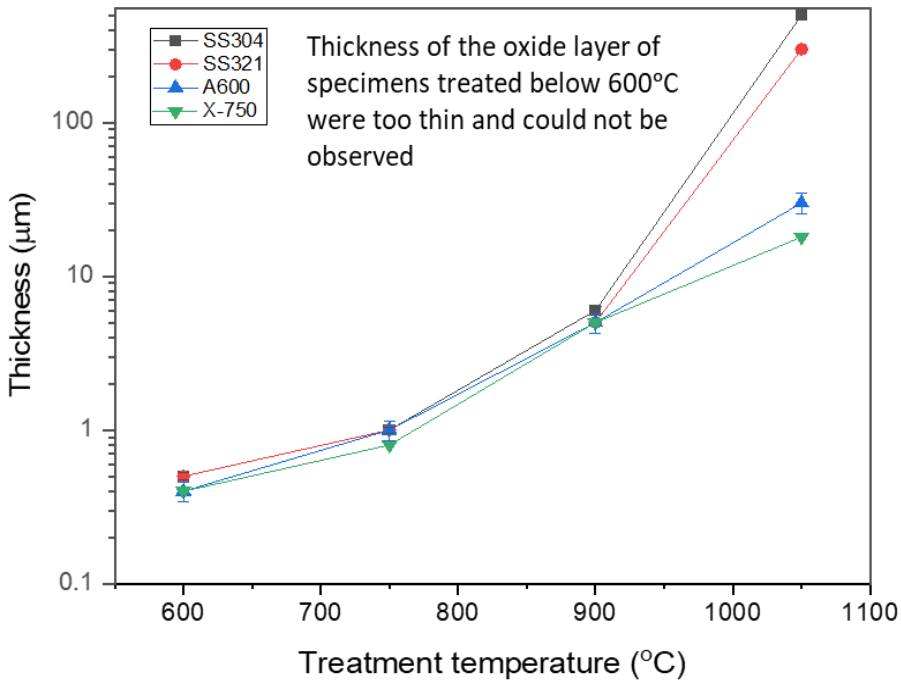

Figure 3.3. Pre-oxide film thickness of pre-oxide specimens annealed at 600 – 1050 °C.

Figure 3.3 shows the thickness variation of the oxide film between each material at each annealing temperature. The thickness is measured based on cross-sectional SEM observation. Cross-sectional SEM observation cannot be performed for the specimens annealed below 600 °C. This is because the oxide film thickness of specimens annealed below 600 °C is thin. Therefore, Figure 3.3 only shows data of specimens annealed at 600 - 1050 °C. From those materials, the oxide film of SS 304 grows fastest then followed by SS 321, Inconel 600, and X-750. The thicker oxide layer of SS 304 and 321 compared

with Inconel 600 and X-750 happen because Ni is thermodynamically more stable compared with Fe, as can be explained based on the Ellingham diagram as discussed by (Stratton, 2013). Oxidation properties differences between SS 304 and SS 321 as well as Inconel 600 and X-750 can be explained thermodynamically especially related to their solute elements (Ezugwu, 2004; Pedeferri, 2018).

A more detailed description of the pre-oxide specimen's characterization is explained in the following subchapter.

3.2.1 Pre-oxidized Film of SS 304

Although difficult to be observed, oxidation of SS 304 occurs starting from room temperature. The thickness of oxide films grows exponentially in line with the increase of the annealing temperature. These pre-oxide film structure changes, which are in line with the annealing temperature can be used to roughly describe the oxidation growth mechanism.

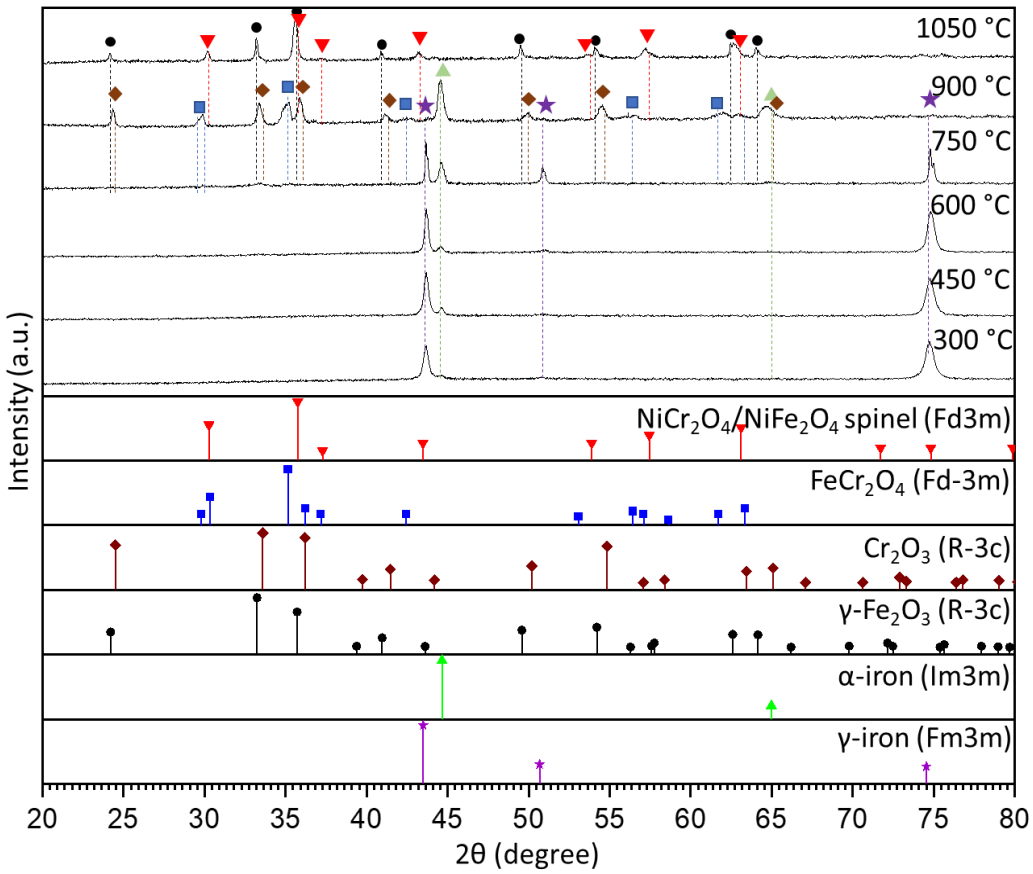

Figure 3.4 Oxide compounds identification of pre-oxidized SS 304 annealed at 300 – 1050 °C.

The color of SS 304 annealed at 300 °C is brown with some green areas, which indicates the formation of iron oxides and chromium oxides. However, SEM/EDS surface observation cannot identify the element overlapping, although some dark spots exist. XRD characterization as shown in Figure 3.4 shows similar peaks compared with unoxidized specimens. These indicate the formed oxide film is too thin.

Oxidation can be observed clearly from the specimen annealed at 450 °C. The optical photograph shows brown and dark brown colors covering all the surfaces and indicating the formation of iron oxides and chromium oxides. While observation using SEM/EDS shows several bright dots spread out on the darker areas, which are identified as Cr-O and Fe-O, respectively. XRD analysis shows the appearance of one new peak. However, that peak is strongly related to α' of steel rather than oxide compounds.

SS 304 specimen annealed at 600 °C shows rich colors, starting from bright, brown, purple, black, and green. These colors are related to several types of iron, nickel, and chromium oxides. Thicker formation of Fe-O including Cr-O can be observed to spread uniformly on the rough surface. Cross-sectional observation is also performed but it is difficult to identify the elemental distribution of oxide film because its thickness is only around 500 nm, which is almost like the spatial resolution of EDS used in this study. While XRD measures two new peaks. However, these peaks are identified as α' and γ' of iron.

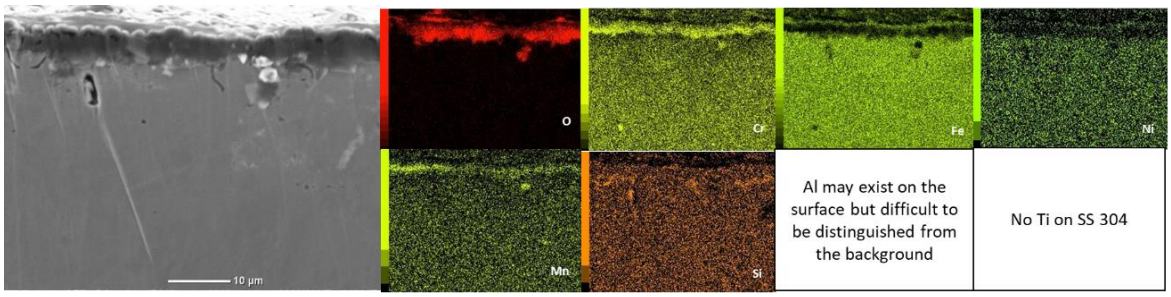

Figure 3.5. Cross-sectional oxide film morphology of pre-oxidized SS 304 treated at 900 °C.

The formation of oxide compounds can be observed using all techniques starting from specimens annealed at 750 °C. Various types of oxides including iron, chromium, nickel, and some minor elements are observed. Clear dots formation of Al-O and Mn-O can be identified by SEM/EDS spread around chromium oxides and iron oxides formation

with a thickness of ~1 μm. Some peaks from the XRD analysis are identified as Fe_2O_3 and the rest are closely related to α' and γ' of steel, including the spinel of $FeCr_2O_4$, $NiCr_2O_4$, and/or $NiFe_2O_4$.

The oxide film of specimens annealed at 900 °C consists of various compounds. Those compounds are mainly related to Fe, Cr, Ni, Mn, Al, and Si. As shown in Figure 3.5, the oxide film of the specimen annealed at 900 °C grows up to ~6 μm. The oxide film is mainly constructed in 2 layers, chromium oxides with Mn spinel as the inner layer, and the outer layer consisting of several compounds, especially the oxide of Fe, Ni, Cr, and Mn. Based on XRD analysis, most of these oxide compounds are related to Fe_2O_3, Cr_2O_3, and $FeCr_2O_4$, $NiCr_2O_4$, & $NiFe_2O_4$ spinels, which matches the analysis performed by (Fisher *et al.*, 2018) who simulate high temperature oxidation of SS 304 in the de-aerated water. The Si-enriched formation can be observed mainly filling the crack areas below the inner layer. However, the rest of Si also can be found on the outer oxide layer.

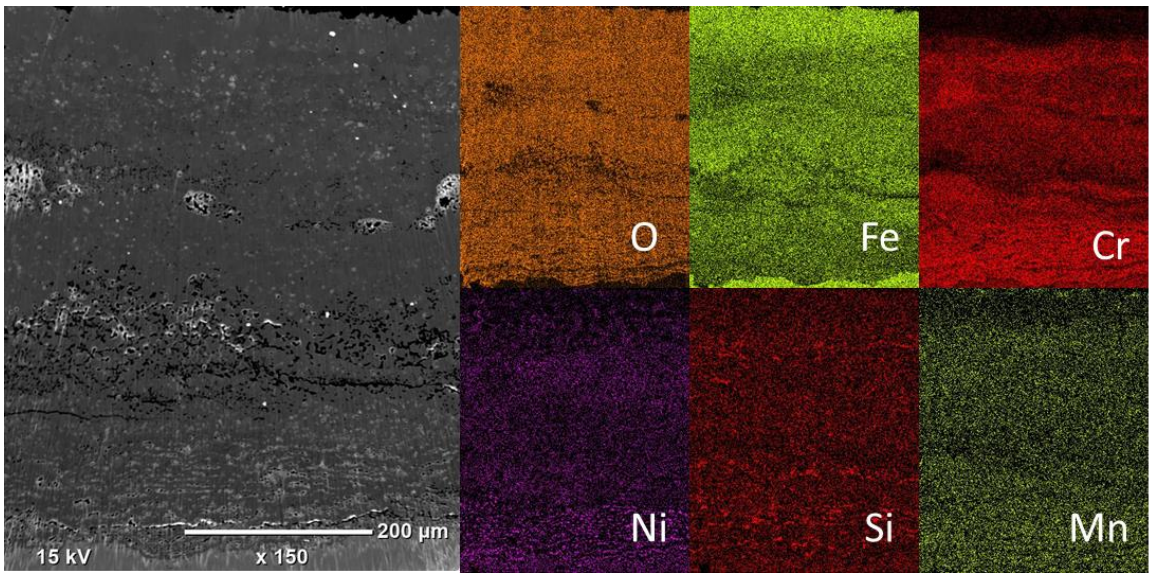

Figure 3.6. Cross-sectional oxide film morphology of pre-oxidized SS 304 specimen annealed at 1050 °C.

A very clear, but fragile oxide layer with a thickness of up to 700 μm can be observed from the specimen annealed at 1050 °C. The oxide layer of the specimen annealed at 1050 °C is dominated by the formation of iron oxides, iron-chromium oxides, and nickel-iron oxides. The color of this specimen is dominated by brown – solid black indicating the rich formation of Fe_2O_3. SEM/EDS observation on the surface shows the

specimen is dominated by Fe-O with some formation of Ni. While the X-ray penetration depth during XRD measurement for this specimen is predicted only ~39.8 μm, which is much smaller compared with its oxide film thickness. XRD measurement strongly suggests the main compounds are related to Fe_2O_3, and spinel of $NiCr_2O_4$, & $NiFe_2O_4$. However, by considering cross-sectional SEM/EDS analysis as shown in Figure 3.6, other compounds such as Cr_2O_3, and $FeCr_2O_4$ as identified from specimen annealed at 900 °C may exist in deeper parts. Cross-sectional SEM/EDS observation suggests both the outer and inner layers grow fast with the Si formation distributed in several parts in both the inner and outer oxide layer.

3.2.2 Pre-oxidized Film of SS 321

SS 321 has better high temperature oxidation resistance compared with SS 304. As shown in Figure 3.3, the oxide film growth of SS 321 is slower compared with that in SS 304. The better oxidation resistance of SS 321 is achieved due to the chromium oxide layer stabilization as the effect of Ti as had been explained by (Yvon, 2017).

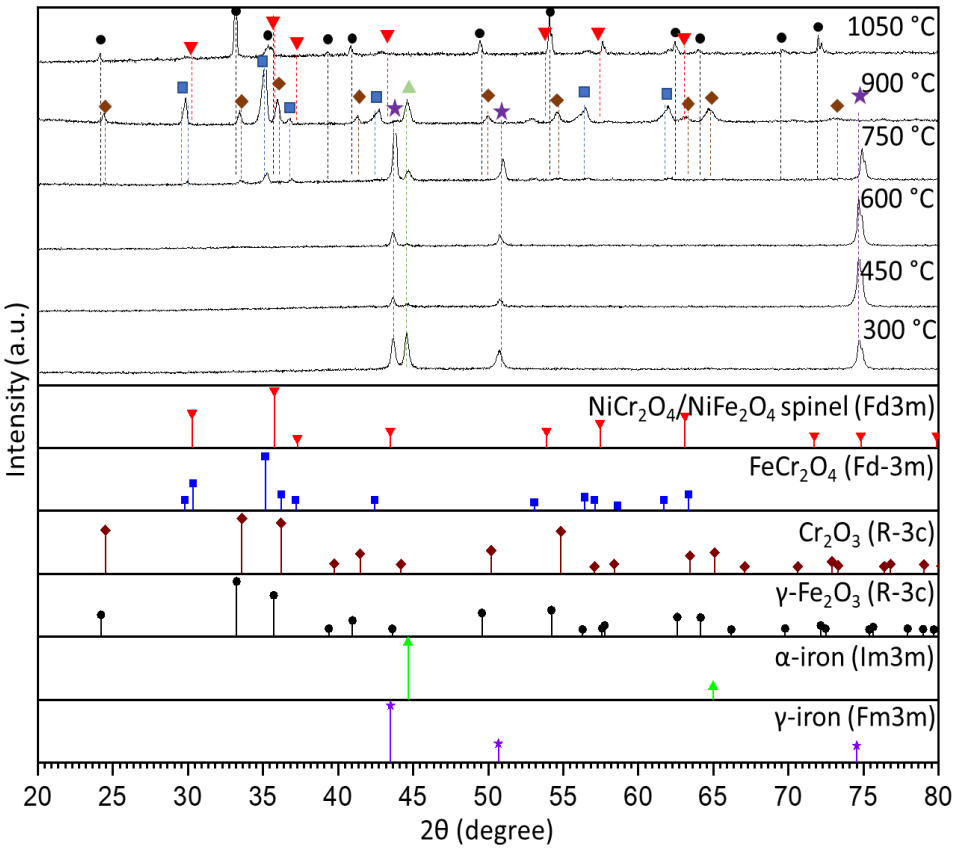

Figure 3.7. Oxide compounds identification of pre-oxidized SS 321 annealed at 300 – 1050 °C.

OM photograph of SS 321 specimen annealed at 300 °C shows brown and several dots of green colors. Those colors indicate the formation of iron oxides and chromium oxides. However, the formation of oxides cannot be identified clearly both using SEM/EDS and XRD.

The color of the specimen annealed at 450 °C is brown with some darker areas, indicating the formation of iron and chromium oxides. However, Surface SEM/EDS observation is unable to produce clear elemental mapping. While XRD analysis shows a similar pattern compared with the unoxidized specimen. XRD measurement shows small intensity peaks changing that indicate crystal structure transformation. It shows the oxide film on the specimen annealed at 450 °C is too thin.

Although surface SEM/EDS and XRD characterization also show similar results with specimen annealed at 450 °C, however, OM photograph of specimen annealed at 600 °C is more colorful with the combination of brown, red, green, black, and purple. These colors are related to the formation of iron oxides, chromium oxides, and nickel oxides. The surface of the specimen annealed at 600 °C is coarser compared with the specimen annealed at 450 °C.

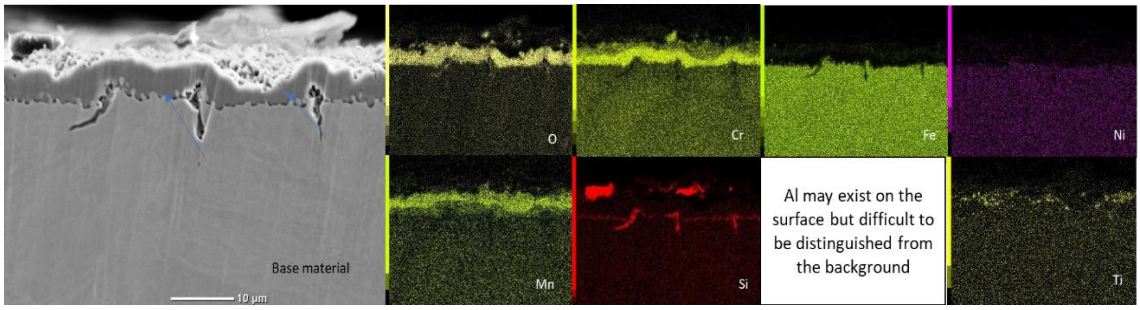

Figure 3.8. Cross-sectional oxide film morphology of pre-oxidized SS 321 treated at 900 °C.

Clear and rough formation of the oxide film can be observed from specimens treated at 750 °C. The color of the specimen becomes brown with dark brown to black around crack areas. These colors show the domination of iron oxides and chromium oxides respectively. These indications furthermore can be validated based on surface SEM/EDS analysis, which shows sandy surfaces related to the formation of iron oxides. The formation of manganese, silicon, titanium, and aluminum oxides is identified spread

around the surface. Relatively clear XRD peaks can be observed which are strongly related to Fe_2O_3, Cr_2O_3, and spinel of $FeCr_2O_4$, $NiCr_2O_4$, & $NiFe_2O_4$.

OM examination for the surface of SS 321 specimen annealed at 900 °C shows brown color with some silver spots. These colors are related to the formation of iron and chromium oxides. Surface and cross-sectional SEM/EDS observations show an almost similar formation compared with SS 304, except for the smoother surface and the existence of Ti-rich areas which are strongly related to titanium oxides and/or titanium carbide as shown in Figure 3.8. The chromium oxides construct the inner layer together with manganese chromium oxides spinel just upper it. Several oxides are formed on the outer layer dominated by Fe, Cr, and the rest are identified as Mn, Si, and Al. Silicon oxides are observed on the crack areas located between the base material and the inner layer. Some spots of Si can be found spread in the outer oxide layer. XRD analysis as shown in Figure 3.7 indicates SS 321 specimen annealed at 900 °C mainly consisted of similar compounds compared with the oxide film of SS 304, namely Fe_2O_3, Cr_2O_3, and spinel of $FeCr_2O_4$, $NiCr_2O_4$, and $NiFe_2O_4$. Although Mn, Si, and Ti can be detected by SEM/EDS observation, XRD peaks related to the compounds of these elements cannot be detected. This happened because the concentration of these elements is too small. Pre-oxide film at this temperature is relatively similar to the study done by (Pour-Ali *et al.*, 2020) which was performed in Ar-20 vol.% O_2 at 800°C.

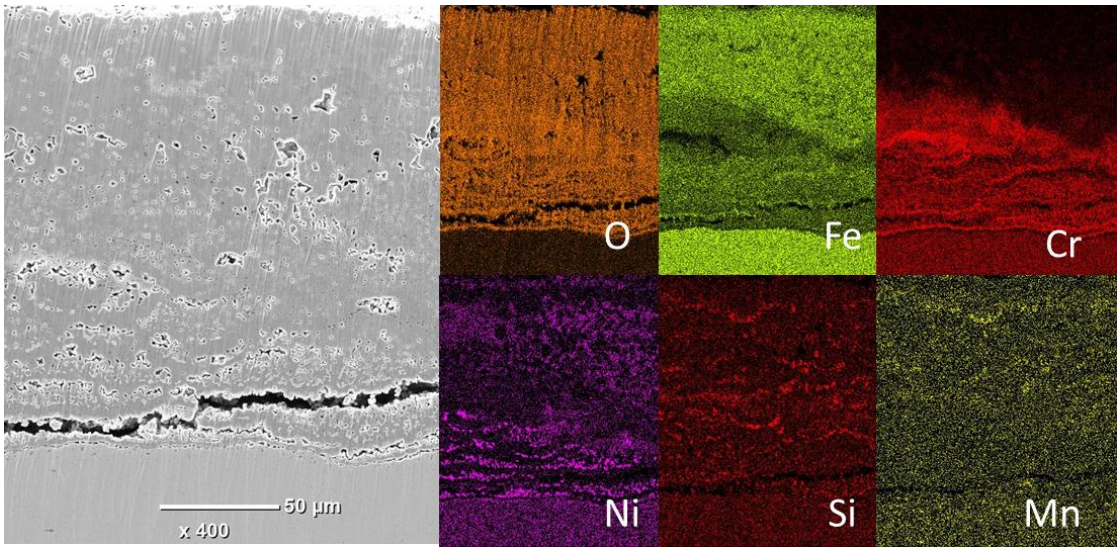

Figure 3.9. Cross-sectional oxide film morphology of pre-oxidized SS 321 specimen treated at 1050 °C.

Surface observation of SS 321 annealed at 1050 °C shows a very rough surface. Titanium oxides that are observed from the surface of the specimen annealed at 900 °C cannot be observed at the specimen annealed at this temperature. Although it has undergone very fast oxidation, its oxide structure is still robust compared to that in SS 304, which is annealed at the same temperature. The oxide film thickness of SS 321 annealed at 1050 °C is only less than one-fifth of SS 304 annealed at the same temperature. SEM/EDS cross-sectional analysis as shown in Figure 3.9 indicates the Si is distributed in both inner and outer layers like SS 304. However, the inner layer of SS 321 looks more robust, consisting of richer Cr, while the outer layer is relatively thinner. Based on these facts, the amount of Si in the oxide layer of SS 321 should be smaller compared with SS 304 which is annealed at the same temperature.

3.2.3 Pre-oxidized Film of Inconel 600

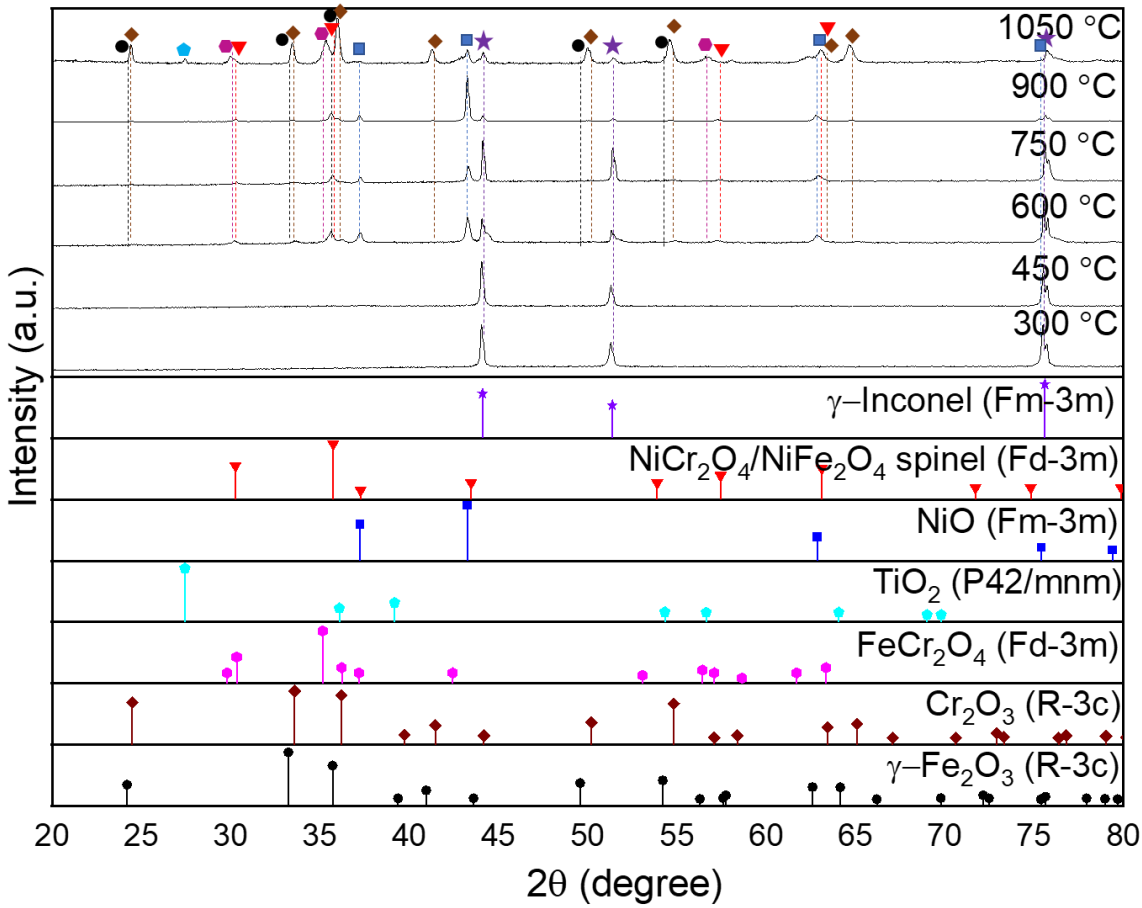

Figure 3.10. Oxide compounds identification of pre-oxidized Inconel 600 annealed at 300 – 1050 °C.

OM examination of the surface of Inconel 600 specimen annealed at 300 °C shows pink, dark brown, and black colors. These colors indicate the formation of the thin oxide film of Fe, Cr, and Ni. However, surface SEM/EDS and XRD analysis cannot provide enough information to confirm the preliminary identification of OM examination.

Better oxide film identification can be observed from the specimen annealed at 450 °C. SEM/EDS characterization of the specimen surface clearly shows the elemental overlapping, especially indicating the correlation between Ni and O. This formation is then identified as NiO with the appearance of new peaks in the XRD pattern. OM observations show a more colorful surface dominated by dark brown to green indicating the presence of nickel, iron, and chromium oxides.

Clear observation using all characterization techniques can be performed for specimen annealed at 600 °C. XRD analysis indicates the existence of NiO, Fe_2O_3, Cr_2O_3, and the spinel of $FeCr_2O_3$, $NiCr_2O_3$, & $NiFe_2O_4$. Although some XRD peaks of these compounds, especially $NiCr_2O_3$, and $NiFe_2O_4$ which are isomorphic, are overlapped and difficult to be distinguished, however, SEM/EDS observation indicates they may exist in small amounts as had been identified such as by (Moosa, Ahmed and Hoobi, 2007; Xiao *et al.*, 2013; Wu *et al.*, 2018). Cross-sectional SEM/EDS observation shows elemental overlapping, especially between Fe–O and Ni–O as the outer layer. Meanwhile, Cr–O, which overlaps with Mn, is formed mainly as the inner layer.

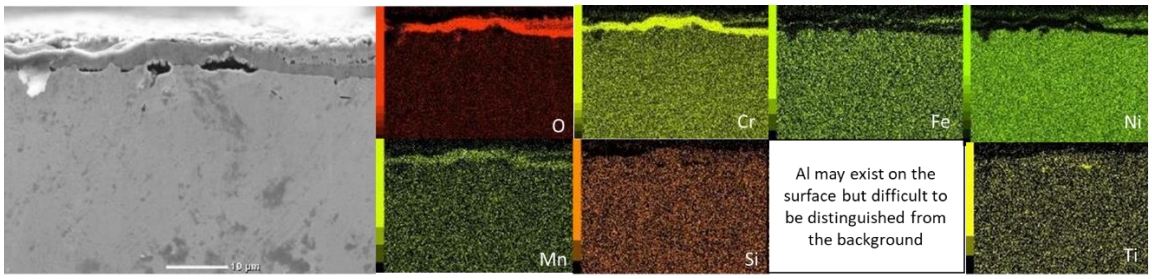

Figure 3.11. Cross-sectional oxide film morphology of pre-oxidized Inconel 600 specimen annealed at 900 °C.

Inconel 600 annealed at 750 °C has rougher and thicker oxide film compared with the specimen annealed at 600 °C. XRD analysis confirms the formation of NiO, Fe_2O_3, and the spinel of $NiCr_2O_3$, & $NiFe_2O_4$ which may exist as the outer oxide layer.

Chromium oxides in the form of Cr_2O_3, $FeCr_2O_3$ spinel, and a part which is related to Mn and Ti dominate the inner layer. Formation of Ti can be observed mainly spread around the cracks but unable to be characterized by XRD.

The relatively ideal observation using all characterization techniques can be performed from the specimen annealed at 900 °C. The surface formation of the specimen became coarse and dominated by Fe–O and Ni–O with several bubble-like cracks. These bubble-like cracks contain Ti and are identified as titanium oxides. These bubble-like cracks also can be observed from cross-sectional SEM/EDS analysis as shown in Figure 3.11. These cracks can be formed due to the carbon-oxygen reaction forming a gas bubble of CO_2/CO (Rao, 1988); or because of the different stress forces between the base and oxide layers during the annealing. Cross-sectional SEM/EDS observation clearly shows the inner oxide layer especially constructed by Cr–O and Mn spinel. While the outer oxide layer is mainly dominated by Ni, Fe, Cr, and some minor elements. Chemical compounds of the outer oxide layer furthermore are identified by XRD analysis, which is closely related to NiO, Cr_2O_3, Fe_2O_3, and spinel of $NiFe_2O_4$, $NiCr_2O_3$, & $FeCr_2O_3$.

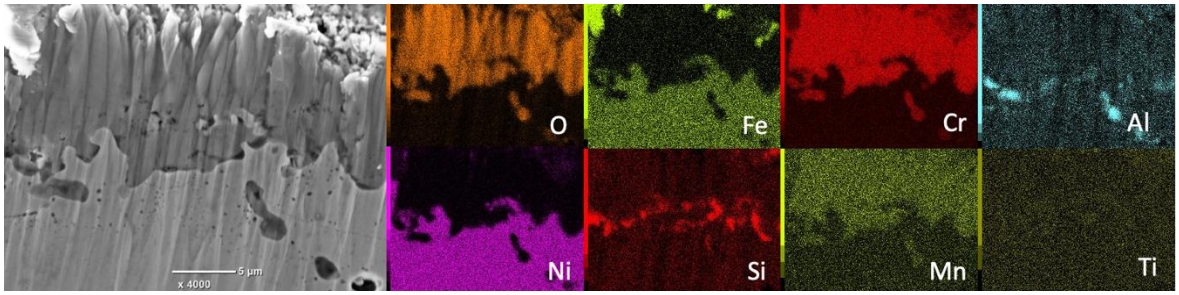

Figure 3.12. Cross-sectional morphology of pre-oxidized Inconel 600 specimen annealed at 1050 °C.

The same formation of oxides with specimen annealed at 900 °C can be observed from specimen annealed at 1050 °C. However, as shown in Figure 3.12, the oxide film of this specimen is around 2-5 times thicker compared with the specimen annealed at 900 °C. SEM/EDS mapping shows the oxide layer is dominated by chromium oxides with its Mn spinel, which acts as a protective inner layer. While the thin outer oxide layer consists of Fe, Mn, Ni, Si, and Al. Besides the outer layer, aluminum oxides are also observed to fill the cracks just below chromium oxides. Rich formation of Si especially can be found located between the base material and inner layer. While some of them lay in the

outermost oxide layer. XRD analysis furthermore indicated the existence of Cr_2O_3 as the inner layer, including NiO, Fe_2O_3, and minor formation of TiO_2 as the outer layer. Besides that, $NiFe_2O_4$, $NiCr_2O_3$, and $FeCr_2O_3$ spinels may also exist with a very limited amount.

3.2.4 Pre-oxidized Film of X-750

In general, X-750 has the best high temperature oxidation resistance properties compared to SS 304, SS 321, and Inconel 600. OM examination of the X-750 specimen annealed at 300 °C only shows the color change in some parts, especially on the cracks and grain boundaries.

Color changing to be brown, green, purple, and dark, can be seen clearly from the specimen annealed at 450 °C. These colors should be related to the oxide compounds of Ni, Cr, and Fe. SEM/EDS observation of the specimen surface observes several dots indicating the formation of nickel oxides. However, as shown in Figure 3.13, the XRD analysis of this specimen produces the same peaks compared with the unoxidized and 300 °C annealing specimens.

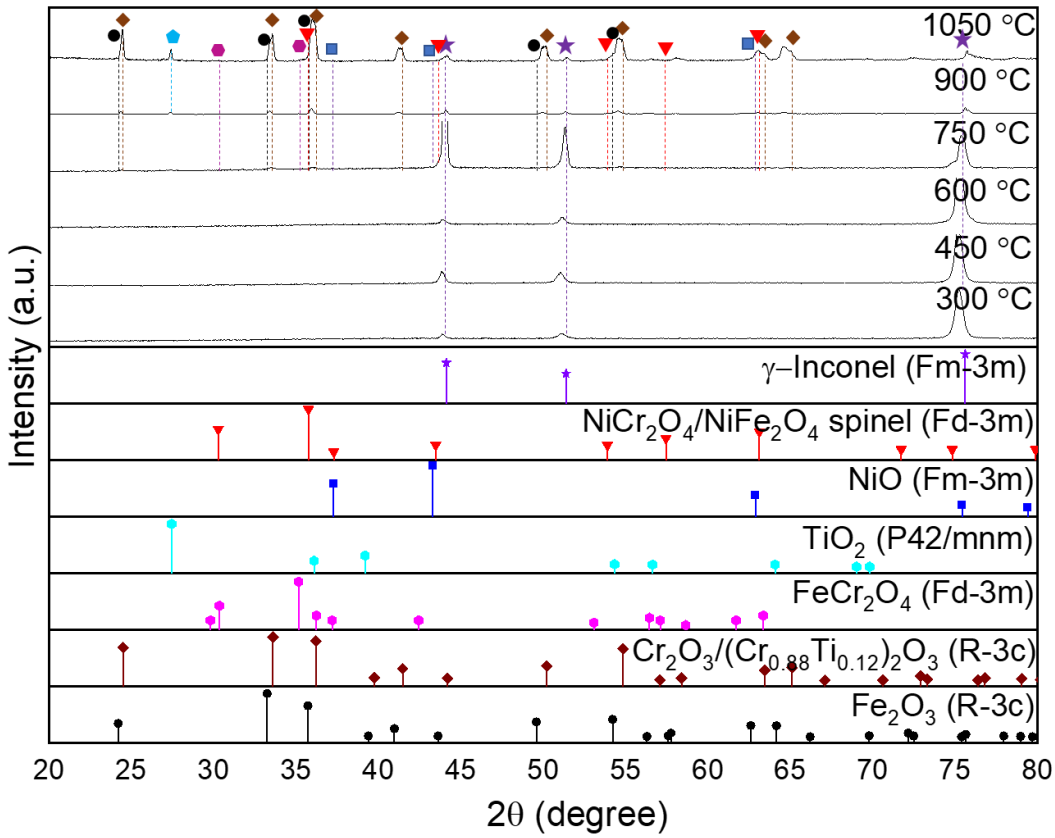

Figure 3.13. Oxide compounds identification of pre-oxidized X-750 annealed at 300 – 1050 °C.

Similar oxide films but with different compositions and thickness are expected from the specimen annealed at 600 °C. Specimen annealed at 600 °C is dominated by green with several red-brown areas and dark around the cracks. These colors show the formation of nickel oxides, chromium oxides, and iron oxides. SEM/EDS observation of the specimen surface identifies the formation of nickel oxides. However, like the specimen annealed at 450 °C, the XRD analysis of this specimen is unable to identify any oxide compound-related peaks.

Detail examination can be performed starting from the specimen annealed at 750 °C. OM examination shows black, green, and red colors. These colors indicate the formation of nickel oxides, iron oxides, and chromium oxides. SEM/EDS observation of the specimen surface shows the growth of Ti–O rich formation around the cracks between the nickel oxides and iron oxides-rich areas. Several oxide formations of minor elements such as Al, Si, and Mn also exist. The oxide of Al must be related to Al_2O_3 as confirmed in the study of (Tan, Chen and Pint, 2019). Despite the intensity being relatively low, the newly appeared XRD peaks exist. These XRD peaks are associated with the formation of NiO, Fe_2O_3, TiO_2, Cr_2O_3, and/or $(Cr_{0.88}Ti_{0.12})_2O_3$ which is isomorphic, and the rest should be spinel of $FeCr_2O_4$, $NiCr_2O_4$ and/or $CrFe_2O_4$.

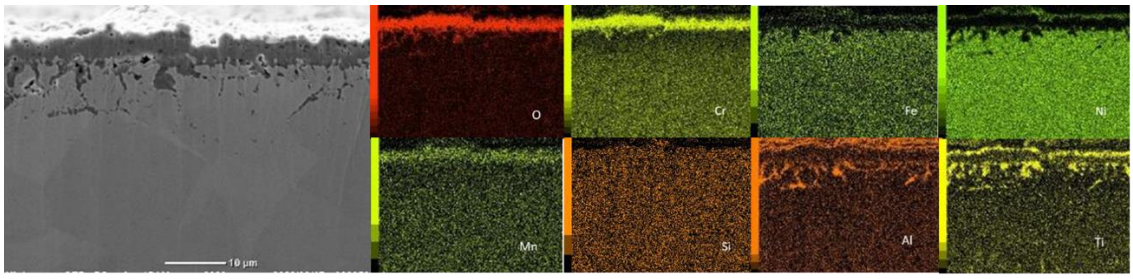

Figure 3.14. Cross-sectional oxide film morphology of pre-oxidized X-750 specimen annealed at 900 °C.

Robust oxide film formation of X-750 can be clarified from specimens annealed at 900 °C and 1050 °C as shown in Figure 3.14 and Figure 3.15. Both specimens show an inner oxide layer constructed by a Cr-rich formation, which is also associated with Mn and Ti. Several cracks are formed between the base material and the inner oxide layer which are filled with aluminum oxides and titanium oxides. A thin outer oxide layer is constructed by various types of oxides, including Fe, Ni, Cr, Mn, Al, Ti, and a very limited

amount of Si. Needle-like formations of Ti can be seen from SEM/EDS observation of the specimen surface. XRD analysis from both specimens annealed at 900 °C and 1050 °C as shown in Figure 3.13 indicated the same formation of NiO, Fe_2O_3, TiO_2 and Cr_2O_3, and/or $(Cr_{0.88}Ti_{0.12})_2O_3$. The other small peaks which are related to other oxides may exist, especially spinel of $FeCr_2O_3$, $NiCr_2O_3$, and $NiFe_2O_4$. This result is relatively similar to the study of (Tuzi *et al.*, 2016, 2017; Yun, Park and Wang, 2017) although performed under different environmental conditions.

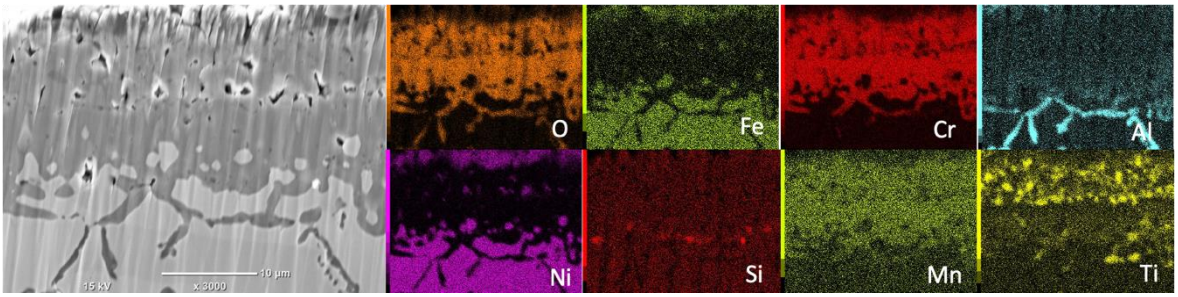

Figure 3.15. Cross-sectional oxide film morphology of pre-oxidized X-750 specimens treated at 1050 °C.

3.3 Discussion

The oxidation resistance of metals can be improved, mainly by limiting oxygen diffusion to the material and reducing material elements' migration to the surface (Sequeira, 2019, pp. 199–201). Adding chromium as the solute element is one of the typical methods to improve the oxidation properties of steel and nickel materials (Ezugwu, 2004; Pedeferri, 2018). The chromium oxides layer can reduce oxygen diffusion and suppress oxidation mechanisms. It is possible because chromium oxides have small oxygen partial pressure gradients and diffusion coefficients (Noguchi and Yakuwa, 2016). Other solute elements also can be added for the matrix alloy and chromium oxides formation improvements. These elements such as Al and Ti. Al and Ti improve material properties through crystal structure changing as well as their characteristics which are easily diffused and oxidized (Callister and Rethwisch, 2013; Hoffelner, 2013; Lahiri, 2017). Al and Ti increase swelling resistance and creep properties of Ni-based alloys by forming γ'. Al and Ti also increase the oxidation resistance of SS and Ni-based alloys because it is relatively easy to migrate and oxidize on the surface and/or cracks areas, then largely reduce oxygen

partial pressure gradient. Ti can improve alloy's oxidation properties at elevated temperatures by reducing carbon precipitation into the chromium oxides layer, forming a fine scale of carbides, and intermetallic phases (Tipping, 2010, p. 115).

3.3.1 Thermodynamic Properties and Oxidation Growth

The n-type and p-type semiconductor theories can be used to explain how oxygen from the atmosphere penetrates the specimen (Pedeferri, 2018, pp. 596–597). These mechanisms can be imagined by considering the existence of oxygen and metal lattice defects making oxygen may move to the material's matrix, and on the other side, metal ions migrate to the oxide matrix. As explained by (Noguchi and Yakuwa, 2016), the combination of this theory with oxygen partial pressure, oxygen diffusion based on Fick's first law, Wagner's theory regarding parabolic rate law and Arrhenius equation, the oxidation rate constant (k_p) furthermore can be written as:

$$k_p \approx D_0 \Delta P_{O_2} exp\left(\frac{-Q}{RT}\right)$$

Where:

D_0 is self-diffusion coefficient of oxygen,

P_{O_2} is oxygen partial pressure,

Q is the activation energy,

R is gas constant, and

T is the absolute temperature.

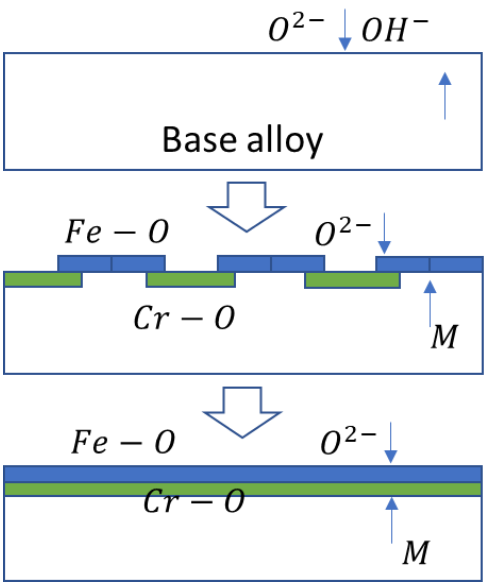

Figure 3.16. Oxide film growth mechanism model.

This equation indicates the oxide film growth is proportional with oxygen partial pressure and has parabolic relation with temperature. The parabolic relation of temperature is caused by oxygen partial pressure reduction through the formation of the oxide film. Based on these theories, the oxidation growth mechanism can be observed from specimens that are annealed at various temperatures as performed in this study.

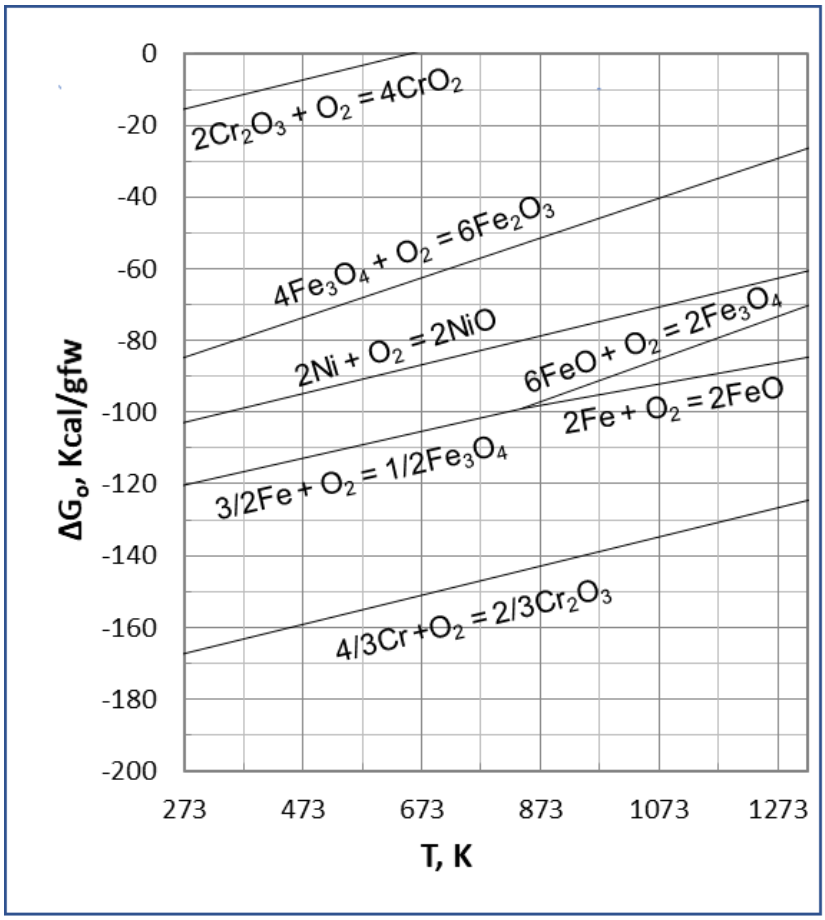

Figure 3.17. Ellingham diagram showing the relationship of Gibbs free energy with the temperature of some oxidation reactions[1]

As illustrated in Figure 3.16, oxidation begins when oxygen is available. Oxygen and metal ions become conductive in the presence of lattice defects then followed by the release and capture of electrons. Electron transfer between oxygen and metal furthermore generates negative oxygen and positive metal ions on each opposite side. That condition then forces the oxygen and metal ions migration and reaction to form such kinds of oxide compounds. However, each oxide compound has different oxygen partial pressure on its

[1] (Generated from: http://showard.sdsmt.edu/)

interface as well as thermodynamic properties with oxygen. These differences furthermore contribute to the oxygen diffusion rate into the specimen and the migration of metal ions to the outside. As can be seen from the Ellingham diagram shown in Figure 3.17, Gibbs free energy of Cr is small compared with Fe and Ni. That condition makes Cr is relatively easier to oxidize to be Cr_2O_3. However, Cr_2O_3 is more stable compared with Fe and Ni. Oxide compounds of Fe and Ni have high dissociation pressure (Stratton, 2013) which furthermore contributes to the oxide formation arrangement. Cr with lower dissociation pressure tends to form as the inner oxide layer while the others formed as the outer oxide layer.

Base element differences between SS 304 & SS 321, and Inconel 600 & X-750 greatly affect the oxidation behavior between them. As the Fe-based materials, oxide formation of SS 304 and SS 321 grow faster compared with Ni-based alloys, Inconel 600 and X-750. As shown in Figure 3.17, Ni is thermodynamically more stable compared with Fe making it become the better choice to be utilized for high temperature environments. However, Ni is expensive which makes it must be selected selectively.

3.3.2 Matrix Composition and the Oxidation Growth

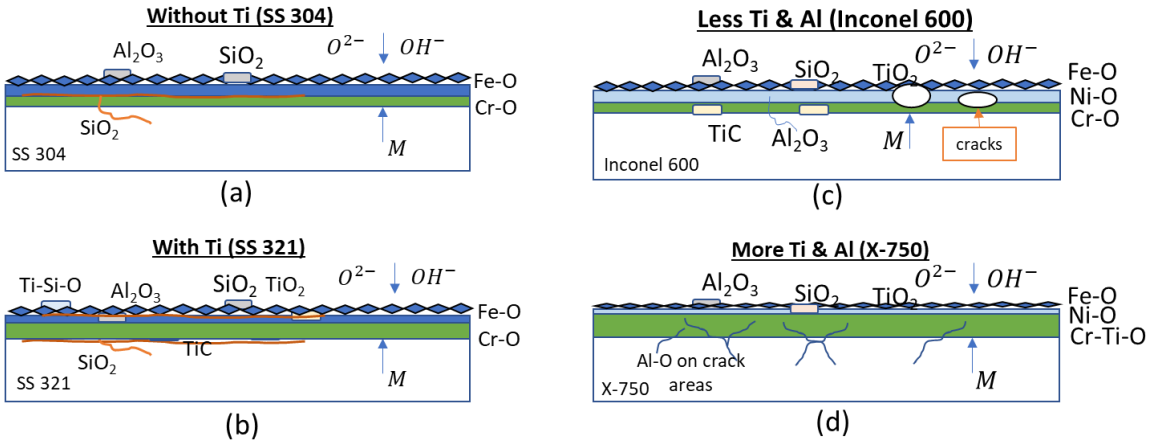

Figure 3.18 Pre-oxide film differences between (a) SS 304, (b) SS 321, (c) Inconel 600 and (d) X-750.

Generally, the oxide film of both SS and Ni-based alloys is similar, consisting of inner and outer layers. The inner layer is constructed mainly of chromium oxides, while the outer layer consists of the oxides of several elements. This similarity is also observed in other studies such as those by (Tuzi *et al.*, 2017; Z. yang Li *et al.*, 2019). However, base,

and solute elements differences between those alloys change the oxidation resistance behavior between them. These differences furthermore could be illustrated in Figure 3.18.

3.4.2.1 Effect of Minor Elements on Stainless Steel

SS 304 is less resistant to high temperature oxidation compared with SS 321. Less oxidation resistance of SS 304 is caused by less stable chromium oxide formation. The chromium oxides layer strongly suppresses the elements' migration and oxygen diffusion. However, that mechanism does not stop the process completely. Oxygen diffusion and element migration still occur and can be accelerated by several factors. Temperature accelerates the oxidation process exponentially (M. Schutze, 2008). The existence of OH^- speeds up the oxidation by interacting with Fe_2O_3, and/or Cr_2O_3, to form $Fe(OH)_2$, and/or $Cr(OH)_2$. These hydroxides are unstable at high temperatures and decompose to be Fe_2O_3, Cr_2O_3, or such kinds of iron-chromium oxides after releasing gaseous H_2O (Chang *et al.*, 1992; Marchetti *et al.*, 2016). Migration of Cr from the inner layer to the outer and/or the environment may reduce the chromium oxide integrity, except if the same amount of Cr still can be supplied from the matrix. If chromium oxide integrity cannot be maintained, then uncontrolled oxidation by fast oxygen diffusion and element migration occurs. The existence of minor elements such as Ti, Al, Mn, and Si plays an important role in oxidation integrity. These elements have relatively low Gibbs free energy, making them easier to be migrated and oxidized. Small amounts of Al are usually present in both SS 304 and SS 321 as an impurity. Solute Al tends to migrate to the surface and form thin aluminum oxide formations which can reduce oxygen diffusion. Besides forming manganese oxides on the outer layer, Mn may also compound with Cr, and with the appropriate amount may increase the oxidation resistance (Xu *et al.*, 2012). Si tends to migrate to the cracks between the base material and inner oxide layer to form SiO_2. SiO_2 also contributes to the oxidation suppression mechanism.

The high-temperature oxidation resistance of SS 321 increases because of Ti. Ti reacts with dissolved C to form TiC (Tipping, 2010; Yvon, 2017) which can be observed in this study. Solute C is present in SS as an impurity during the fabrication, and its concentration can be reduced through decarburization (Lahiri, 2017, p. 48). The presence of C reduces the protective oxide layer integrity by reacting with chromium to form chromium carbide. To avoid chromium oxides integrity reduction, titanium is added

around 5 times of C concentration to produce SS 321 (Pedeferri, 2018, p. 301). The existence of Ti furthermore can stabilize chromium oxides. It is possible because the potential energy of the C and Ti reaction to form TiC is smaller compared with Cr to form chromium carbides. Besides increasing the oxidation resistance, Ti changes the surface of the oxide film by forming a thin layer of TiO_2. Oxidation improvement due to solute Ti furthermore affects the SiO_2 distribution in the oxide film of SS. The better oxidation resistance of SS 321 contributes to the amount of Si which becomes smaller compared to the SS 304.

3.4.2.1 Effect Minor Elements on Ni-based alloys

Oxidation of Ni-based alloys is similar to SS. Metal ions migrate to the surface and oxygen diffuses to the metal matrix and then reacts with each other to form such kinds of oxides. Due to the thermodynamic property differences of each metal and its oxide, the formation arrangement between oxides takes place. Cr_2O_3 with some of its spinel tends to be the inner oxide layer, while the other compounds such as NiO, Fe_2O_3, and $NiFe_2O_4$ construct the outer oxide layer. The existence of Ti in Ni-based alloys improves its oxidation resistance. Ti stabilizes the chromium oxide layer as happened in SS 321 by reacting with C to form TiC. However, as observed from Inconel 600, TiC may undergo further reactions with oxygen then produce titanium oxides and release CO or CO_2 gasses that furthermore look like crack/explosive fractures, which have also been observed by (Rao, 1988). Nevertheless, those explosion-like cracks may occur in other ways, such as caused by the different stress between the main material and the oxide formation. However, unlike SS, Inconel 600 protective layer is still maintained up to 1050 ^{o}C, except for some locations due to the explosion-like cracks phenomenon.

When a larger amount of Ti and Al is introduced into Ni-based alloys as happened in X-750, these solute elements largely improve the oxidation resistance by following some ways. Ti and Al improve high temperature oxidation and corrosion strength of Ni-based alloys by forming γ'. Both Ti and Al have relatively low Gibbs free energy, which makes them easier to oxidize and form such a thin oxide layer on the surface and fill the cracks. That mechanism largely suppresses oxygen diffusion to the matrix alloys. Ti may also react with Cr and O to form chromium titanate and together

with Cr_2O_3 construct an inner oxide layer that has a good ability to reduce oxygen potential.

3.4 Summary

The early oxidation mechanism of all specimens must be the same, except related to oxides concentration due to the base and solute elements concentrations. Iron oxides dominate the surface of SS, while nickel oxides cover the Ni-based alloys. Elements with faster diffusivity and higher dissociation pressure such as Fe, Ni, Al, and Ti are arranged as the outer oxide layer. Meanwhile, Cr is mainly located in the inner oxide layer. The different types and concentrations of solute elements furthermore change the oxidation mechanism. Solute Ti improves oxidation resistance by following some ways, by covering the surface and/or grain boundaries with TiO_2 then reducing the oxygen diffusion to the alloy's matrix, stabilizing the chromium oxide layer by absorbing C that might exist as the impurity, forming γ' and reacting with Cr forming such kind of chromium titanate. Solute Al and Si increase the oxidation resistance by reducing oxygen diffusion, both by forming an oxide layer on the surface as well as on the grain boundaries.

Different oxidation growth characteristics lead to the surface structure variation of each material. A thin oxide layer composed of various elements and concentrations happens in the early oxidation stage. Iron oxides and nickel oxides dominate the surface of SS and Ni-based alloys, respectively. While the inner oxide layer of both materials is constructed by chromium oxides and several spinels.

3.5 References

Callister, W. D. and Rethwisch, D. G. (2013) Materials Science and Engineering 9th Edition. 9th Edition, Wiley. 9th Edition. Wiley. doi: 10.1016/j.str.2011.03.005.

Chang, S. J. et al. (1992) 'Corrosion of Austenitic Stainless Steel in Steam Containing Cesium Hydroxide', Journal of Nuclear Science and Technology, 29(8), pp. 753–761. doi: 10.3327/jnst.29.753.

Chapman, J. and Hess, S. M. (2018) 'Risk-Informed, Technology-Neutral Design and Licensing Framework for New Nuclear Plants', in Risk-informed, Technology-

neutral Design and Licensing Framework for New Nuclear Plants. Brussels, Belgium, pp. 1–10.

Clément, B. et al. (2003) 'LWR severe accident simulation: Synthesis of the results and interpretation of the first Phebus FP experiment FPT0', Nuclear Engineering and Design, 226(1 SPEC. ISS.), pp. 5–82. doi: 10.1016/S0029-5493(03)00157-2.

Eastaugh, N. et al. (2013) Pigment Compendium. A Dictionary and Optical Microscopy of Historical Pigments, Journal of Chemical Information and Modeling.

Ezugwu, E. O. (2004) 'High Speed Machining of Aero-Engine Alloys', Journal of the Brazilian Society of Mechanical Sciences and Engineering, 26(1), pp. 1–11. doi: 10.1590/S1678-58782004000100001.

Fisher, K. B. et al. (2018) 'The role of surface deformation in the oxidation response of type 304 SS in high temperature deaerated water', Corrosion Science, 141(December 2017), pp. 88–96. doi: 10.1016/j.corsci.2018.06.033.

Fox, M. A. (2007) Colour Chemistry, Glossary for the Worldwide Transportation of Dangerous Goods and Hazardous Materials. Cambridge: Royal Society of Chemistry (RSC Paperbacks). doi: 10.1039/9781847550590.

Guentay, S. et al. (2005) 'Iodine behaviour during a severe accident in a nuclear power plant', Chimia, 59(12), pp. 957–965. doi: 10.2533/000942905777675453.

Hoffelner, W. (2013) Materials for Nuclear Plants, Materials for Nuclear Plants. London: Springer London. doi: 10.1007/978-1-4471-2915-8.

JEOL (2012) 'Scanning Electron Microscope A to Z. Basic knowledge for using the SEM'.

Klein-Heßling, W. et al. (2014) 'Conclusions on severe accident research priorities', Annals of Nuclear Energy, 74(C), pp. 4–11. doi: 10.1016/j.anucene.2014.07.015.

Lahiri, A. K. (2017) Applied Metallurgy and Corrosion Control, Applied Metallurgy and Corrosion Control. doi: 10.1007/978-981-10-4684-1.

Li, Z. yang et al. (2019) 'Characteristics and formation mechanism of oxide film on 304 stainless steel in high temperature water', Materials Chemistry and Physics, 222(October 2018), pp. 267–274. doi: 10.1016/j.matchemphys.2018.10.029.

M. Schutze, W. J. Q. (2008) Novel approaches to improving high temperature corrosion resistance. Washington, DC: Woodhead Publishing Limited.

Marchetti, L. et al. (2016) 'Corrosion of nickel-base alloys in primary medium of pressurized water reactors: New insights on the oxide growth mechanisms and kinetic modelling', Corrosion Science, 102, pp. 24–35. doi: 10.1016/j.corsci.2015.09.001.

Moosa, A., Ahmed, J. K. and Hoobi, A. (2007) 'Corrosion properties of Inconel alloy 600 coated by simultaneous aluminizing-chromizing process', Materials Science Forum, 546–549(PART 3), pp. 1763–1768. doi: 10.4028/0-87849-432-4.1763.

Murty, K. L. (2013) Materials ageing and degradation in light water reactors: Mechanisms and management, Materials Ageing and Degradation in Light Water Reactors: Mechanisms and Management. doi: 10.1533/9780857097453.

Noguchi, M. and Yakuwa, H. (2016) 'Lecture on Fundamental Aspects of High Temperature Corrosion and Corrosion Protection Part 1: Basic Theory'. Ebara Engineering Review, pp. 1–11. Available at: https://www.ebara.co.jp/about/technologies/abstract/detail/__icsFiles/afieldfile/2017/03/08/252_P31_1.pdf.

Orna, M. V. (2013) The Chemical History of Color, Springer. Berlin, Heidelberg: Springer Berlin Heidelberg (SpringerBriefs in Molecular Science). doi: 10.1007/978-3-642-32642-4.

Pedeferri, P. (2018) Corrosion Science and Engineering. Pedeferri,. Cham: Springer International Publishing (Engineering Materials). doi: 10.1007/978-3-319-97625-9.

Pour-Ali, S. et al. (2020) 'High temperature oxidation behaviour of AISI 321 stainless steel with an ultrafine-grained surface at 800 °C in Ar–20 vol.% O2', Corrosion Science. Elsevier, 163(May 2019), p. 108282. doi: 10.1016/j.corsci.2019.108282.

Rao, M. C. P. P. R. (1988) 'Effects of Exposure to Air at 1050 degree C on Precipitation of Carbides in Inconel 600', Cripta Metallurgica, 22(3), pp. 1213–1220.

Sehgal, B. R. (2012) Nuclear Safety in Light Water Reactors, Nuclear Safety in Light Water Reactors. Elsevier. doi: 10.1016/C2010-0-67817-5.

Sequeira, C. A. C. (2019) High Temperature Corrosion. Hoboken, NJ, USA: John Wiley & Sons, Inc. doi: 10.1002/9781119474371.

Stratton, P. (2013) 'Ellingham diagrams - their use and misuse', International Heat Treatment and Surface Engineering, 7(2), pp. 70–73. doi: 10.1179/1749514813Z.00000000053.

Tan, L., Chen, T. and Pint, B. A. (2019) 'Steam oxidation behavior of Ni-base superalloys 690, 725 and X-750 at 600 and 650 °C', Corrosion Science, pp. 487–497. doi: 10.1016/j.corsci.2019.06.014.

Tipping, P. G. (ed.) (2010) Understanding and mitigating ageing in nuclear power plants. Cornwall, UK: Woodhead Publishing. Available at: https://www.sciencedirect.com/science/book/9781845695118.

Tuzi, S. et al. (2016) 'Oxide evolution on Alloy X-750 in simulated BWR environment', Journal of Nuclear Materials, 482, pp. 19–27. doi: 10.1016/j.jnucmat.2016.09.026.

Tuzi, S. et al. (2017) 'Corrosion of pre-oxidized nickel alloy X-750 in simulated BWR environment', Journal of Nuclear Materials, 486, pp. 350–360. doi: 10.1016/j.jnucmat.2017.01.051.

Was, G. S. and Ukai, S. (2019) Austenitic stainless steels, Structural Alloys for Nuclear Energy Applications. Elsevier Inc. doi: 10.1016/B978-0-12-397046-6.00008-3.

Wu, X. et al. (2018) 'ToF-SIMS study of oxide films thermally grown on nickel-base alloys', Corrosion Science, 141(February), pp. 175–181. doi: 10.1016/j.corsci.2018.06.043.

Xiao, J. et al. (2013) 'Influence of humidity on high temperature oxidation of Inconel 600 alloy: Oxide layers and residual stress study', Applied Surface Science, 284, pp. 446–452. doi: 10.1016/j.apsusc.2013.07.117.

Xu, X. et al. (2012) 'Roles of manganese in the high-temperature oxidation resistance of alumina-forming austenitic steels at above 800 °c', Oxidation of Metals, 78(5–6), pp. 349–362. doi: 10.1007/s11085-012-9311-9.

Yun, J. Y., Park, D. and Wang, J. P. (2017) ‘A study on the oxidation behavior of nickel alloys at elevated temperatures’, IOP Conference Series: Materials Science and Engineering, 191(1). doi: 10.1088/1757-899X/191/1/012039.

Yvon, P. (2017) Structural Materials for Generation IV Nuclear Reactors, Structural Materials for Generation IV Nuclear Reactors. Elsevier. doi: 10.1016/C2014-0-03589-7.

Chapter 4

CsOH Interaction with Structural Materials

(This page intentionally left blank)

Learning how to learn is life's most important skill.

~Tony Buzan

(This page intentionally left blank)

Chapter 4

CsOH Interaction with Structural Materials

4.1 Introduction

The interaction between source terms with structural materials happens in complex ways, especially during severe accidents. The temperature of the reactor core rises rapidly when severe accidents occur due to the insufficient cooling process (Brockmann, 1987; Sehgal, 2012, pp. 93–109). The subsequent increase in temperature triggers oxidation, especially in the structural materials around the core, such as fuel, fuel cladding, fuel assembly, and control rods. In the case of light water reactors (LWRs), the oxidation reaction of fuel cladding and structural materials with water produces hydrogen gas as the by-products (Brockmann, 1987). Highly accumulated hydrogen gas could trigger an explosion. As simulated by (Fernandez-Moguel, Rydl, and Lind, 2019) for the Fukushima unit 3 accident, the explosion may happen around 27 hours after the starting point of hydrogen generation. Hydrogen explosion furthermore could destroy the reactor confinement as well as the building, followed by the release of steam containing the various types of source terms (Gupta, 2015; Nishimura, Hoshi and Hotta, 2015).

The temperature of the released steam during the explosion might be still high until reaching the boundaries between the reactor building and the environment (Brockmann, 1987; Clément *et al.*, 2003). That hot steam could trigger structural materials oxidation (Abe *et al.*, 1981; Toth *et al.*, 2007; Tóth *et al.*, 2010; Sehgal, 2012, pp. 94–97). It's just that the oxidation and chemisorption of these materials occur simultaneously. It can be assumed that the existence of pre-oxide film is negligible during the source terms release that occurred shortly after the accident. However, the effect of the pre-oxide film and its growth should be considered especially after several hours of the accident. Nevertheless, it is very difficult to determine the thickness of oxide film in each part of structural materials as a function of time.

Source terms and structural material interaction can be estimated more precisely in a longer period after the severe accident. Relatively stable formation of the oxide film can be formed after a certain period, which is affected by several environmental

conditions (Sequeira, 2019), such as temperature, humidity, air and/or water ingress, and acidity of the injected water coolant. At high temperatures, most of the source terms are released in the gaseous phase. However, the saturated gaseous phase transforms to be aerosol in cooler areas which are then deposited in the liquid phase. In addition, source terms may be dissolved by condensed steam and flow back to the core and/or to the leakage part of the environment. The interaction between source terms and structural materials around the core and leakage part to the environment are interesting topics that are categorized as important but with low knowledge availability (Firnhaber *et al.*, 1996; Watanabe, Yamada and Ohsaki, 2009; Lind *et al.*, 2020). These topics are important, especially for the long term after the accident, and consideration for decommissioning activities.

The next section of this chapter discusses the experimental results of the interaction between Cs in the form of $CsOH{\cdot}H_2O$ with various prepared pre-oxidized specimens as explained in Chapter 3.

4.2 CsOH Interaction with Major Oxides

4.2.1 Newly Formed Cs Compounds

4.2.1.1 SEM/EDS Examination

Figure 4.1 shows the atomic percentage of major elements detected on the surface of each specimen. The atomic percentage of each element is measured based on quantitative EDS at a 1200 µm x 900 µm scanning area using the ZAF method as explained by (Williams and Carter, 2009, p. 488). Although accuracy can be increased by taking a large scanning area, it must be noted that large uncertainty exists in this measurement due to the rough surface and the limitation of electron penetration. Rouge surface may induce measurement errors due to uncontrolled X-ray characteristics diffraction. Electron penetration on SEM/EDS measurements reaches only ~200-800 nm depth, while the thickness of the oxide layer including the Cs film itself is much deeper. Nevertheless, this measurement still provides some important indicators.

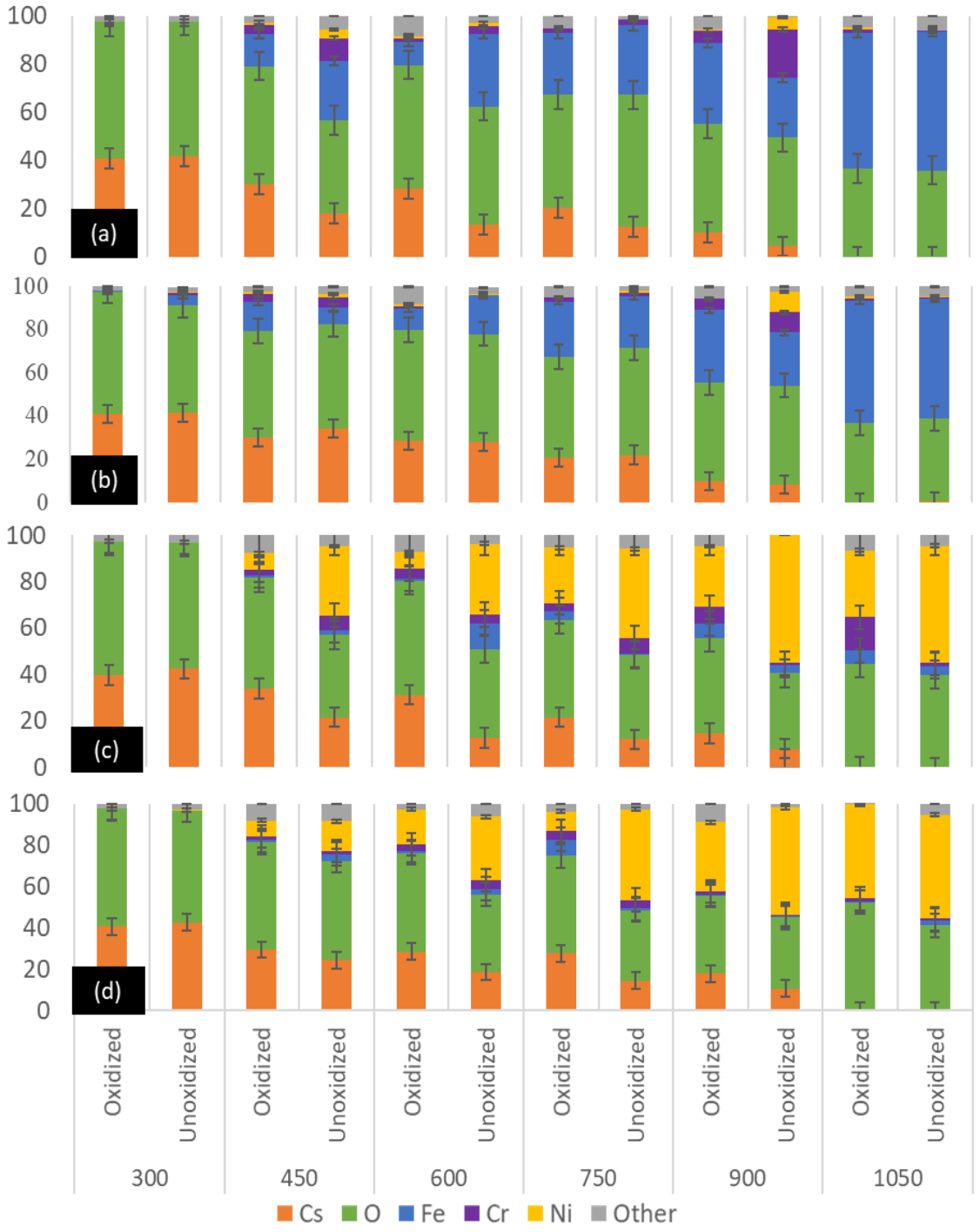

Figure 4.1. Elemental quantification of the pre-soaked (a) SS 304, (b) SS 321, (c) Inconel 600 and (d) X-750 specimens.

Although the measurement is still within the range of uncertainty, the average amount of Cs on all oxidized specimens (with pre-oxide film) is higher compared with unoxidized specimens (as received, without annealing). Cs amount differences can be

seen clearer from specimens treated at 450 °C up to 900 °C. These differences provide preliminary indications related to the importance of pre-oxide film formation to Cs retention ability.

All specimens treated at 300 °C showed similarities which are dominated by Cs and O. The measured atomic ratio between Cs and O is around 0.8, which strongly indicates the existence of CsOH precursors on the surface. Other elements such as Fe, Cr, and Ni also can be detected in a very limited amount, indicating the reaction between CsOH with the specimens had occurred. CsOH is a corrosive compound and may accelerate oxidation by producing such kinds of oxides or hydroxides as had been identified by (Chang *et al.*, 1992).

The atomic percentage of Cs is slightly reduced on specimens treated at 450 ^{o}C. That reduction is followed by the increase of the material's elements, especially dominated by Fe, Ni, and Cr. The atomic ratio of Fe, Ni, and Cr in the case of SS 304 and SS 321 is around 10:3:1. The increase of material elements also happens from Inconel 600 and X-750 but is dominated by Ni, and the rest are Cr and Fe, including the other solute elements with a total atomic ratio less than a tenth of Cs and O.

A similar trend with specimens treated at 450 ^{o}C is observed from specimens treated at 600 ^{o}C. Cs amount reduction is followed by the increase of the material's solute elements, especially Fe in the case of SS 304 and SS 321, including Ni in the case of Inconel 600 and X-750. A similar trend also happens from specimens treated at 900 ^{o}C and 1050 ^{o}C. However, at 1050 ^{o}C, Cs elements are almost completely gone due to the fast CsOH precursor evaporation rate and relatively short reaction period. Atomic percentage reduction of Cs must be related to the increase of the specimen's elements, despite evaporation of CSOH precursor as well as its newly formed compounds. The evaporation rate of Cs in the form of CsOH increases in line with the temperature, especially above 700 °C as measured by TG-DTA (detailed TG-DTA measurement of CsOH can be seen in Appendix A).

Figure 4.2 shows SEM observation of the surface of oxidized specimens of post-Cs exposure with 2000 magnification. Similar surface conditions also can be observed from unoxidized specimens.

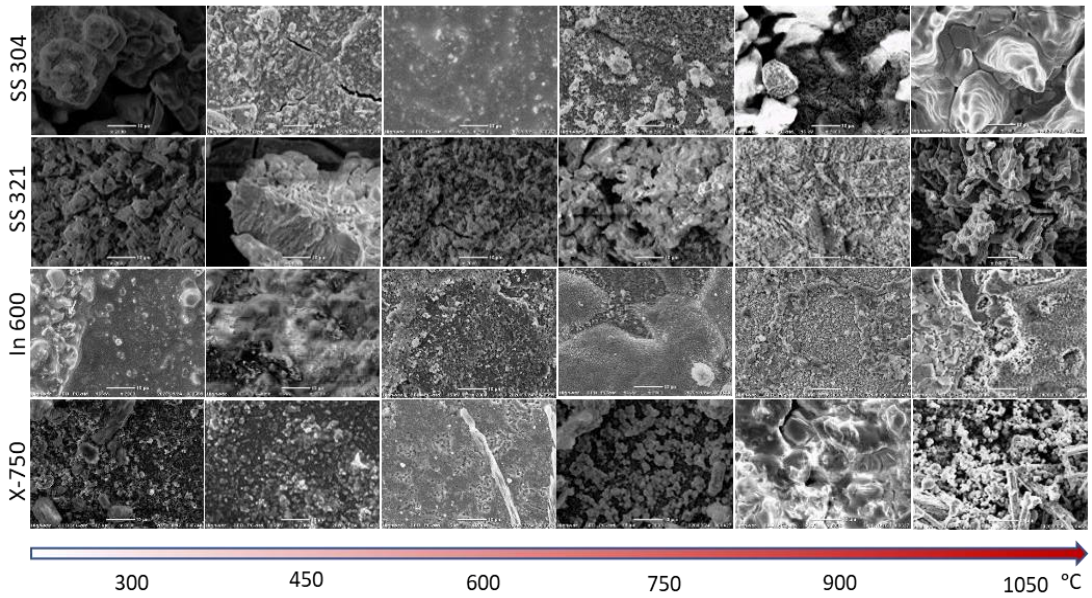

Figure 4.2. Surface morphology of the post-CsOH exposure specimens.

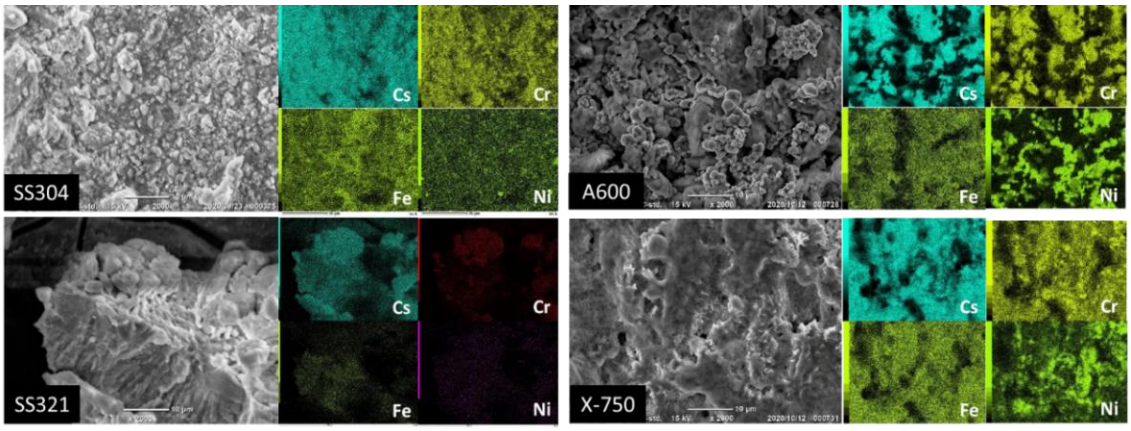

Figure 4.3. Surface SEM/EDS observation of pre-soaked specimens treated at 450 °C indicates the formation of Cs-Fe-Cr-O compounds.

Analysis related to the formation of Cs compounds is done by combining these surface SEM observations with the EDS mapping and point analysis as can be seen in Figure 4.3. SEM/EDS mapping and point analysis of specimens treated at 300 °C show the overlapping and domination of Cs and O, indicating the existence of CsOH precursor residual. Domination of Cs and O is also observed from specimens treated at 450 °C.

However, Cs mainly overlap with Fe and Cr but does not occur with Ni. This is strongly indicated that Cs makes the compounds with Fe and Cr, but relatively inert with Ni. The same indication also can be observed from both oxidized and unoxidized specimens treated at 600 °C.

The elemental overlapping pattern slightly changes starting from specimens treated at 750 °C. Specimens treated at 750 °C show the amount of Fe in the Cs-rich region become lower, while the amount of Cr is the same. This formation suggests that at 750 °C, Fe probably exists as iron oxides and cesium exists as a separate compound, but mainly is still related to the Cr. As shown in Figure 4.4, the same indication furthermore can be seen in specimens treated at 900 °C. That figure indicates Cs elements are mainly overlapping with Cr, while Fe and Ni are located on the opposite sides.

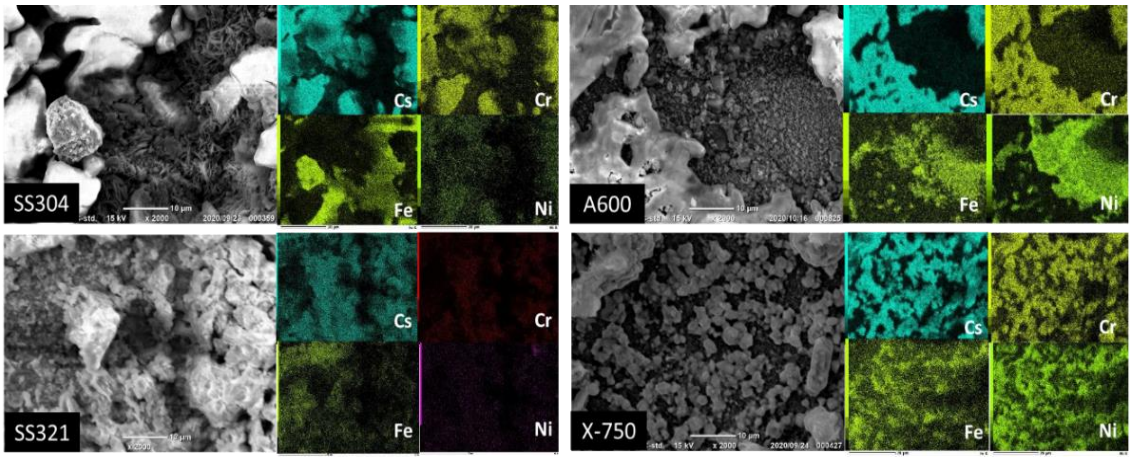

Figure 4.4. Surface SEM/EDS observation of pre-soaked specimens treated at 900 °C indicates the formation of Cs-Cr-O compounds.

4.2.1.2 XRD Analysis

As shown in Figure 4.5, the XRD analysis of all pre-soaked SS 304 and SS 321 specimens show almost similar patterns, particularly at lower temperatures. CsOH precursor-related peaks can be observed particularly from 2θ diffraction angles at 24.4°, 26.3°, 27.3°, 30.3°, and 31.5° both from SS 304, and SS 321 specimens treated at 300 °C, suggesting it remains on the surface. At 450 and 600 °C, CsOH precursor-related peaks are still presented from SS 321 specimens, however, their intensities in SS 304 are small. This shows CsOH precursor reaction with SS 304 is faster compared with SS 321. Cs_2FeO_4

and Cs_2CrO_4 related peaks which are matched with ICDD card numbers 00-025-0210 and 01-075-0866, respectively, can be observed particularly from 2θ = 23.8–24.0°, 25.2–27.0°, 27.9–28.8°, 32.0–33.2°, and 38.6–39.6°. Both Cs_2FeO_4 and Cs_2CrO_4 have crowded patterns with adjacent peaks. Although some peaks are unique, especially in 2θ = 28.5° and 32.9° for Cs_2FeO_4, and in 2θ = 26.9°, 28.7°, 33.2°, and 39.6° for Cs_2CrO_4, however, they are difficult to distinguish. Nevertheless, by combining the results of SEM/EDS analysis as shown in Figures 4.4 and 4.5, Cs_2FeO_4 and Cs_2CrO_4 must be presented in the specimens treated at 300–600 °C and 300–900 °C, respectively. Peaks related to these compounds can be observed clearly from SS 304 treated up to 900 °C. However, at this temperature, they are barely even visible from SS 321. This indicates that Cs_2FeO_4 and Cs_2CrO_4 are more abundant in SS 304 rather than in SS 321. While at 1050 °C, all peaks of both SS 304 and SS 321 specimens corresponded to Fe_2O_3, and the spinel of $NiFe_2O_4$, and/or $CrFe_2O_4$ without indication of $FeCr_2O_4$. $FeCr_2O_4$ should be totally consumed to produce Cs_2FeO_4 and/or Cs_2CrO_4. Regardless of that, observation from specimens treated at 1050 °C indicates the existence of Cs compounds is negligible.

Like the XRD analysis of SS 304 and SS 321, CsOH precursor, Cs_2FeO_4, Cs_2CrO_4, Fe_2O_3, $NiFe_2O_4$, and/or $CrFe_2O_4$ spinels are formed in pre-soaked Inconel 600 and X-750. However, as shown in Figure 4.6, peaks related to NiO in both specimens as well as chromium titanate in X-750 which has a similar pattern with Cr_2O_3 are also detected. The appearance peaks from specimens treated at 300 °C are strongly related to the CsOH precursor. CsOH precursor-related peaks still can be observed from specimens treated at 450 and 600 °C. However, the strongest peak such as at 2θ = 27.3° is slightly shifted which might be related to the changing of the crystal structure. Nevertheless, these peaks must be an indication that the CsOH precursor still exists on the Inconel 600 and X-750 specimens treated up to 600 °C. Crowded Cs_2FeO_4 and Cs_2CrO_4 related peaks which are almost impossible to be identified lonely only based on XRD analysis can be observed particularly from 2θ = 23.8–24.0°, 25.2–27.0°, 27.9–28.8°, 32.0–33.2°, and 38.6–39.6°. As also shown in Figures 4.4 and 4.5, Cs_2FeO_4 is formed from both specimens treated at 300–600 °C, while Cs_2CrO_4 is expected from specimens treated at 300–900 °C. When treated at 1050 °C, peaks of both Inconel 600 and X-750 specimens cannot show any association with Cs compounds. Peaks of Inconel 600 treated at 1050 °C

are strongly related to NiO, Fe_2O_3 and $NiFe_2O_4$, and/or $CrFe_2O_4$ spinels. While peaks of X-750 are related to Cr_2O_3 and/or $(Cr_{0.88}Ti_{0.12})_2O_3$, Fe_2O_3, including the spinel of $NiFe_2O_4$, and/or $CrFe_2O_4$ which are impossible to be distinguished. Some other small peaks also exist; however, they are very difficult to be identified.

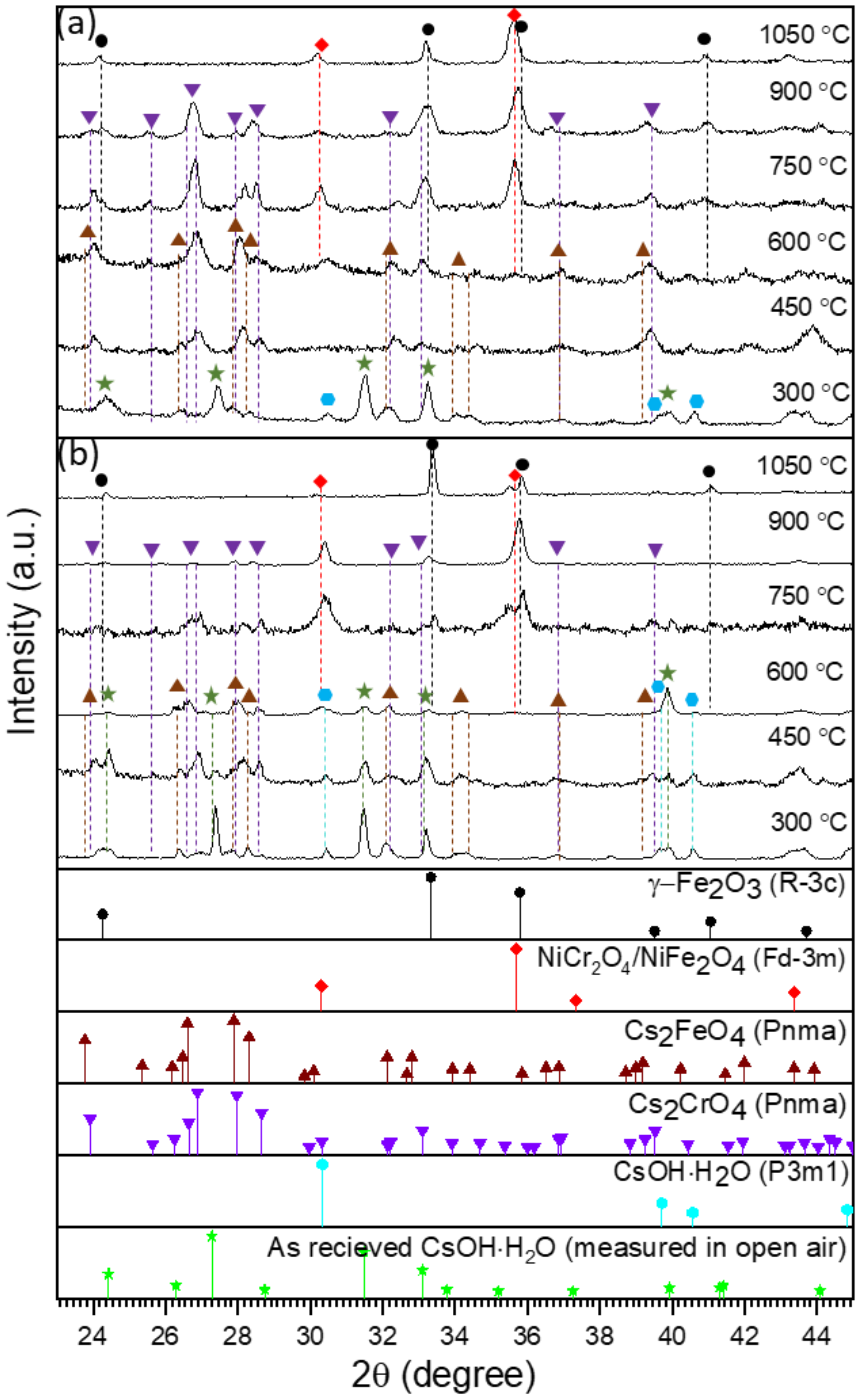

Figure 4.5. XRD analysis of pre-soaked (a) SS 304, and (b) SS 321 specimens indicate the existence of Cs_2FeO_4 and Cs_2CrO_4 compounds beside CsOH precursor and several oxides.

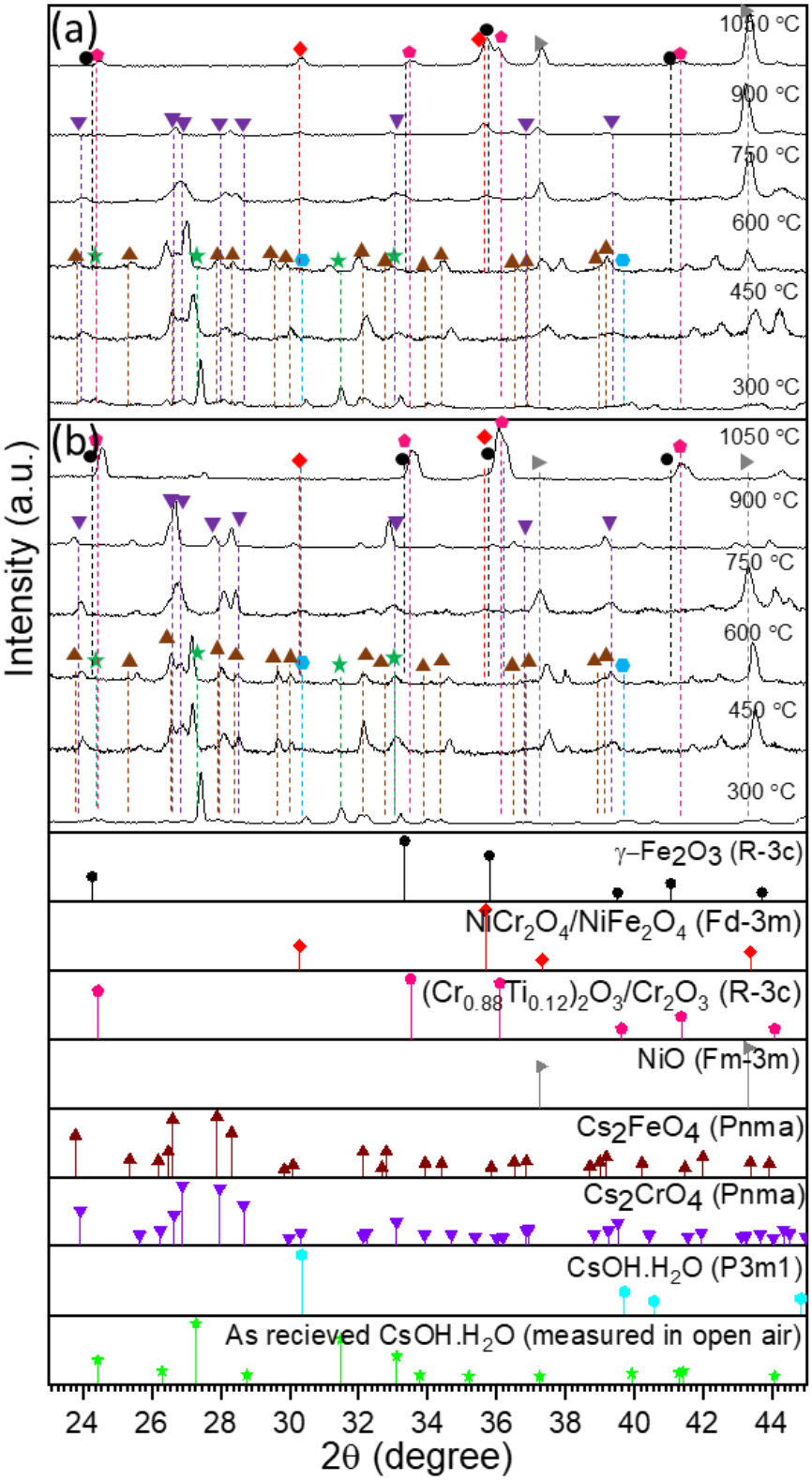

Figure 4.6. Cs_2FeO_4 and Cs_2CrO_4 compounds beside CsOH precursor and several oxides can be observed by XRD analysis from pre-soaked (a) Inconel 600, and (b) X-750 specimens.

4.2.2 Analytical Identification of Cs-Fe-Cr-O

4.2.2.1 Cs-Fe-O Compounds

Six specimens, including 1 precursor which is heated at 150 °C for 1 hour to dry up the solvent are synthesized as shown in Figure 4.7. Color differences between each specimen at different temperature treatments indicate the variation in the oxidation state of Fe.

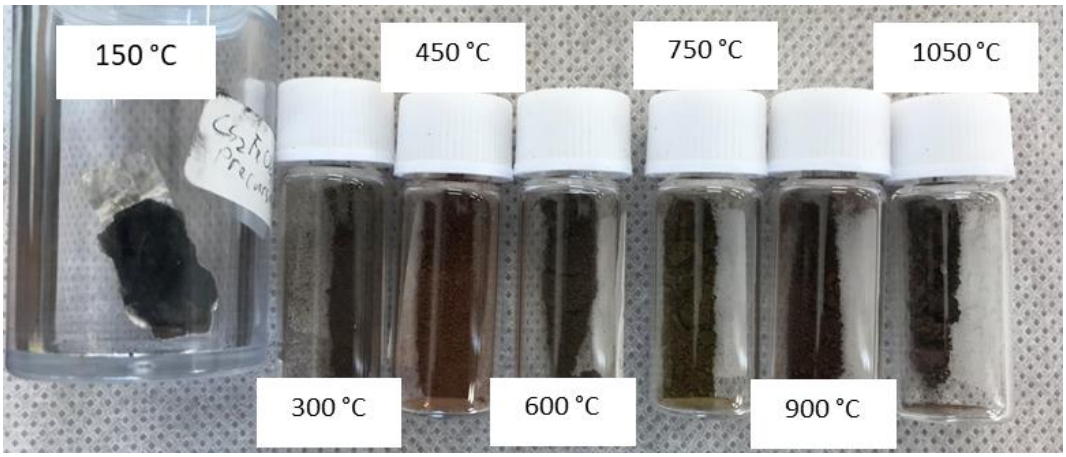

Figure 4.7. Sample preparation of Cs-Fe-O, which are treated at various temperatures.

XRD analysis as shown in Figure 4.8 indicates the formation of both Cs_2FeO_4 and $CsFeO_{2.5}$ compounds. Several peaks from the sample treated at 300 °C, especially at 2θ = 22.6°, 30.4°, 39.7°, and 40.6° are strongly related to $CsOH{\cdot}H_2O$ precursor (ICDD: 00-036-0771). The other peaks, such as at 2θ = 21.4°, 24.2°, 24.6°, 33.2°, 35.9°, 33.1°, and 39.2° are related to Fe_3O_4 and Fe_2O_3. This shows that the precursor does not fully react even after being heated for 6 hours. While the peaks other than those associated with the precursor can be identified as Cs_2FeO_4, especially at 2θ = 23.8°, 25.5°, 26.9°, 28.1°, 29.9°, 33.1°, and 34.0°. Peaks related to Cs_2FeO_4 still can be observed from specimens treated at 450 and 600 °C. However, the intensity of its peaks is getting low, indicating a lower amount of Cs_2FeO_4. Relatively clear $CsFeO_{2.5}$-related peaks can be observed from samples treated at 600 °C, especially at 2θ = 21.1°, 29.9°, and 43.1°. $CsFeO_{2.5}$-related peaks still exist up to 900 °C and are completely undetected from the specimen treated at 1050 °C. All peaks of the specimen treated at 1050 °C are associated with Fe_2O_3 which is identified as multiple phases.

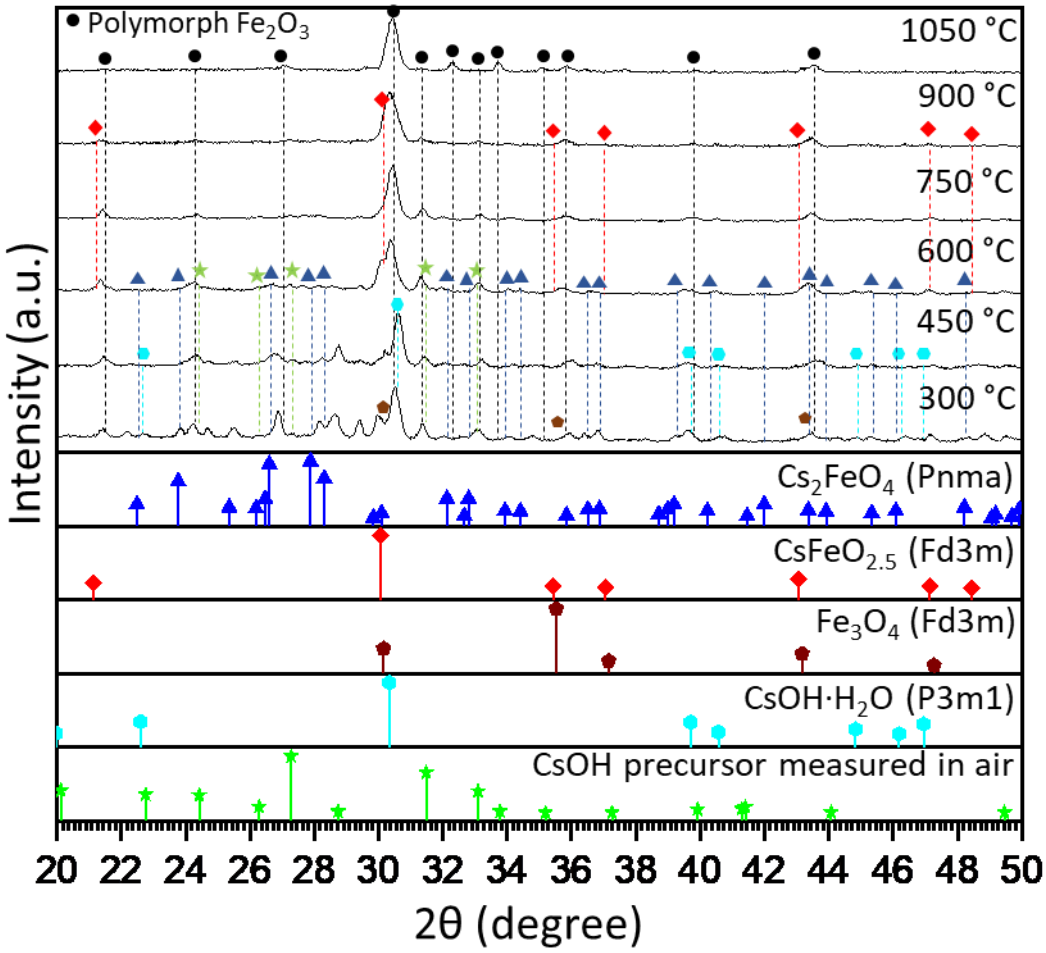

Figure 4.8. XRD analysis of synthesized Cs-Fe-O compounds treated from 300 – 1050 °C shows the reaction between CsOH precursor with Fe_3O_4 to form Cs_2FeO_4 and $CsFeO_{2.5}$ at respective temperatures.

The formation and decomposition of Cs-Fe-O compounds furthermore can be analyzed using TG-DTA as shown in Figure 4.9. Mass reduction, which happens endothermically is observed up to ~237 °C up to ~486 °C, indicating the reaction of precursor with oxygen and releasing water vapor to form Cs_2FeO_4 and the evaporation of surface water of $CsOH{\cdot}H_2O$ precursor. However, when the temperature reaches ≥ ~591 °C, the mass reduction should be related to the decomposition of Cs_2FeO_4 to be $CsFeO_{2.5}$ and Fe_2O_3. This process may be followed by the decomposition of $CsFeO_{2.5}$ to be Fe_2O_3 and such kinds of gaseous Cs compounds. That gaseous Cs compounds are related to cesium oxides (Kopelev, Popov and Val'kovskii, 1994). While starting from ~1010 °C, $CsFeO_{2.5}$ is completely decomposed to be Fe_2O_3.

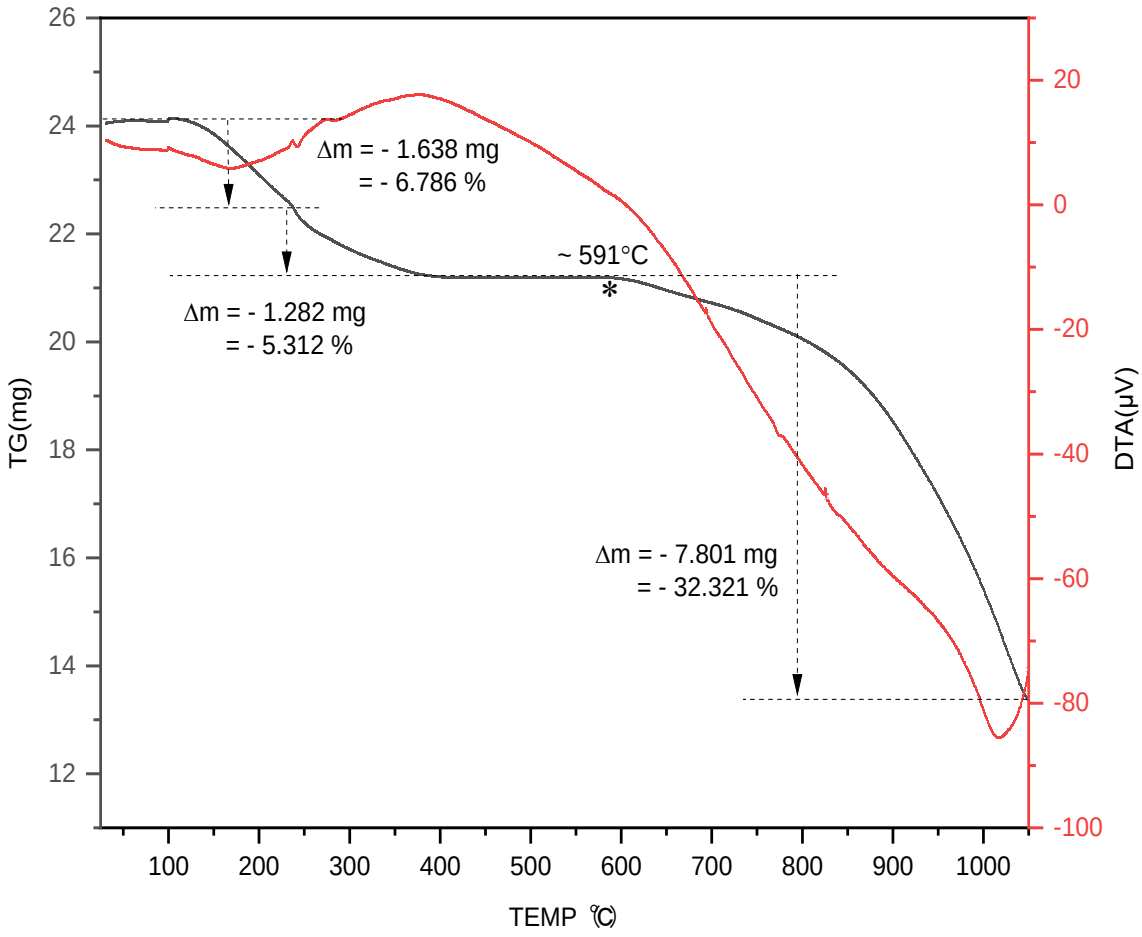

Figure 4.9. Thermal analysis showing the formation and decomposition of Cs-Fe-O compounds.

4.2.2.2 Cs-Cr-O Compounds

Cs-Cr-O is synthesized by reacting $CsOH{\cdot}H_2O$ and Cr_2O_3 with the Cs and Cr atomic ratio of 2:1 and then treated at 300, 450, 600, 750, 900, and 1050 °C. As shown in Figure 4.10, the color of specimens is changed depending on the temperature treatment. At 300 °C, the specimens look green indicating the existence of Cr(III). The color changes gradually in line with the temperature and completely becomes yellow when treated at 900 °C. The yellow color indicates the formation of Cr(VI). However, at 1050 °C, the specimen evaporates quickly which makes it unable to be collected and measured with XRD.

Figure 4.10. Prepared Cs-Cr-O compounds which are treated at various temperatures.

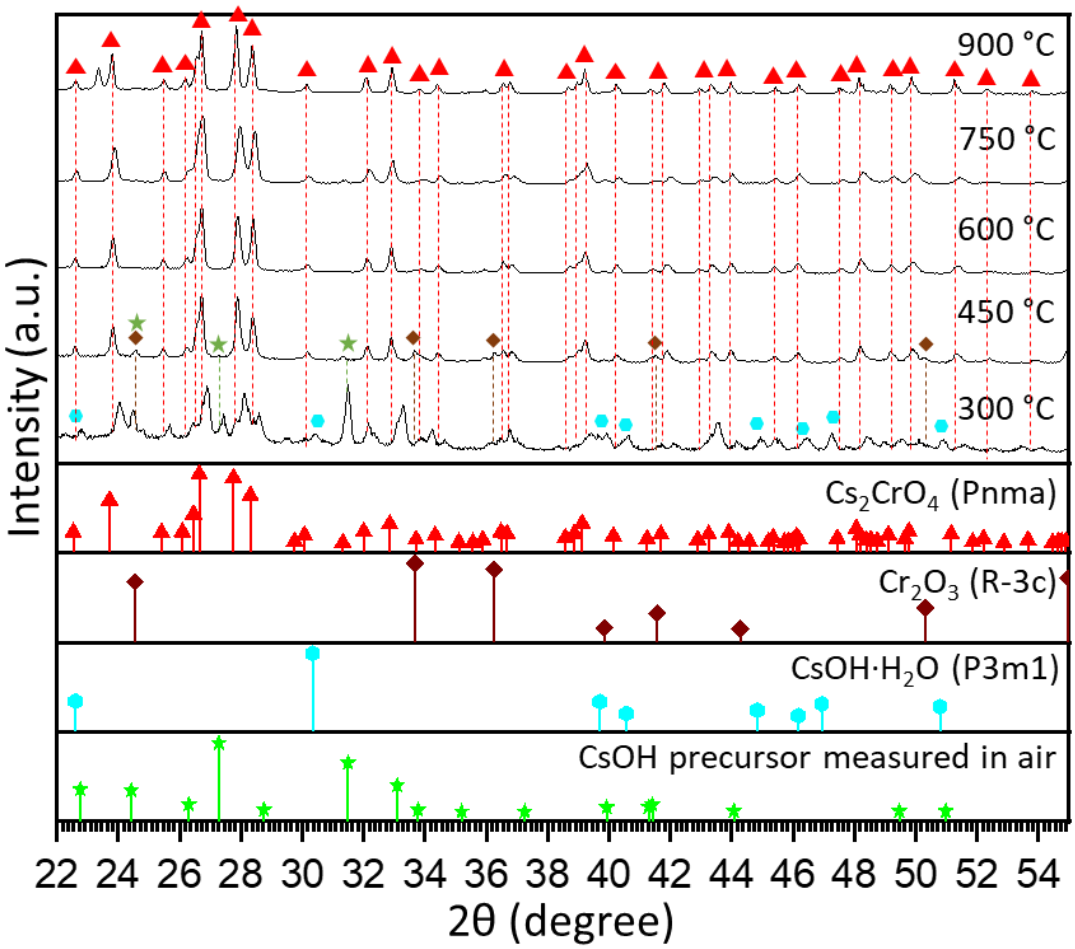

Figure 4.11. XRD analysis of synthesized Cs-Cr-O compounds indicates Cs_2CrO_4 is formed at all temperature treatments.

As shown in Figure 4.11, XRD analysis indicates that Cs_2CrO_4 is largely formed at all temperature treatments, particularly at 2θ = 22.7°, 24.0°, 26.9°, 28.1°, 28.6°, 32.2°, 33.3°, and 39.3°. However, at 300 °C, some peaks unrelated to Cs_2CrO_4 also exist. These peaks are identified as $CsOH{\cdot}H_2O$ (at 2θ = 21.6°, 24.0°, 27.4°, 30.5°, and 43.5°) and Cr_2O_3

(at 2θ = 24.7°, 33.9°, 36.5°, 41.8°, and 50.7°) precursors as well as related to the surface water due to the humidity absorption. Cr_2O_3-related peaks disappear from specimens treated at 600 °C and all peaks perfectly match with Cs_2CrO_4 with the ICDD card 01-084-2202. Peaks of specimens treated at 900 °C also match with Cs_2CrO_4, however, one new peak appears at 2θ = 23.3°. This new peak does not match with any available ICDD card. This peak may be related to the changing of the lattice crystal structure of Cs_2CrO_4.

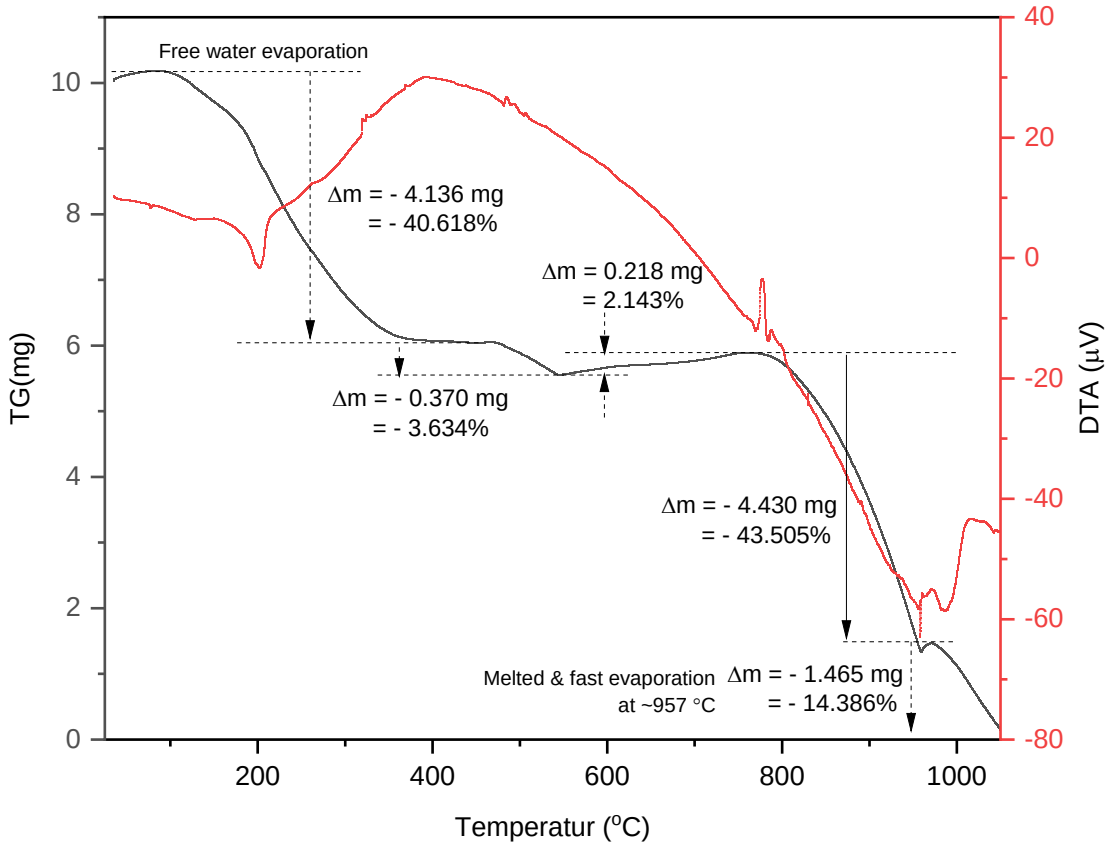

Figure 4.12. Thermal analysis indicating physicochemical changing of Cs_2CrO_4.

Detailed formation and decomposition of Cs_2CrO_4 and its correlation with temperature can be observed from TG-DTA measurement as shown in Figure 4.12. The endothermic mass reduction which can be observed up to ~200 °C relates to the free water evaporation. Large exothermic mass reduction still happens until it becomes relatively stable at ~390 °C, then followed by the mass increase which happens endothermically up to ~770 °C. This mechanism must be related to the $CsOH.H_2O$ decomposition and reaction with Cr_2O_3 precursors which release H_2O vapor as the by-product including oxygen absorption from the environment to produce Cs_2CrO_4. However, mass reduction

starting from ~800 °C is related to the decomposition and/or evaporation of Cs_2CrO_4. While at 961 °C, the graph indicates Cs_2CrO_4 is melted and then largely evaporated.

4.2.2.3 Cs-Fe-O interaction with Cr_2O_3

Figure 4.13 shows the XRD analysis of the products between Cs-Fe-O, which is mainly in the form of $CsFeO_{2.5}$ with the Cr_2O_3 reaction. The highest peaks of specimens treated at 300 and 450 °C are identified to have a strong relationship with $CsFeO_{2.5}$, particularly at 2θ = 30.3°, 35.8°, 43.4°, and 53.8°. While the rests are identified as Cr_2O_3 (2θ = 24.5°, 33.7°, 36.4°, 41.6° and 50.4°), Fe_2O_3 (2θ = 24.2°, 33.2°, 35.7°, 39.3°, 43.7° and 49.7°) and Cs_2CrO_4 (2θ = 22.7°, 24.0°, 26.9°, 28.1°, 28.6°, 32.2°, 33.3°, and 39.3°). Cs_2CrO_4-related peaks become dominant starting from specimens treated at 600 °C, while the $CsFeO_{2.5}$-related peaks seem to disappear. However, new peaks appear which are identified as Fe_2O_3. The intensity of both peaks related to Cs_2CrO_4 and Fe_2O_3 are getting higher from specimens treated at higher temperatures.

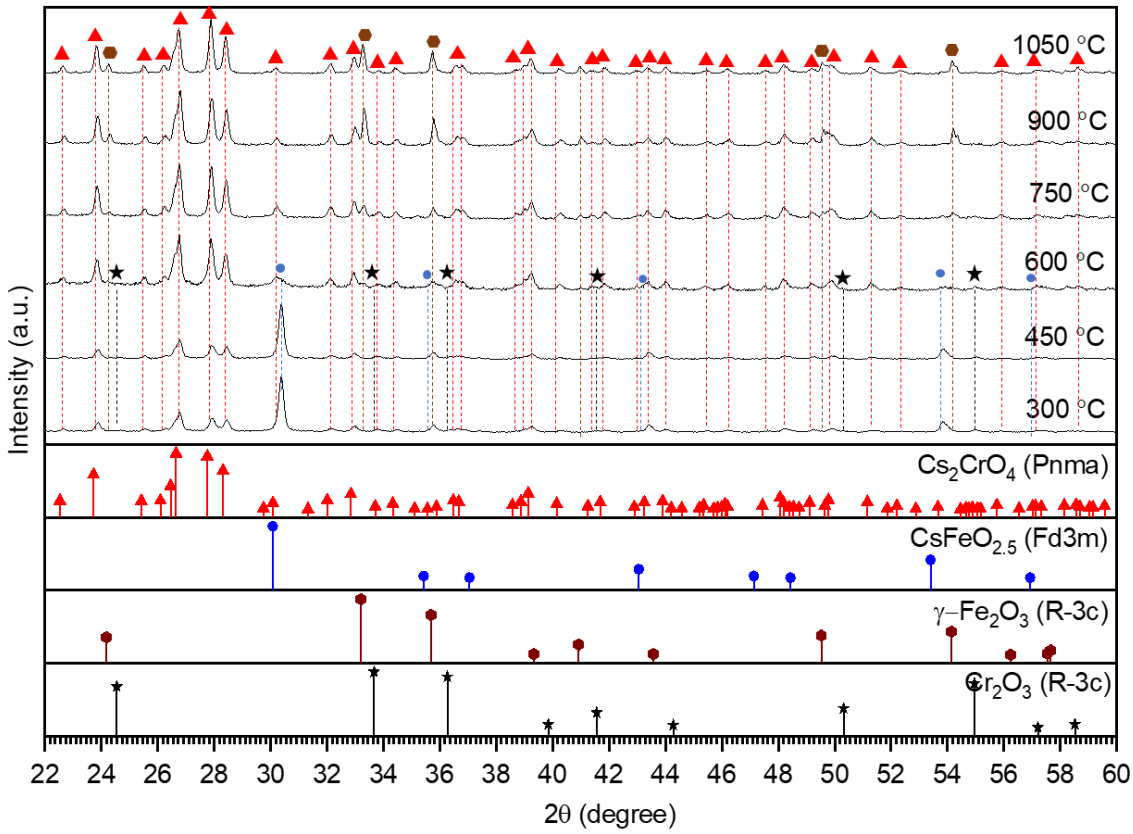

Figure 4.13. XRD analysis shows the reaction between $CsFeO_{2.5}$ with Cr_2O_3 to form Cr_2CrO_4.

This test confirms that Cs-Fe-O compounds can be decomposed and then react with Cr_2O_3 to form stable Cs_2CrO_4 starting from low temperatures. This means that Cs-Fe-O will only be formed if the availability of Fe is quite abundant compared to Cr. However, when Cr is available, then they will tend to form Cs_2CrO_4 rather than Cs_2FeO_4 and/or $CsFeO_{2.5}$.

4.3 Discussion

4.3.1 CsOH Reactions with Major Oxides

The interaction of CsOH with structural materials is closely related to several factors, especially temperature, reactants availability, and pre-oxide film condition (Cantrel and Krausmann, 2003). These factors directly affect the formed Cs compounds including the amount of its retention.

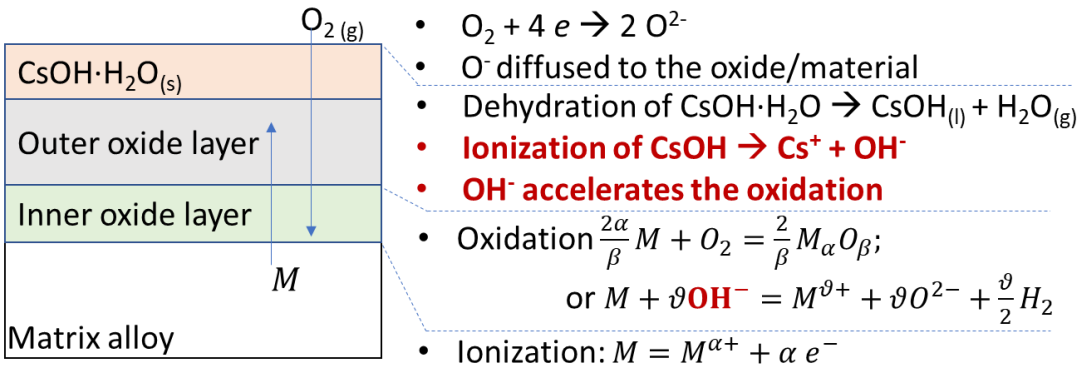

Figure 4.14. Schematic interaction between CsOH precursor with the oxide film.

The amount of Cs residual is higher on the oxidized compared to the unoxidized specimens. This occurs due to the oxides amount differences which act as the reactant that is ready to react with CsOH. As illustrated in Figure 4.14, oxidation happens due to the migration of material elements to the surface and the diffusion of oxygen into the material. The oxidation rate and oxide film formation arrangement are varying for each material and alloy depending on their thermodynamic properties as described in Section 3. When CsOH is introduced onto the surface of specimens, there is a difference in starting point between pre-oxidized and unoxidized specimens. Pre-oxidized specimens already have an oxide film on their surface that is ready to react with CsOH, while unoxidized specimens still do not have it. Therefore, the availability of reactants from the pre-oxidized specimen should be technically higher than that of the non-oxidized

specimen. Although oxidation makes the metal chemically more stable, it can still be ionized and react with $CsOH{\cdot}H_2O$. The reactants availability differences directly affect the newly formed Cs compounds, which are expected to be higher from pre-oxidized rather than unoxidized specimens.

When subjected to heat treatment, $CsOH{\cdot}H_2O$ decomposes by releasing surface water and crystalline-bound H_2O. H_2O undergoes evaporation (see Appendix A), while CsOH ionizes to form Cs^+ and OH^-. As had been observed by the previous study (Chang *et al.*, 1992), OH^- ion is highly corrosive and could accelerate the oxidation mechanism. As the most abundant element in SS and Ni-based alloys, the oxide of Fe, Ni, and Cr especially in the form of Fe_2O_3, Cr_2O_3, NiO, and with the rest related to $NiFe_2O_4$, $NiCr_2O_4$, and/or $FeCr_2O_4$ spinels are expected to dominate the oxide layer. Therefore, these oxides also have a great opportunity to react with Cs^+. Meanwhile, Ni and its oxides tend to be inert with Cs^+ so only the formation of Cs-Fe-Cr-O compounds can be formed.

4.3.2 Effect of pH on the Formation of Cs-Fe-Cr-O

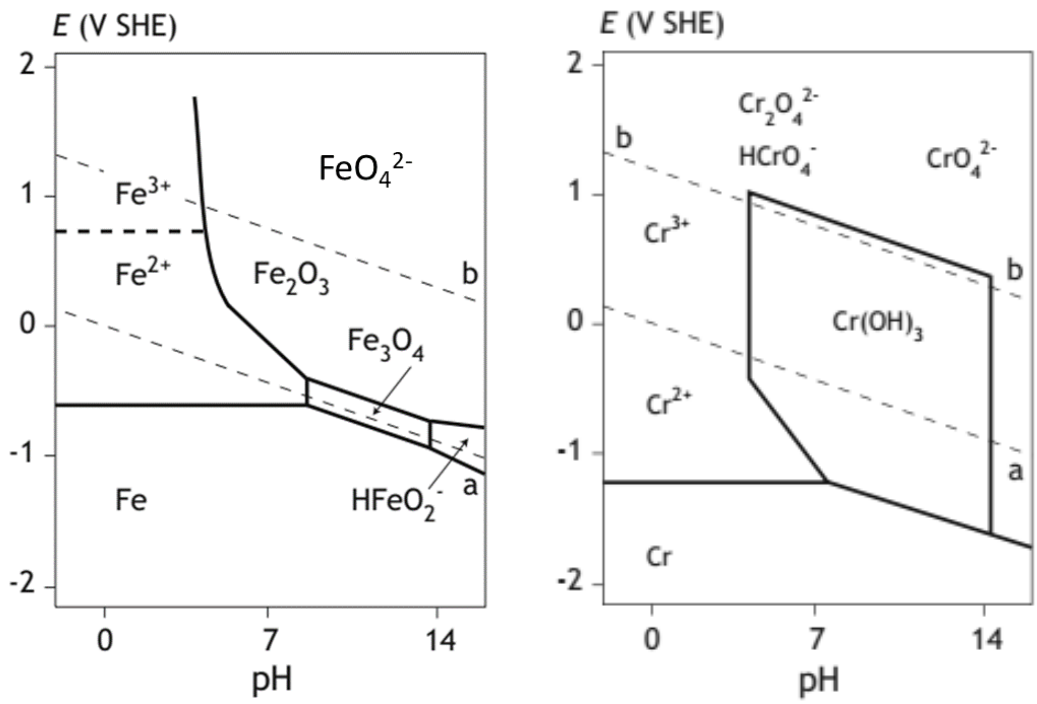

Figure 4.15. Pourbaix diagram, *E*-pH, for iron and chromium.

A previous study as explained by (Kopelev, Popov and Val'kovskii, 1994) observes that Cs_2FeO_4 is unstable, especially at higher temperatures that make it decomposed to be

$CsFeO_{2.5}$. Nevertheless, $CsFeO_{2.5}$ cannot be detected in this study. Instead, this study can only detect the formation of Cs_2FeO_4 and Cs_2CrO_4 which are formed on the specimens treated at 300-600 °C and 300-900 °C, respectively.

The reason for the large formation of Cs_2FeO_4 instead of $CsFeO_{2.5}$ is related to the effect of hydrogen potential (pH) and voltage potential. These factors are correlated to the temperature treatment as shown by the Nernst equation (Sequeira, 2019). As explained by the Pourbaix diagram shown in Figure 4.15 (Pedeferri, 2018, p. 65), when the voltage potential $E \geq \sim 1$, Fe (III) tends to be formed when the pH is low, while Fe (VI) could be formed when the pH is high. In the case of this study, a large amount of $CsOH{\cdot}H_2O$ is directly put into the specimens. $CsOH{\cdot}H_2O$ consists of hydroxide ions and therefore becomes a strong base with high pH, especially at low temperatures. With such a high pH environment, Fe tends to be oxidized to become Fe(VI) in the form of FeO_4^{2-}. FeO_4^{2-} furthermore could capture 2 Cs^+ to form Cs_2FeO_4.

Due to its corrosive nature, OH^- actively reacts with the material's elements to form oxides, releasing water vapor and then increasing the thickness of oxide film. This mechanism ultimately results in a reduction of OH^- concentration, so that the pH also decreases. The decrease in the pH eventually causes Fe(VI) in the form of Cs_2FeO_4 to become unstable and undergoes decomposition especially to be $CsFeO_{2.5}$ as illustrated in Figure 4.16. Even so, due to the increasing amount of Cr in line with the oxidation growth mechanism, $CsFeO_{2.5}$ may react with $NiCr_2O_4$, $FeCr_2O_4$, and/or Cr_2O_3 to form Cs_2CrO_4 and Fe_2O_3. As shown by the Pourbaix diagram in Figure 4.16, Cr(VI) is stable at all pH, which means the formation of Cs_2CrO_4 can be formed at all temperature treatments.

Formation energy can be used as an indicator related to the chemical compound stability. As shown by (Jain *et al.*, 2013), the energy formation of Cs_2CrO_4 is about -2.082 eV. While the energy formation of Cs_2FeO_4 and $CsFeO_{2.5}$ are around -1.520 eV and -1.862 eV, respectively. This information indicates that Cs_2CrO_4 is more stable than $CsFeO_{2.5}$ and Cs_2FeO_4.

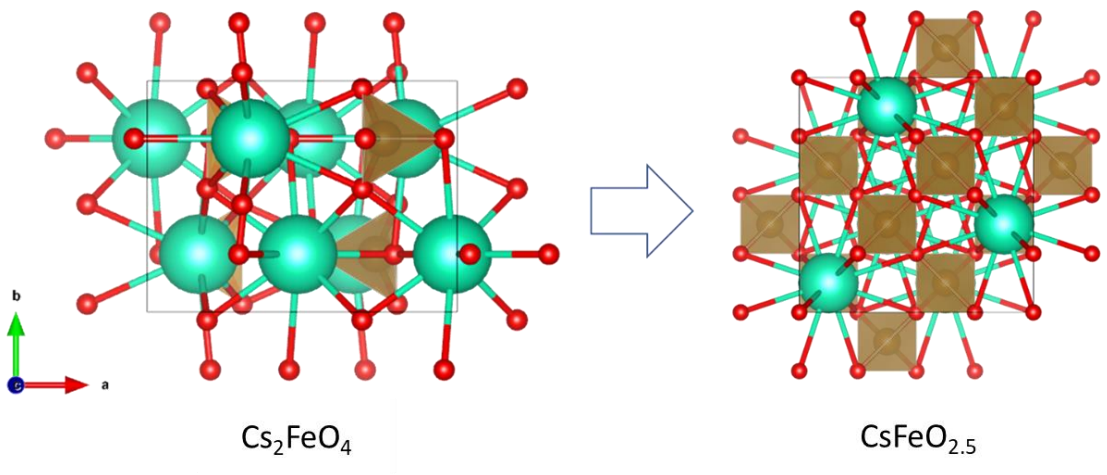

Figure 4.16. Crystal structures of Cs_2FeO_4 and $CsFeO_{2.5}$ compounds.

Understanding physicochemical properties of both Cs_2FeO_4 and $CsFeO_{2.5}$ as well as Cs_2CrO_4 may be important for source terms transport model improvement by considering these compounds are not yet be taken into account as part of the chemical database, especially for LWR SA codes. The importance of cesium iron oxides due to their potential as powerful oxidizing agents had been identified especially related to Liquid Metal Fast Breeding Reactor (LMFBR) systems (Meigh, 2019). Thermodynamic properties of some cesium iron oxide species such as those related to $Cs_8Fe_2O_7$, $Cs_5Fe_3O_6$, and $CsFeO_2$ had been calculated theoretically (Lindemer, Besmann and Johnson, 1981). However, Cs_2FeO_4, including the thermodynamic properties of $CsFeO_{2.5}$, are still poorly understood. An in-depth study of cesium iron oxides is needed, considering that Fe is one of the elements with the greatest abundance in nuclear reactors. The formation of the Cs_2CrO_4 compound which can be formed due to the interaction between CsOH with stainless steel structural materials has been observed such as by (Allen *et al.*, 1987). Its thermodynamic properties from low to high temperatures also had been studied such as by (Fredrickson, Johnson, and O'Hare, 1980), and (Lyon, Osborne, and Flotow, 1975).

4.4 Summary

Higher Cs retention on pre-oxidized compared with that on unoxidized specimens is related to the higher abundance of reactants in the form of oxide compounds.

Both SS and Ni-based alloys consist of a high abundance of Fe, Ni, and Cr. Fe and Cr tend to react with Cs forming cesium iron oxides and cesium chromium oxides,

while Ni is relatively inert with Cs. A high abundance of Cs_2FeO_4 can be formed from all types of materials treated at 300-600 ^oC. While Cs_2CrO_4 is formed in all specimens treated at all temperatures. More stable cesium iron oxide species in the form of $CsFeO_{2.5}$ cannot be observed in this study. That is related to the pH of the reaction environment which pushes the oxidation state of iron to be Fe(VI), which tends to form Cs_2FeO_4. Although at higher temperatures Cs_2FeO_4 decomposes to be $CsFeO_{2.5}$, however, $CsFeO_{2.5}$ may react with Cr_2O_3 to form a more stable Cs_2CrO_4.

Synthesizing and characterizing Cs-Fe-Cr-O ensure the existence of Cs_2FeO_4 and Cs_2CrO_4, as well as confirming why $CsFeO_{2.5}$ cannot be observed from the main experiment. Cs_2FeO_4 is largely formed due to the high pH level of the reaction environment, especially at lower temperatures. Although pH levels decrease at higher temperatures and encourage the decomposition of Cs_2FeO_4, to be $CsFeO_{2.5}$, however, Cr_2O_3 reacts with $CsFeO_{2.5}$ to form Cs_2CrO_4. Cs_2CrO_4 is stable at all temperature treatments but melted and easily evaporated at ≥ ~957 °C.

4.5 References

Abe, F. et al. (1981) 'The effect of grain size on the corrosion behaviour of inconel 600 in high-temperature steam', Corrosion Science, 21(12), pp. 819–842. doi: 10.1016/0010-938X(81)90024-X.

Allen, G. C. et al. (1987) 'Surface studies of the interaction of cesium hydroxide vapor with 304 stainless steel', Oxidation of Metals, 28(1–2), pp. 33–59. doi: 10.1007/BF00666470.

Brockmann, J. E. (1987) 'Ex-vessel releases: Aerosol source terms in reactor accidents', Progress in Nuclear Energy, 19(1), pp. 7–68. doi: 10.1016/0149-1970(87)90003-5.

Cantrel, L. and Krausmann, E. (2003) 'Reaction kinetics of a fission-product mixture in a steam-hydrogen carrier gas in the phebus primary circuit', Nuclear Technology, 144(1), pp. 1–15. doi: 10.13182/NT03-A3425.

Chang, S. J. et al. (1992) ‘Corrosion of Austenitic Stainless Steel in Steam Containing Cesium Hydroxide’, Journal of Nuclear Science and Technology, 29(8), pp. 753–761. doi: 10.3327/jnst.29.753.

Clément, B. et al. (2003) ‘LWR severe accident simulation: Synthesis of the results and interpretation of the first Phebus FP experiment FPT0’, Nuclear Engineering and Design, 226(1 SPEC. ISS.), pp. 5–82. doi: 10.1016/S0029-5493(03)00157-2.

Fernandez-Moguel, L., Rydl, A. and Lind, T. (2019) ‘Updated analysis of Fukushima unit 3 with MELCOR 2.1. Part 1: Thermal-hydraulic analysis’, Annals of Nuclear Energy. Elsevier Ltd, 123, pp. 59–77. doi: 10.1016/j.anucene.2018.09.008.

Firnhaber, M. et al. (1996) ‘International Standard Problem ISP37: VANAM M3. A Multicompartment Aerosol Depletion Test with Hygroscopic Aerosol Material’. Moulineaux: Committee on the Safety of Nuclear Installations OECD Nuclear Energy Agency.

Fredrickson, D. R., Johnson, G. K. and O’Hare, P. A. G. (1980) ‘Cesium chromate, Cs2CrO4: high-temperature enthalpy increments and other thermodynamic properties’, Journal of Chemical Thermodynamics, 12(8), pp. 801–805. doi: 10.1016/0021-9614(80)90179-2.

Gupta, S. (2015) ‘Experimental investigations relevant for hydrogen and fission product issues raised by the Fukushima accident’, Nuclear Engineering and Technology, 47(1), pp. 11–25. doi: 10.1016/j.net.2015.01.002.

Jain, A. et al. (2013) ‘Commentary: The materials project: A materials genome approach to accelerating materials innovation’, APL Materials, 1(1). doi: 10.1063/1.4812323.

Kopelev, N. S., Popov, A. I. and Val’kovskii, M. D. (1994) ‘Properties of the products of CsxFeO2+0.5x thermal decomposition’, Journal of Radioanalytical and Nuclear Chemistry Letters, 188(2), pp. 99–108. doi: 10.1007/BF02164943.

Lind, T. et al. (2020) ‘A summary of fission-product-transport phenomena during SGTR severe accidents’, Nuclear Engineering and Design, 363(April), p. 110635. doi: 10.1016/j.nucengdes.2020.110635.

Lindemer, T. B., Besmann, T. M. and Johnson, C. E. (1981) ‘Thermodynamic review and calculations—alkali-metal oxide systems with nuclear fuels, fission products, and structural materials’, Journal of Nuclear Materials, 100(1–3), pp. 178–226. doi: 10.1016/0022-3115(81)90533-X.

Lyon, W. G., Osborne, D. W. and Flotow, H. E. (1975) ‘Cesium chromate, Cs2CrO4: heat capacity and thermodynamic properties from 5 to 350 K’, The Journal of Chemical Thermodynamics, 7(12), pp. 1189–1194. doi: 10.1016/0021-9614(75)90041-5.

Meigh, H. J. (2019) Ternary Alloy Systems, Cast and Wrought Aluminium Bronzes. doi: 10.1201/9781315138848-13.

Nishimura, T., Hoshi, H. and Hotta, A. (2015) ‘Current research and development activities on fission products and hydrogen risk after the accident at fukushima daiichi nuclear power station’, Nuclear Engineering and Technology, 47(1), pp. 1–10. doi: 10.1016/j.net.2014.12.002.

Pedeferri, P. (2018) Corrosion Science and Engineering. Pedeferri,. Cham: Springer International Publishing (Engineering Materials). doi: 10.1007/978-3-319-97625-9.

Sehgal, B. R. (2012) Nuclear Safety in Light Water Reactors, Nuclear Safety in Light Water Reactors. Elsevier. doi: 10.1016/C2010-0-67817-5.

Sequeira, C. A. C. (2019) High Temperature Corrosion. Hoboken, NJ, USA: John Wiley & Sons, Inc. doi: 10.1002/9781119474371.

Toth, B. et al. (2007) ‘Benchmark study on fuel bundle degradation in the phebus FPT3 test using the severe accident codes ATHLET-CD, ICARE2, and MELCOR’, Nuclear Technology, 157(2), pp. 132–142. doi: 10.13182/NT07-A3808.

Tóth, B. et al. (2010) ‘Benchmark study on fuel bundle degradation in the phebus FPT2 test using state-of-the-art severe accident analysis codes’, Nuclear Technology, 169(2), pp. 81–96. doi: 10.13182/NT10-A9354.

Watanabe, A., Yamada, K. and Ohsaki, M. (2009) ‘FP Aerosol Trapping Effect Along the Leakage Paths of Degraded Containment Penetrations During a Severe

Accident (II) Decontamination Factor at the Containment Penetrations and Its Application to Actual Plant’, Transactions of the Atomic Energy Society of Japan, 8(4), pp. 332–343. doi: 10.3327/taesj.J08.052.

Williams, D. B. and Carter, C. B. (2009) Transmission Electron Microscopy, Kobunshi. Boston, MA: Springer US. doi: 10.1007/978-0-387-76501-3.

(This page intentionally left blank)

Chapter 4

Oxidation, Solute Elements, and Cs Chemisorption

(This page intentionally left blank)

Science never solves a problem without creating ten more.

~George Bernard Shaw

(This page intentionally left blank)

Chapter 5

Oxidation, Solute Elements, and Cs Chemisorption

5.1 Introduction

Cs retention onto structural materials may happen by following several ways, both physically and/or chemically. Physical retention happens through adhesion, cohesion, or surface tension attraction between different and/or similar types of materials. These attractions can be caused by hydrogen bonding, polar attraction, dipole-dipole interactions, Van der Waals force, etc. (Callister and Rethwisch, 2013, pp. 32–45). Physical retention usually occurs with relatively low binding energy thus making it easier to be removed. Cs may also be retained by forming such compounds with strong joints where the atoms between Cs and the material's surface share electrons following covalent or ionic bonding. These chemical bonds make Cs tightly retained to the material, so it is relatively difficult to remove. The retention associated with these chemical bonds hereinafter refers to chemisorption (Walton *et al.*, 2014).

The interaction between Cs and material in this experiment is started with physical interaction by placing $CsOH{\cdot}H_2O$ on the surface of the target specimens and then forming a thin film. Physical interactions are then followed by chemical reactions involving liquid $CsOH{\cdot}H_2O$ precursor, oxygen from the air, and the elements contained in the target specimens. Complex chemical reactions then produce various types of new compounds including the growth of the oxide layers and the formation of various new Cs compounds. Although several new Cs compounds can be formed through chemical reactions, some of them do not bound strongly. The weak retention may be caused by various factors, such as its characteristic which is easily dissolved in water, formed on a brittle oxide layer, etc. The new Cs compound which is not strongly attached to the material should be excluded from the chemisorption. Therefore, this chapter discusses the characterization of Cs compounds which are indicated to be strongly attached to the materials.

5.2 Effect of Solute Al, Ti, and Si on Cs Chemisorption

5.2.1 Cs Chemisorption Identification

5.2.1.1 XRD Analysis of Post-soaked Specimens

Generally, post-soaked XRD analysis of oxidized and unoxidized specimens after the soaking procedure is the same. Because of that, only XRD peaks from oxidized specimens are shown in Figures 5.1 – 5.4. As shown in these figures, the XRD patterns of post-soaked specimens of all types of materials are almost similar compared to the pre-oxidized specimens before being exposed to CsOH precursors. All peaks of the patterns are mainly related to the base materials and their oxides. It means Cs compounds as had been identified from pre-soaked specimens in Chapter 4, especially Cs_2FeO_4, and Cs_2CrO_4 are diluted. Cs_2FeO_4 and Cs_2CrO_4 should be water-soluble. The remaining Cs compounds which are chemisorbed to the specimens are measly which makes them cannot be detected by XRD.

5.2.1.1.1 Post-soaked SS 304

Although oxidation and CsOH precursor reaction with the oxide film of SS 304 already occurred when specimens are treated at 300 and 450 °C, however as shown in Figure 5.1, all the XRD peaks from these specimens are only related to the base material. This indicates both Cs compounds and formed oxide compounds are largely diluted and leaving only a thin oxide film that is unable to produce sufficient XRD peaks. However, unlike the peaks from the pre-oxidation stage, high-intensity peaks that are strongly related to Fe_2O_3, Cr_2O_3, and spinel of $NiCr_2O_4$, and/or $NiFe_2O_4$ can be observed from specimens treated starting from 600 °C. It shows that oxidation is heavily occurred starting from lower temperatures as also had been observed by (Chang *et al.*, 1992). XRD peaks from specimens annealed at 750 and 900 °C also show the same pattern as specimens treated at 600 °C. Nevertheless, the specimen treated at 1050 °C is fragile and broken during the soaking, which makes it difficult to be measured by XRD. However, it should be noted that $NiCr_2O_4$ and $NiFe_2O_4$ spinels are isomorphic and impossible to be distinguished by XRD. Nevertheless, these compounds may exist in small quantities.

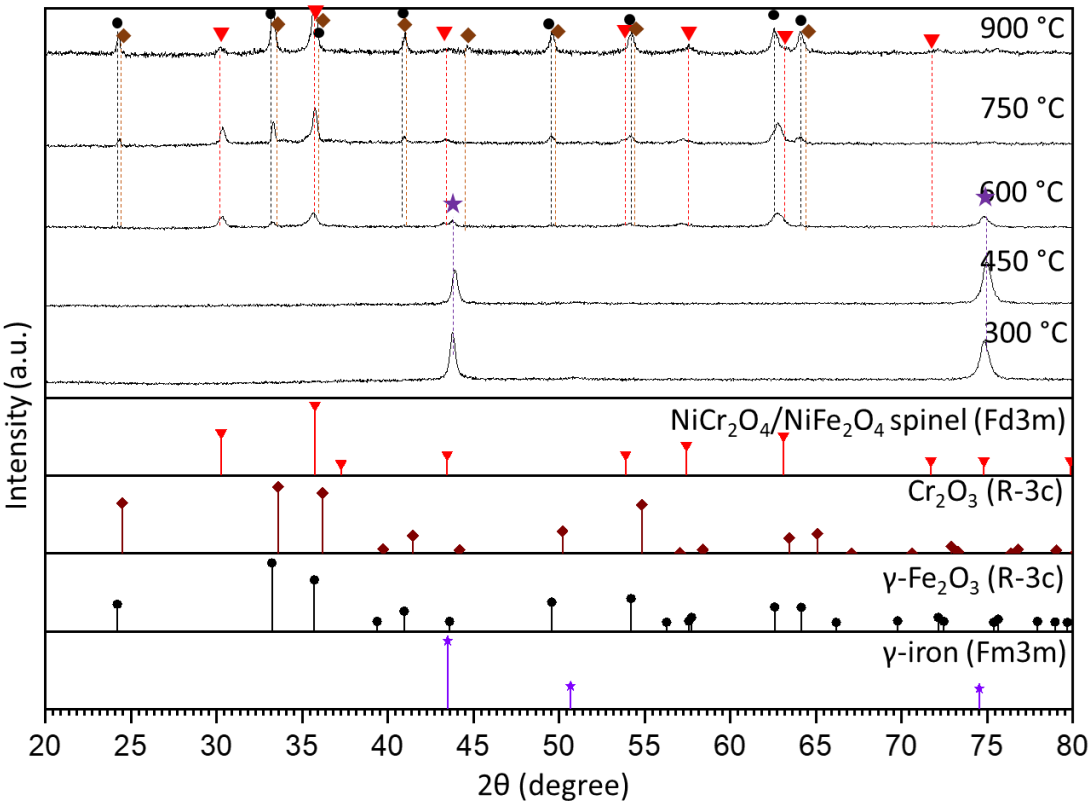

Figure 5.1 XRD peaks of post-soaked SS 304 are only related to the base material, Fe_2O_3, Cr_2O_3, and spinel of $NiCr_2O_4$, and/or $NiFe_2O_4$.

5.2.1.1.2 Post-soaked SS 321

As shown in Figure 5.2, XRD peaks of post-soaked SS 321 specimens are also like their pre-oxidation. The XRD patterns are mainly showing the formation of base material, and some oxides of major elements. Clearer oxides-related peak intensity of post-soaked specimens compared with pre-oxidized specimens indicated thicker oxide films are also expected. Base material-related peaks with some variation compared with the peaks of pre-oxidation specimens indicating crystal structure changing can be observed from specimens treated at 300 - 600 °C. Fe_2O_3, Cr_2O_3, including $NiCr_2O_4$, and/or $NiFe_2O_4$-related peaks are formed from all specimens treated at 750-1050 °C. Some small peaks especially from specimens treated at 900 °C still exist and cannot be well-identified. These peaks may be related to such kinds of Cs compounds. As isomorphic compounds and with relatively small peak intensities, the existence of $NiCr_2O_4$, and $NiFe_2O_4$ in SS 321 are unclear. However, SEM/EDS observation suggests these elements may exist measly.

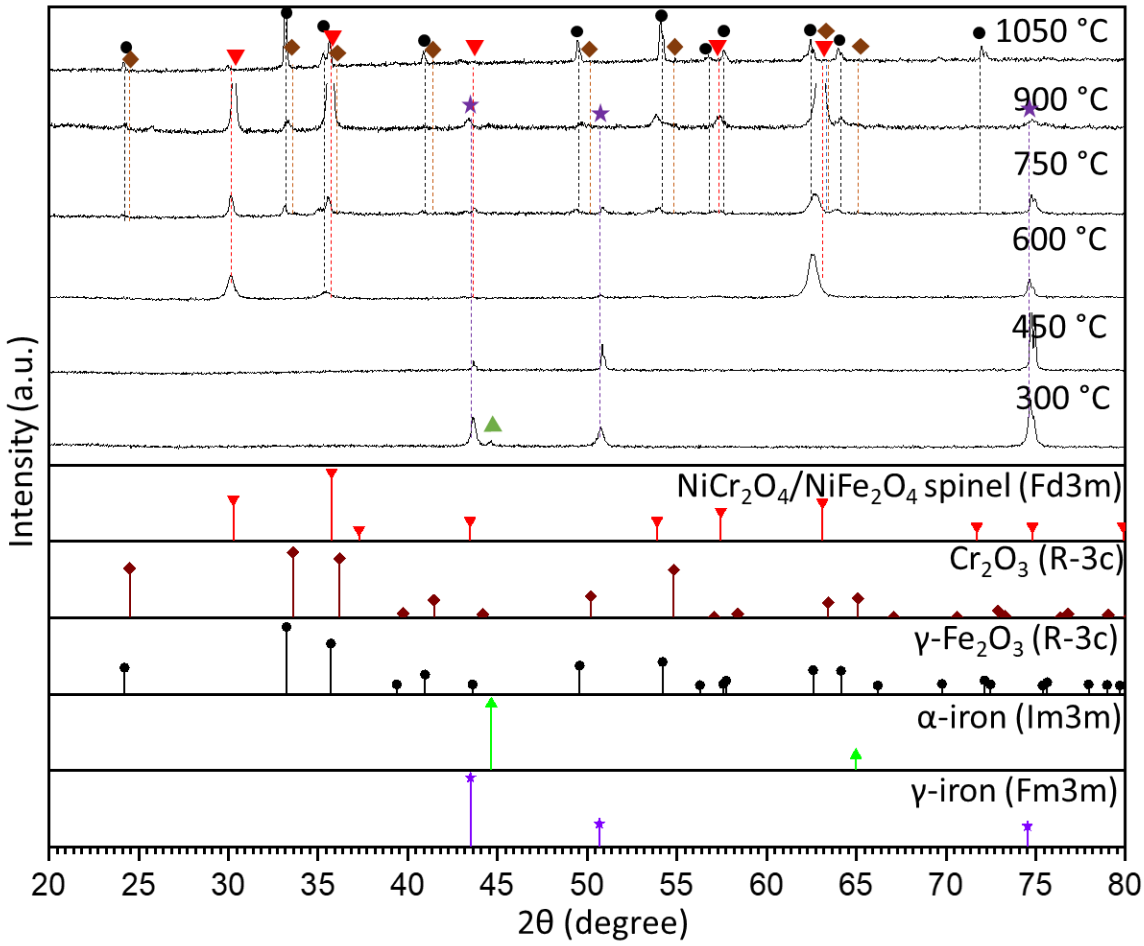

Figure 5.2. XRD analysis of post-soaked SS 321 only indicates the formation of base material, Fe_2O_3, Cr_2O_3 and $NiCr_2O_4$, and/or $NiFe_2O_4$ spinels.

5.2.1.1.3 Post-soaked Inconel 600

By comparing the XRD peaks of post-soaked Inconel 600 specimens with their pre-oxidation, the similarity between them clearly can be seen. However, as shown in Figure 5.3, all peaks of Inconel 600 specimens are mainly related to NiO and Cr_2O_3. $NiCr_2O_4$, and/or $NiFe_2O_4$ spinel-related peaks with the absence of Fe_2O_3, $FeCr_2O_4$, and TiO_2 are also detected with relatively low intensity. The absence of Fe_2O_3 and $FeCr_2O_4$ should be related to the formation of Cs_2FeO_4 and Cs_2CrO_4 which are completely diluted during soaking. Interestingly, NiO-related peaks that appear from pre-oxidation specimens treated starting from 600 °C can be observed starting from 450 °C from post-soaked specimens. Like the phenomenon that happened in SS 304 and SS 321, this must be evidence of the oxidation acceleration due to CsOH. Some small peaks which might be related to other compounds also appeared. However, it was difficult to be identified.

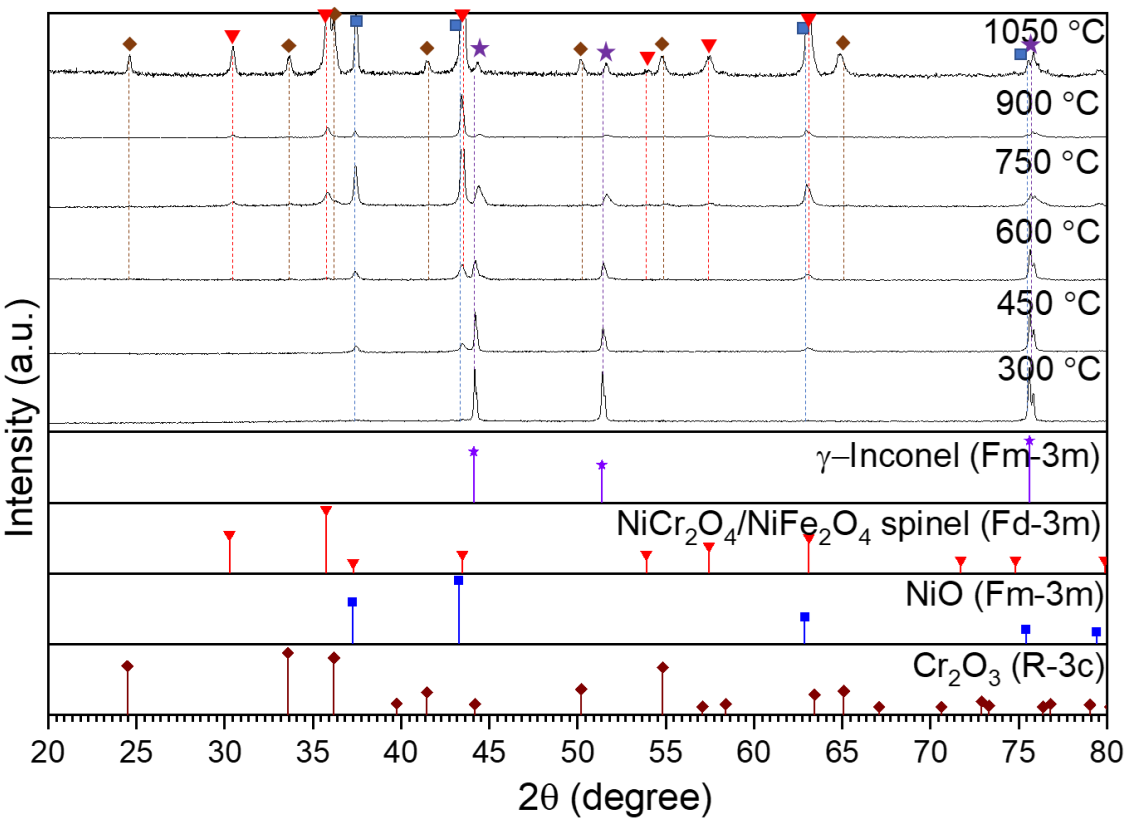

Figure 5.3. XRD analysis of post-soaked Inconel 600 showing the formation of base material, Cr_2O_3, NiO, and spinel of $NiCr_2O_4$, and/or $NiFe_2O_4$.

5.2.1.1.4 Post-soaked X-750

Thicker oxide film in post-soaked compared with their pre-oxidation specimens is observed from X-750 alloy. This indication can be confirmed by the relatively higher peaks related to oxide compounds which can be observed starting from specimens treated at 450 °C. While from its pre-oxidation stage as shown in Section 3, only can be observed starting from specimens annealed at 900 °C. As shown in Figure 5.4, the peaks of post-soaked X-750 specimens are mainly related to NiO, Cr_2O_3, and/or $(Cr_{0.88}Ti_{0.12})_2O_3$, and TiO_2. The rest peaks are related to $NiFe_2O_4$, and/or $NiCr_2O_4$ spinels. However, it must be noted that besides $NiFe_2O_4$, and $NiCr_2O_4$ spinel, the XRD pattern of Cr_2O_3, and $(Cr_{0.88}Ti_{0.12})_2O_3$ are also almost identical and difficult to distinguish. Nevertheless, SEM/EDS observation suggests that Cr_2O_3, and $(Cr_{0.88}Ti_{0.12})_2O_3$ may exist in relatively large quantities, while $NiFe_2O_4$, and/or $NiCr_2O_4$ are scrimp. Similar to Inconel 600, undetected Fe_2O_3 and $FeCr_2O_4$ must be related to the formation of Cs_2FeO_4 and Cs_2CrO_4 on the surface which is completely diluted during soaking.

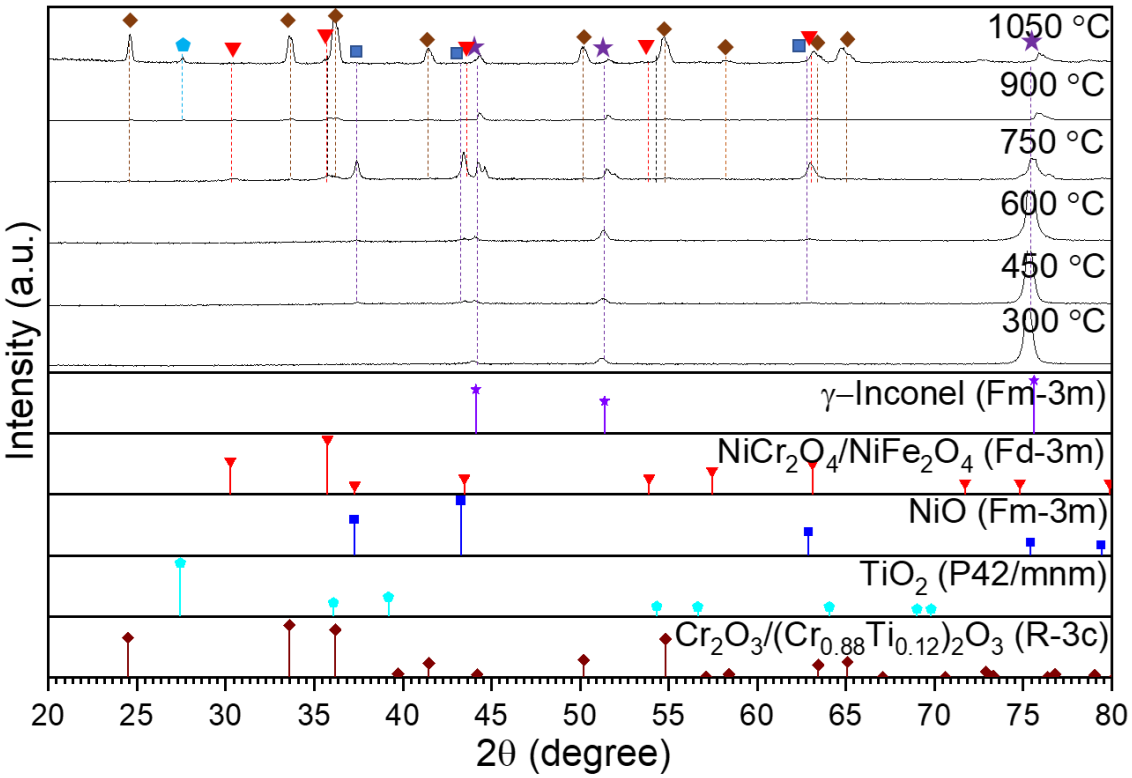

Figure 5.4. Base material, NiO, Cr_2O_3, and/or $(Cr_{0.88}Ti_{0.12})_2O_3$, TiO_2, $NiCr_2O_4$, and/or $NiFe_2O_4$ spinels are identified from XRD analysis of post-soaked X-750.

5.2.1.2 SEM/EDS Observation of Post-soaked Specimens

Detailed Cs chemisorption identification is performed through SEM/EDS observation. Figure 5.5 shows the image of post-soaked specimens which had previously undergone pre-oxidation before being exposed to the $CsOH{\cdot}H_2O$ precursor. Similar surface conditions also can be observed from unoxidized specimens.

The rough surface of the specimens shown in Figure 5.5 indicates heavy oxidation had occurred during $CsOH{\cdot}H_2O$ exposure. Large oxide film removal occurred during the soaking procedure, leaving a partial oxide layer that adheres strongly to the materials. This mechanism not only partially destroys the oxide layer but also removes most of the Cs compounds. Nevertheless, a small amount of Cs can be observed with several formations' variations depending on the material and the temperature treatment.

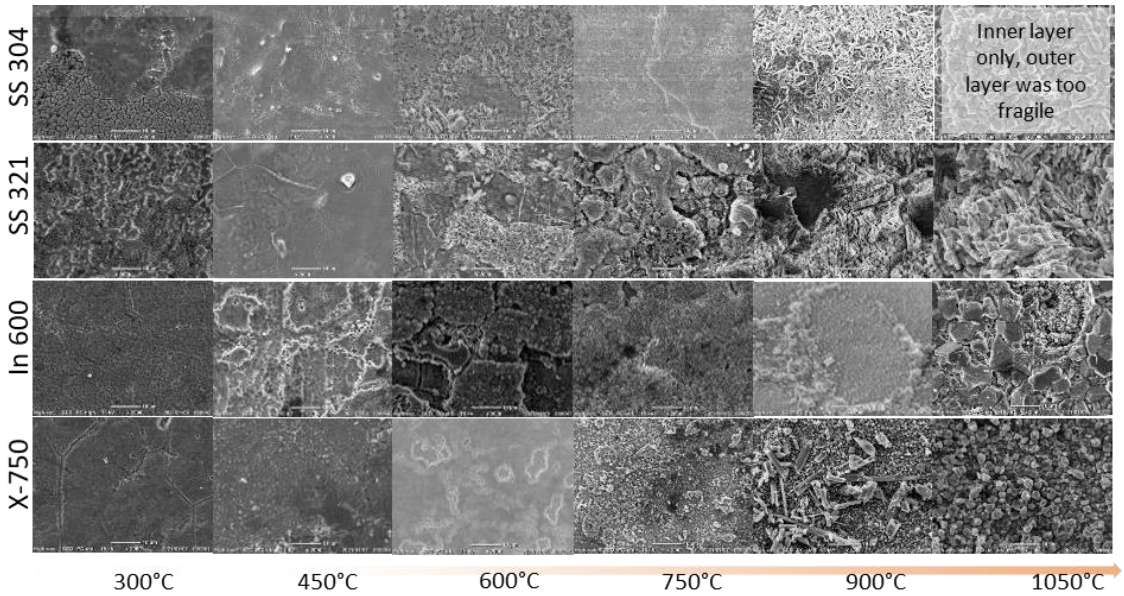

Figure 5.5. Surface morphologies of post-soaked specimens.

As shown in Figure 5.6, quantitative EDS is conducted to measure the amount of Cs residual on the surface of each specimen. Quantitative EDS is taken at 1200 µm x 900 µm scanning areas to ensure the representativeness of the entire surface of the specimens by focusing only on the atomic percentage of Cs and some minor elements. These minor elements are selected because they appear to relate with the chemisorbed Cs elements. Despite the uncertainty of quantitative EDS measurement, the amount of Cs in oxidized specimens is generally higher than in unoxidized specimens as previously indicated by the measurement of pre-soaked specimens. This phenomenon may be related to the availability of important compounds, particularly solute Al, Si, and Ti, which are larger in oxidized specimens compared to unoxidized specimens.

The amount of Cs on the specimens treated at 300 °C is low, even under the detection limit of quantitative EDS. The amount of Cs from specimens treated at 450 °C is almost like the specimens treated at 300 °C. Nevertheless, oxidized X-750 shows the highest amount of Cs, then followed by Inconel 600 and SS 304, while SS 321 has the lowest amount of Cs. Si and Al are also detected with almost similar amounts compared with specimens treated at 300 °C.

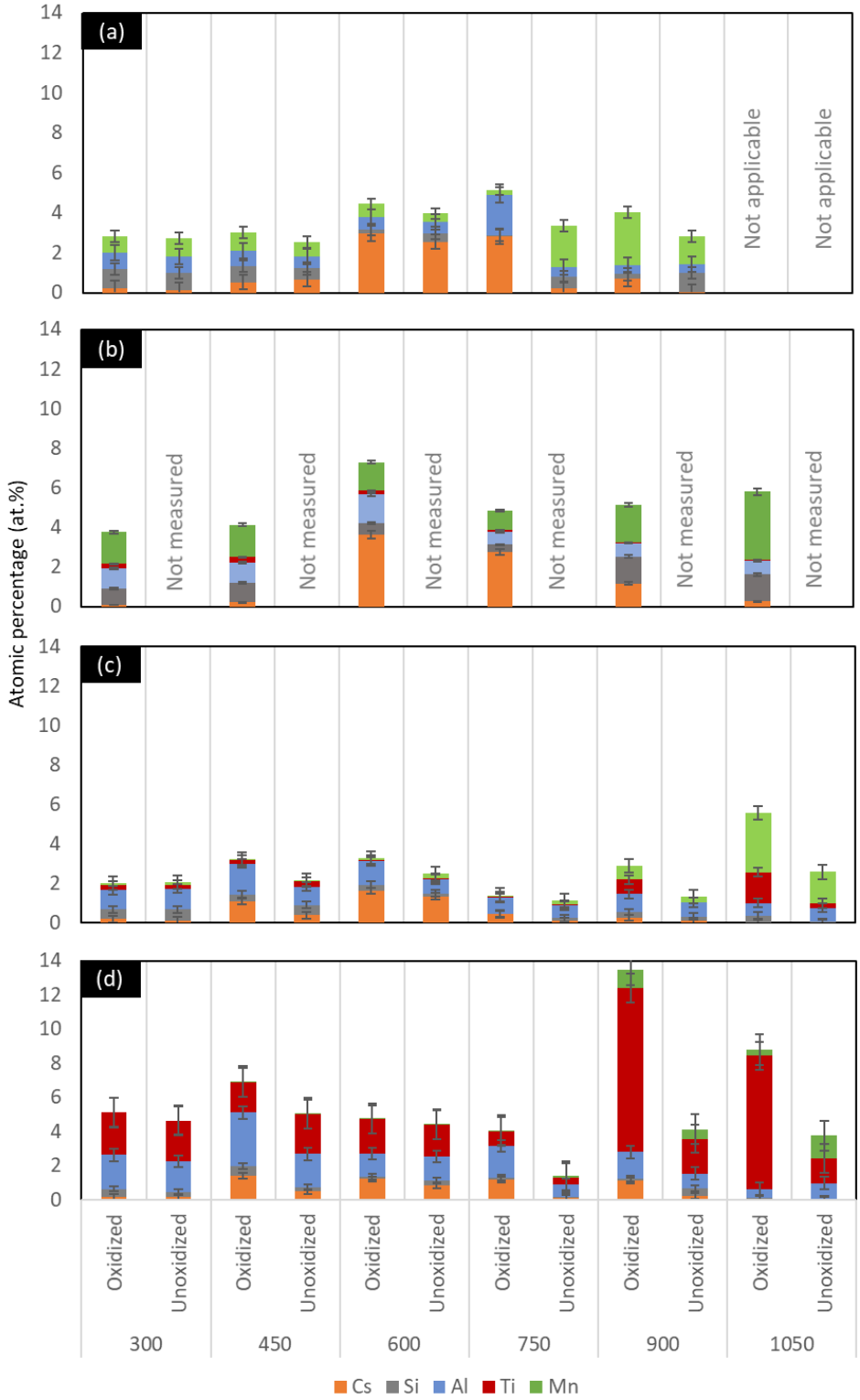

Figure 5.6. Concentration of Cs, Si, Al, Ti, and Mn on surface of post-soaked (a) SS 304, (b) SS 321, (c) Inconel 600 and (d) X-750.

A more reasonable amount of Cs can be detected from specimens treated at 600, 750, and 900 °C. From specimens treated at 600 and 750 °C, the highest amount of Cs is

measured from SS 321, then followed by SS 304, Inconel 600, and X-750. Meanwhile, from the specimens treated at 900 °C, the largest amount of Cs is measured from SS 321 and X-750 then followed by SS 304 and Inconel 600.

At 1050 °C, SS 304 specimen is too fragile, with almost all its oxide film diluted during soaking and leaving only a small part of the base material. Therefore, quantitative EDS measurement for post-soaked SS 304 at this temperature is not carried out. Degradation of the outermost oxide layer in other specimens also occurred, but in relatively small amounts, so it is still worth to be observed. However, from the three remaining specimens, only SS 321 shows an indication that Cs compounds are strongly chemisorbed into the surface of the oxide film. While Inconel 600 and X-750 do not show any indication of remaining Cs.

Detailed correlation between Cs and other elements that may give important insight related to what kind of compounds in each specimen can be seen from EDS mapping and point analysis as discussed in the following subchapters.

5.2.1.2.1 Post-soaked SS 304

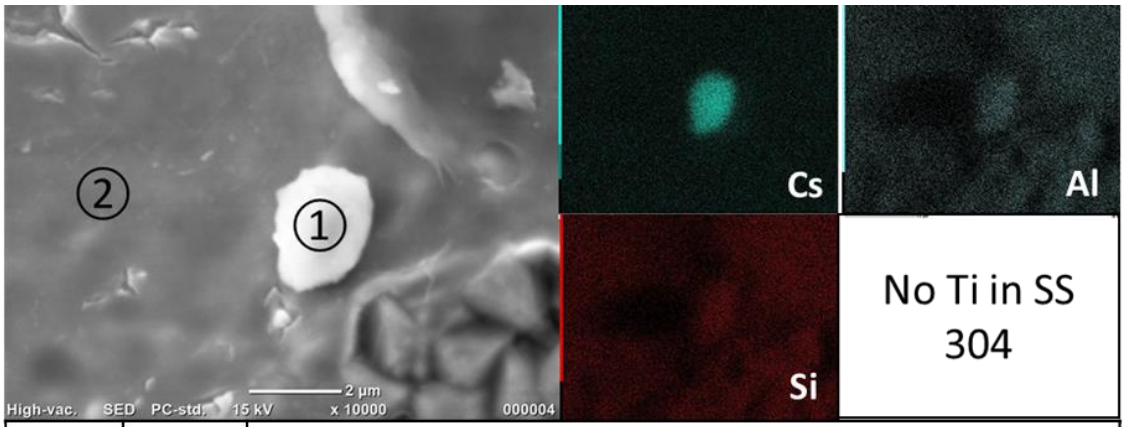

at.%	Point	Cs	Al	Si	Ti	Fe
SS 304	①	3.48±0.17	2.83±0.14	1.04±0.05	-	42.44±2.12
	②	0.15±0.01	0.92±0.05	1.09±0.05	-	64.17±3.21

Figure 5.7 Al-enriched Cs particle retains on post-soaked SS 304 treated at 450 °C.

Although the amount of Cs retention on the surface of SS 304 specimens treated at 300 and 450 °C as shown in Figure 5.6 is measly, however, several Cs particles can be observed adhered with the size of only ~2 µm. SEM/EDS mapping and point analysis

from the post-soaked specimen as shown in Figure 5.7 strongly shows these Cs particles are mainly related to Al, and O, with some particles, also correlated with Si. These indicate the formation of Cs-Al-(Si)-O compounds. Although Figure 5.7 is only showing Cs particles on specimens that have undergone pre-oxidation, however, similar Cs particles can be observed from unoxidized specimens.

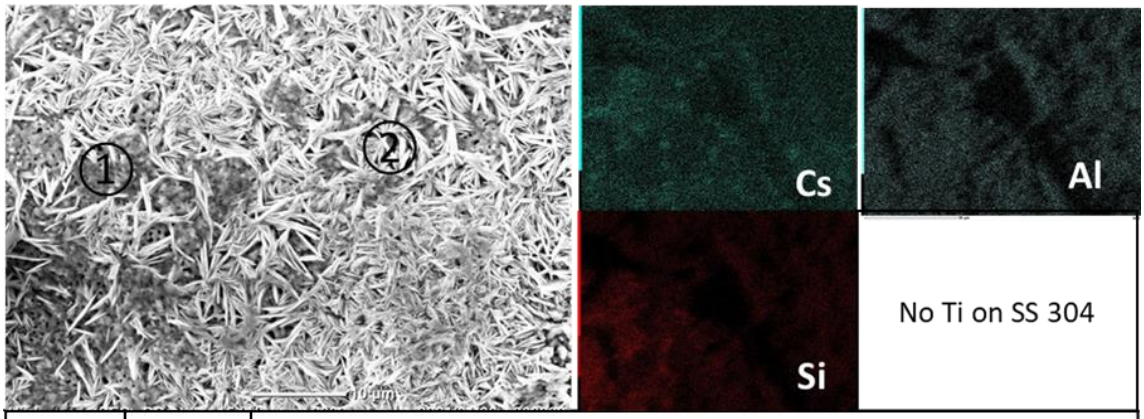

at.%	Point	Cs	Al	Si	Ti	Fe
SS 304	①	3.57±0.18	0.36±0.02	0.25±0.01	-	39.23±1.96
	②	0.41±0.02	0.48±0.03	0.07±0.01	-	39.92±1.20

Figure 5.8. Cs-Al-Si compounds spread in oxide film of post-soaked SS 304 treated at 900 °C.

Small Cs particles as shown in Figure 5.7 cannot be observed from specimens treated at 600 and 750 °C, although the amount of chemisorbed Cs at this temperature is higher. SEM/EDS mapping shows Cs elements are spread and overlap particularly with Fe, Al, and some also with Si. Clearer formation of Cs compounds can be observed from specimens treated at 900 °C. However, as shown in Figure 5.8, Cs compounds mainly relate to Si, although some points are still related to Al.

Interesting results come from cross-sectional SEM/EDS observation of specimens treated at 900 °C as shown in Figure 5.9. Although Cs and specimen interaction is conducted following solid-liquid reaction, similar formation of Cs compounds located on the oxide layer which is also observed in previous gas-solid interaction experiments such as by (Nakajima *et al.*, 2018), (Kobata *et al.*, 2018), (F.G. Di Lemma *et al.*, 2017), (Miradji F.; et al., 2019) can be confirmed. A part of Cs-rich compounds is observed laid between the formation of the Cr-rich area as the inner layer and the Fe-rich area as the outer oxide layer which is mainly overlapped with Si. That

formation should be related to such kind of stable Cs-Si-O compounds which may also relate to Fe, such as in the form of $CsFeSiO_4$, $CsFeSi_2O_6$, $Cs_2Si_2O_5$, and/or $Cs_2Si_4O_9$ as predicted by (Osaka *et al.*, 2016). However, these Cs-Si-O compounds are present in the outer oxide layer. Cs cannot be found to overlap with Si at or below the Cr-rich layer.

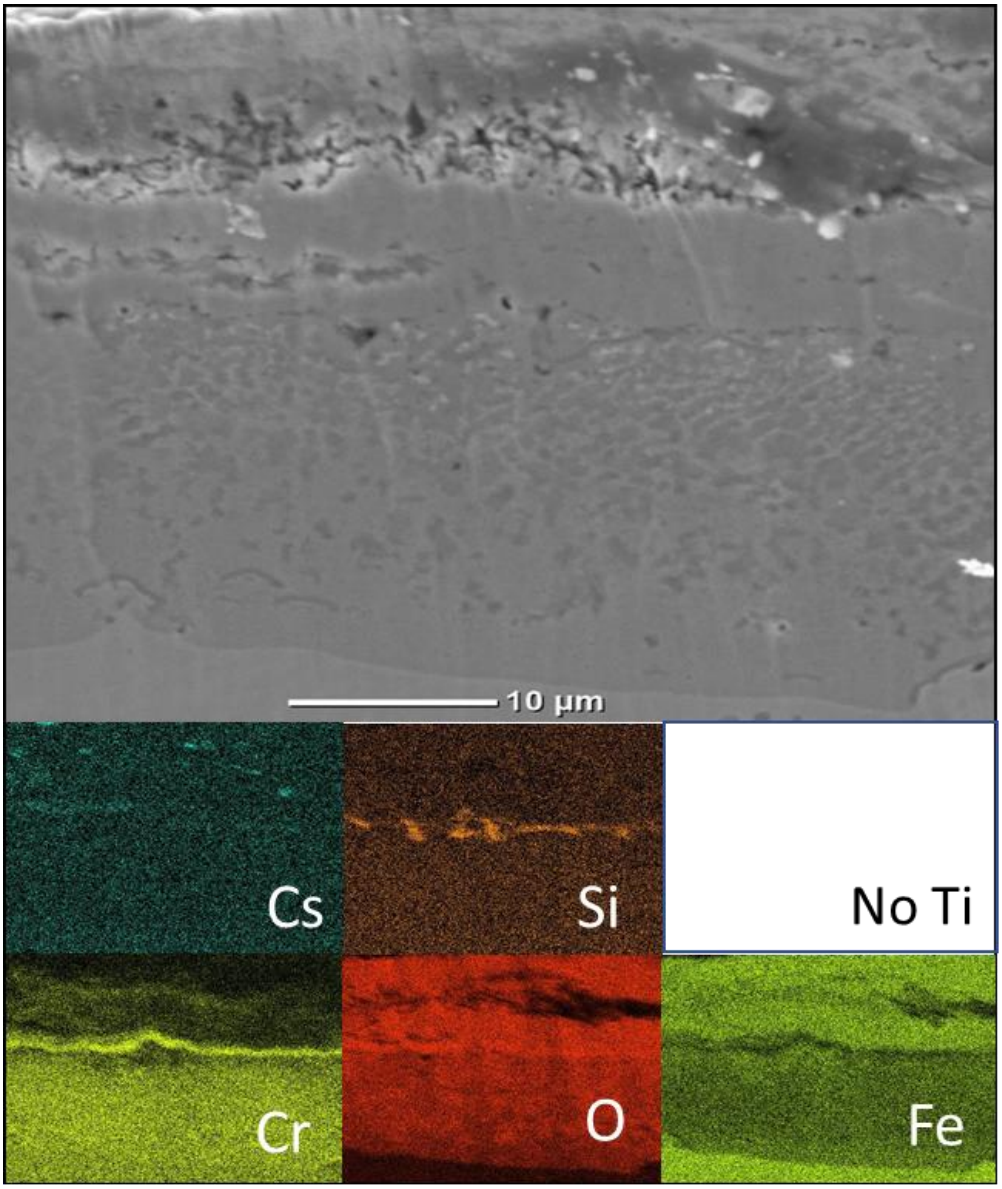

Figure 5.9. Si-enriched Cs formation laid mainly between the inner and outer oxide layers of SS 304 treated at 900 °C.

For several reasons, specimens treated at 1050 °C are essentially incomparable with the specimens treated at lower temperatures. The liquid-solid reaction that occurs in these specimens only lasts a very short time, during the coating process and just after the

temperature reaches 1050 °C. While the other cause is that oxidation occurs quickly. The rapid oxidation makes the oxide layer grows very thick and brittle. These thick and brittle oxide structures cannot survive under actual conditions. However, this specimen still has some meanings related to the oxidation growth and Cs chemisorption mechanisms. As shown in Figure 5.10, SEM/EDS observation indicates that Si-enriched Cs particles are spread in the oxide layer. Interestingly, the formation of Si-enriched Cs particles is mainly concentrated between the inner and outer oxide layers as also observed from specimens treated at 900 °C.

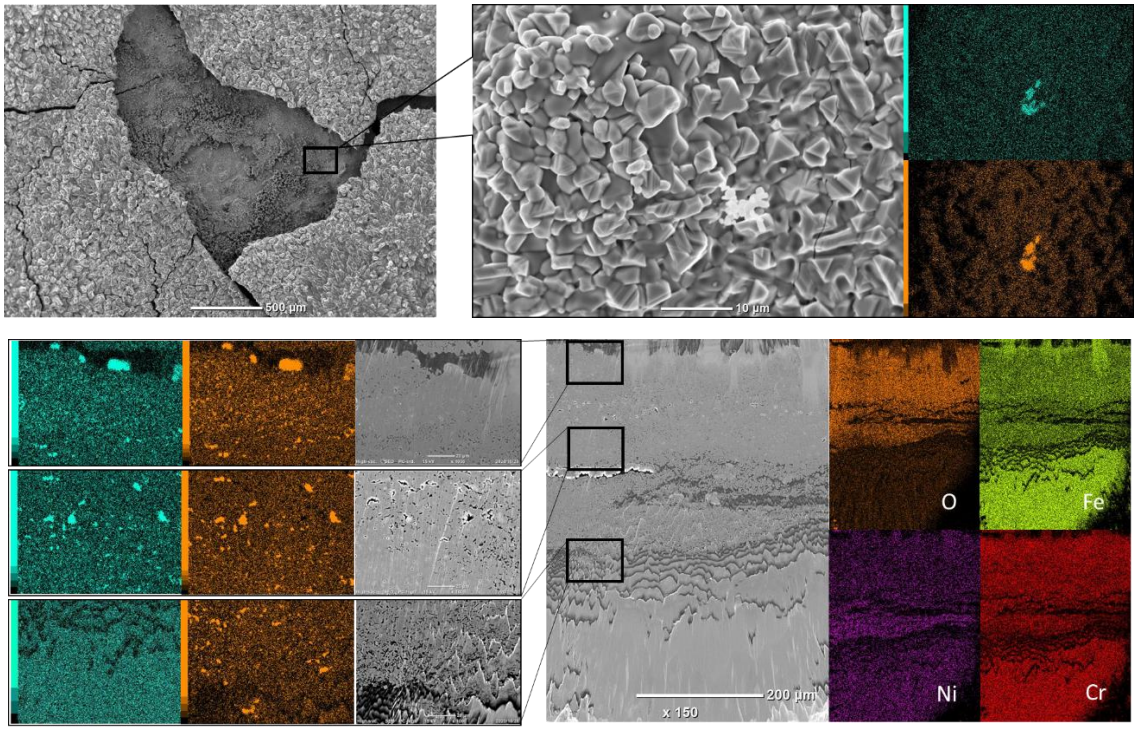

Figure 5.10. Distribution of Cs-Si compounds in oxide film of post-CsOH exposure of SS 304 treated at 1050 °C.

Detailed cross-sectional observation from both oxidized and unoxidized specimens treated at 900 °C and 1050 °C indicates Cs compounds are only located alongside the formation of the outer oxide layer. Cs cannot be observed on or below the Cr-rich layer. This indicates that in the case of solid-liquid interaction, Cs elements cannot diffuse into the material matrix as hypothesized in the solid-gas interaction (such as in (Saĭto, Otšuka and Furuya, 1983; Allen *et al.*, 1987; Roki *et al.*, 2008; Miradji F.; et al., 2019; Nakajima *et al.*, 2019). The formation of Cs-(Fe)-Si-O in the deeper parts seems to

occur due to the growth of the oxide layers especially due to the migration of Fe to form Fe_2O_3 as an outer oxide layer.

5.2.1.2.2 Post-soaked SS 321

Quantitative EDS of SS 321 treated at 300 °C and 450 °C indicates the amount of Cs retention is very small, even under the detection limit of quantitative EDS measurement. However, some small particles adhere to these specimens. SEM/EDS mapping and point analysis as shown in Figure 5.11 show these particles are strongly related to Cs-Al-Ti-O. Besides Al and Ti, some Cs particles are also observed to be related to Si.

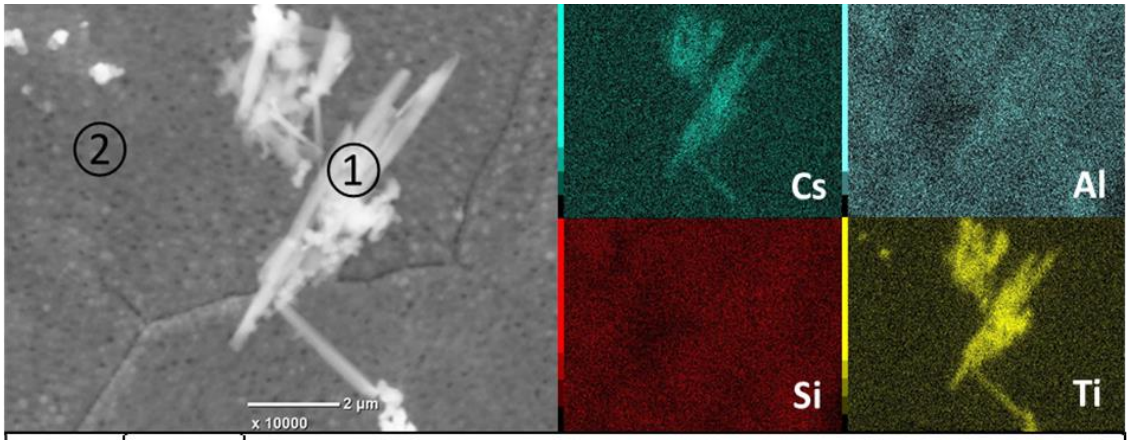

at.%	Point	Cs	Al	Si	Ti	Fe
SS 321	①	5.16±0.26	1.46±0.073	1.16±0.06	7.76±0.38	36.54±1.83
	②	0.39±0.12	0.92±0.046	1.16±0.06	2.62±0.13	56.17±2.81

Figure 5.11. Tiny Al- and Ti-enriched Cs particles retain on the surface of post-soaked SS 321 treated at 450 °C.

Tiny particles as observed from specimens treated at lower temperatures cannot be seen from specimens treated at 600 °C. From specimens treated at 600 and 750 °C, the formation of Cs compounds is spread on the surface but still shows the same tendency, which overlaps with Al, Ti, and some also related to Si.

At 900 °C, the formation of Cs compounds is mainly associated with Si, although some still show a tendency to overlap with Al and Ti as shown in Figure 5.12. Si-enriched Cs compounds spread mainly in the formation of iron oxides but are relatively poor in the formation of Ni-rich regions. This can be understood because Cs tend to be inert with Ni

but are still able to make such kinds of compounds with Fe. However, the formation of Cs compounds is not consistent with lumpy objects which are strongly related to iron oxides. The small number of Cs-Si compounds on the surface is also overlapping with Al but does not form distinct clusters. Nevertheless, since the formation of the oxide film is relatively thick, it is necessary to confirm the presence of Cs entrapped inside the oxide film.

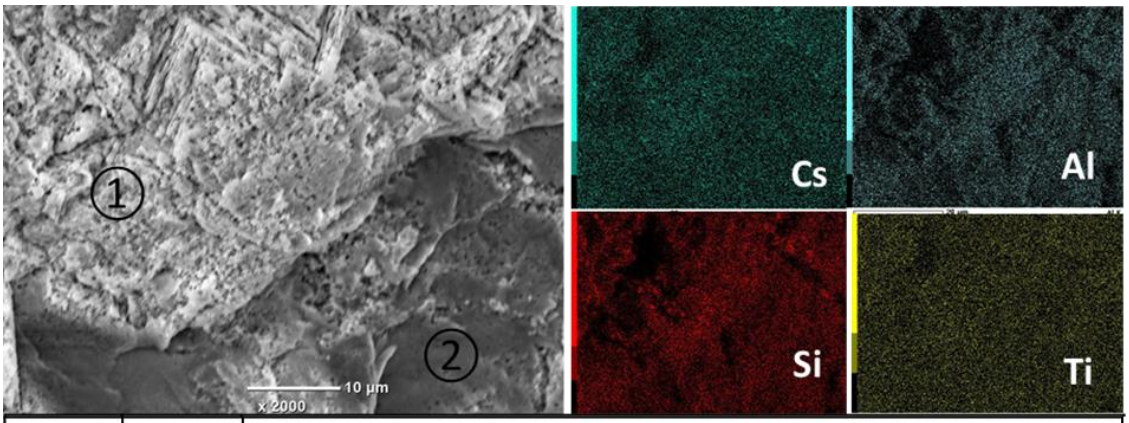

at.%	Point	Cs	Al	Si	Ti	Fe
SS 321	①	2.12±0.11	1.15±0.06	2.04±0.10	0.08±0.01	35.98±1.80
	②	0.35±0.02	0.44±0.02	0.59±0.03	0.05±0.01	16.88±0.84

Figure 5.12. Formation of Cs-Al-Ti-Si compounds in post-soaked SS 321 treated at 900 °C.

Cross-sectional analysis as shown in Figure 5.13 also shows a similar tendency. Cs compounds mainly overlap with Ti, with some parts with Si. However, point analysis indicates the amount of Ti on the outermost layer near the surface is relatively small compared with the deeper parts. Because of that, Figures 5.12 and 5.13 suggest that the formation of Cs compounds on the surface is mainly related to Si while Ti enrichment should be in the deeper parts. By taking a closer look at Figure 5.13, the formation of Si-enriched Cs compounds also can be observed laid in the outer layer as happened in SS 304. There is no indication that Si-enriched Cs elements are in the Cr-rich regions and/or in the base materials. However, based on the EDS signal intensity, the amount of Cs in the oxide film of SS 321 is very limited.

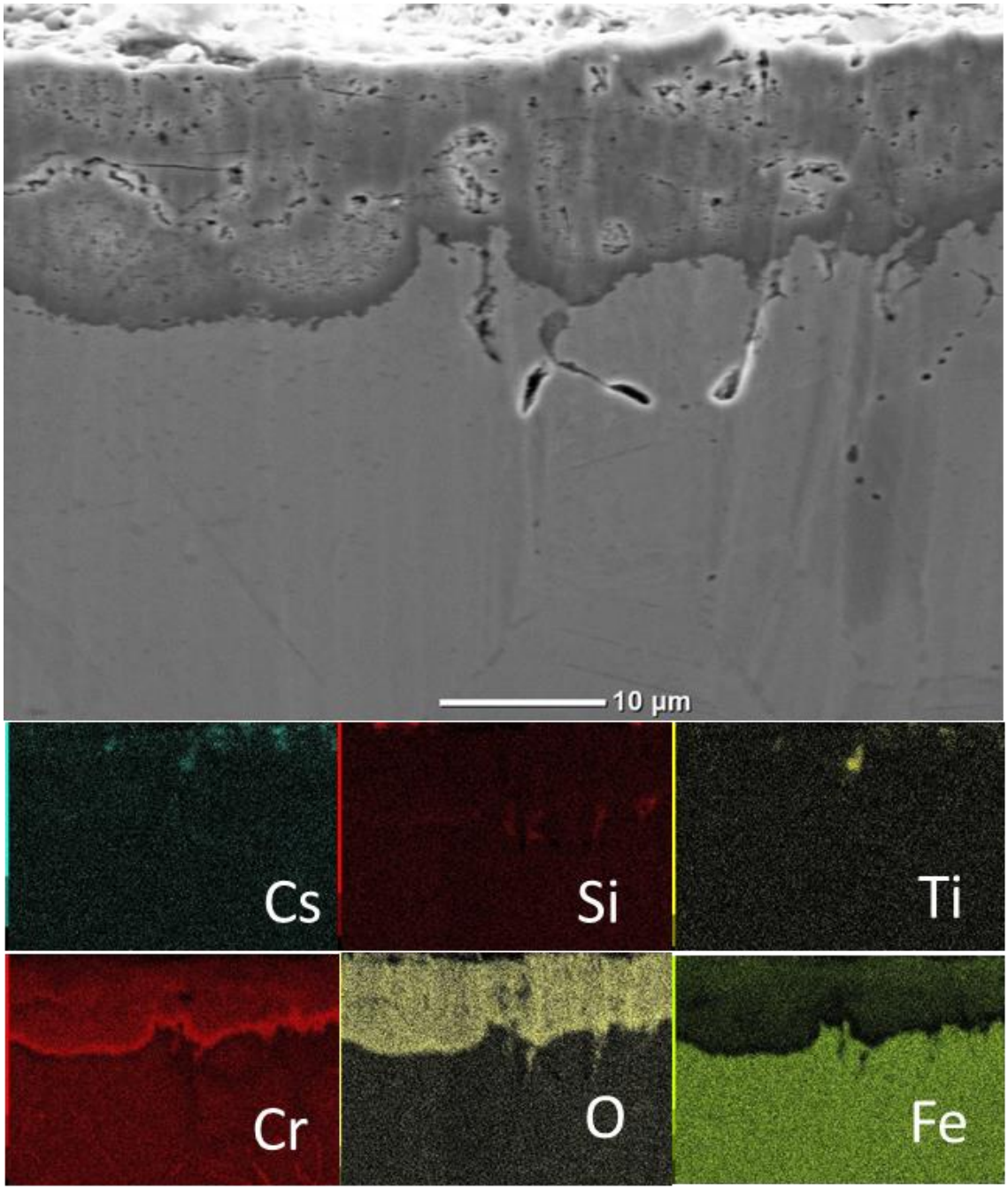

Figure 5.13. Formation of Ti- and/or Si-enriched Cs compounds in oxide film of post-soaked SS 321 treated at 900 °C.

More detailed elemental distribution can be observed from specimens treated at 1050 °C. Although this condition cannot be compared with the specimens treated at lower temperatures due to a short liquid-solid reaction and should not happen in the real environment as a liquid-solid reaction, however, it could be used to interpolate and extend the oxidation growth and Cs chemisorption observation.

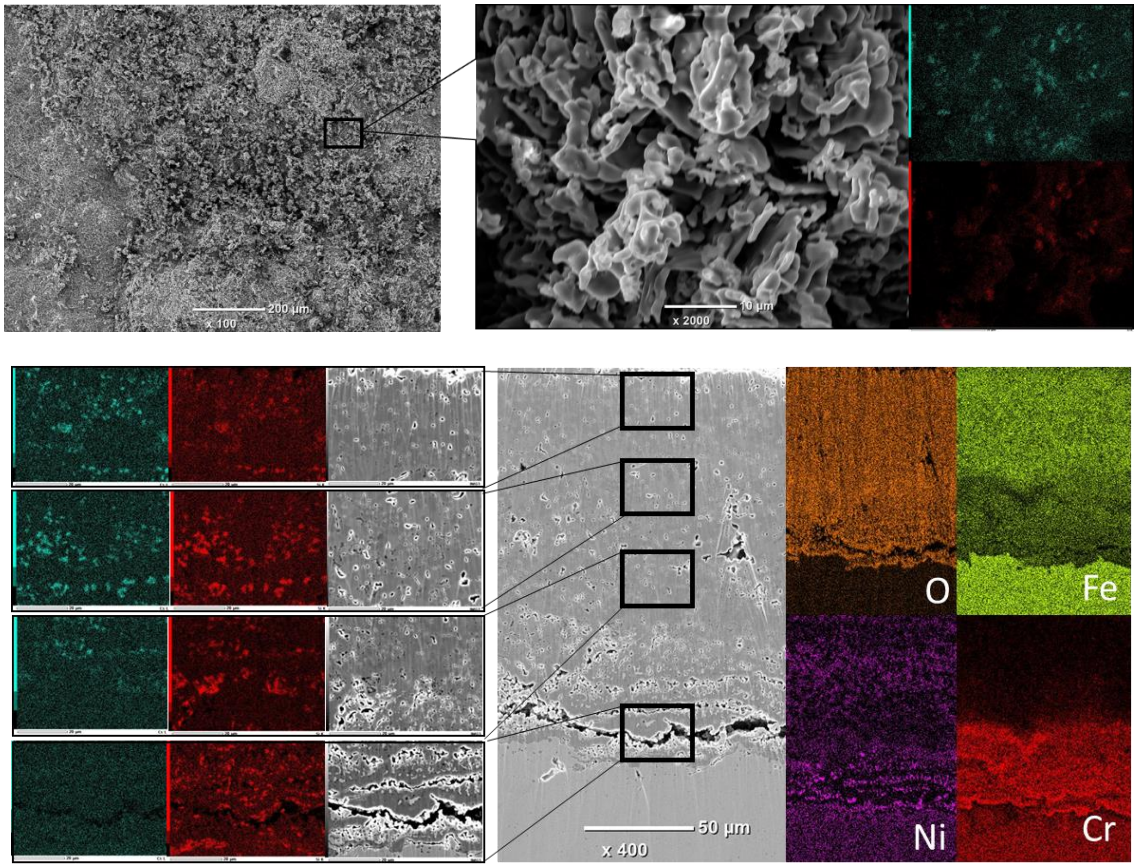

Figure 5.14. Si-enriched Cs compounds distribution in oxide film of post-soaked SS 321 treated at 1050 °C.

As shown in Figure 5.14, the surface and cross-sectional SEM/EDS observations show that Si-enriched Cs elements are distributed alongside the outer oxide layer. Although Si formation is spread in the Cr-rich layer as the inner layer as well as fills the cracks just below the inner layer, however, no indication shows Si-enriched Cs compounds as observed in the outer layer. This provides clear evidence that Cs elements are not diffused through Cr-rich formation. In the outermost oxide layer, Cs can be observed mainly overlap with Si and Al without any relationship with Ti. EDS signal intensity of Cs from SS 321 compared with SS 304 is also smaller. That indicates lesser Cs are chemisorbed onto SS 321 compared with SS 304.

5.2.1.2.3 Post-soaked Inconel 600

As indicated in Figure 5.15, small Cs particles containing Si, Al, and a small amount of Ti are stuck on the surface of Inconel 600. Point analysis by comparing between inner and outer of the object of interest shows Cs elements are strongly related to Al and Si

with atomic ratios around 1: 1.1: 1. While the amount of Ti on the target of interest is only 0.11 at. % higher compared with the surroundings. It should be an indication that the chemisorbed Cs compounds are mainly related to Cs-Al-Si-O compounds.

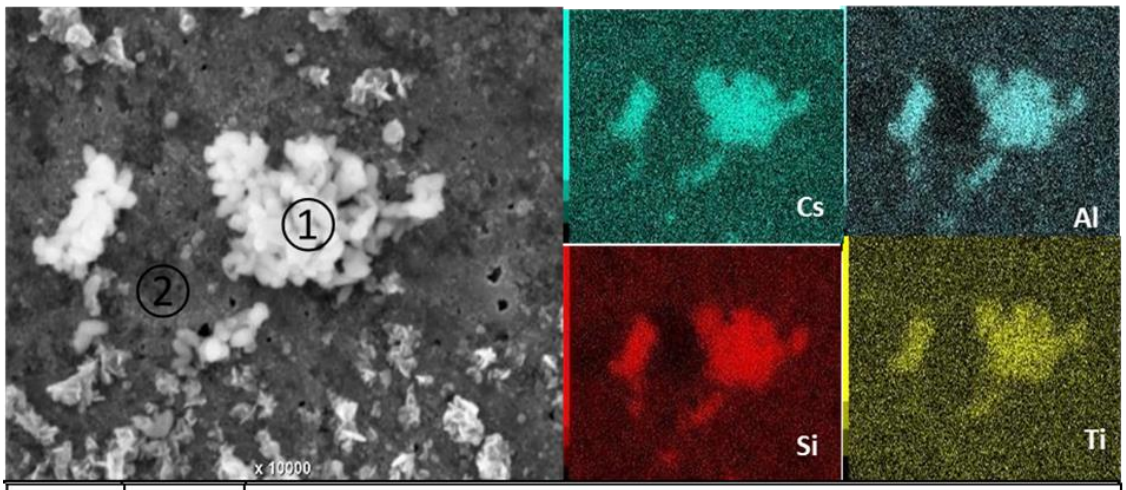

at.%	Point	Cs	Al	Si	Ti	Fe
In 600	①	9.24±0.46	10.34±0.52	9.12±0.46	0.33±0.02	1.26±0.02
	②	1.08±0.05	1.30±0.07	0.74±0.04	0.22±0.01	3.39±0.17

Figure 5.15. Small Cs-Al-Ti-Si-O formations are retained on the surface of Inconel 600 treated at 450 °C.

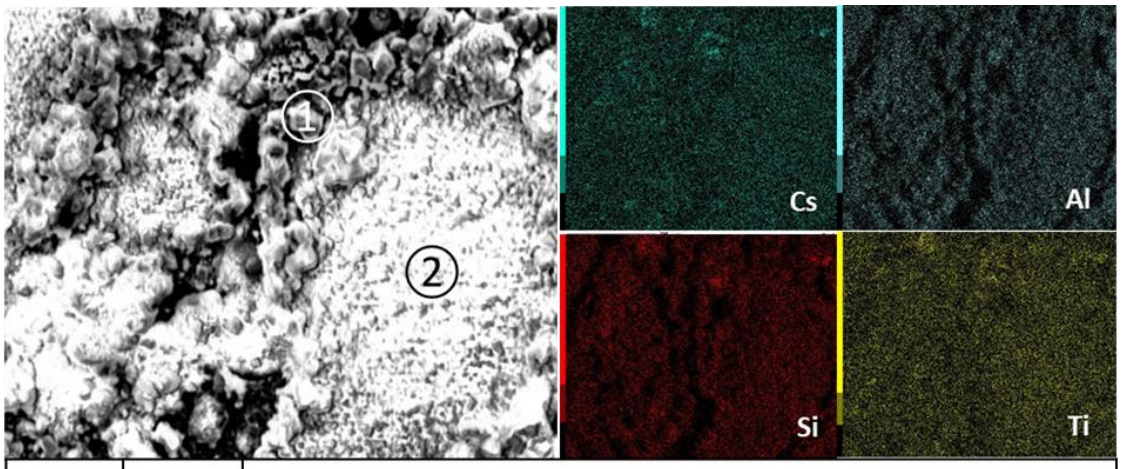

at.%	Point	Cs	Al	Si	Ti	Fe
In 600	①	3.44±0.17	2.51±0.13	2.86±0.13	1.25±0.06	8.34±0.42
	②	0.36±0.02	1.02±0.05	0.49±0.02	0.86±0.04	10.96±0.55

Figure 5.16. Measly amounts of Si- and Ti-enriched Cs particles exist on the surface of Inconel 600 treated at 900 °C.

Although in general, the remaining Cs on the surface of the Inconel 600 specimen treated at 600 °C is slightly higher compared with the specimens treated at 300 & 450 °C, however, Cs particles that are stuck on the surface cannot be observed. Cs spread on the surface more uniformly but show overlapping with Al, Si, and Ti. That trend still can be observed from specimens treated at 750 °C as well as from specimens treated at 900 °C, as shown in Figure 5.16. However, same with SS 304 and SS 321, Cs elements are mainly related to Si rather than Al.

Cross-sectional SEM/EDS observation of specimens treated at 900 °C as shown in Figure 5.17 indicates the overlapping between Cs with Al, Ti, and Si around the surface and crack areas. The formation of Cs compounds around the cracks seems to correlate with the crack of the pre-oxide film before being exposed to the CsOH precursor. These cracks may make Cs easier to enter and interact with Ti. However, this Cs trapping mechanism does not make a significant contribution to the Cs chemisorption. That is because Inconel 600 has a relatively thin oxide layer with a very limited amount of Ti as well as Al and Si.

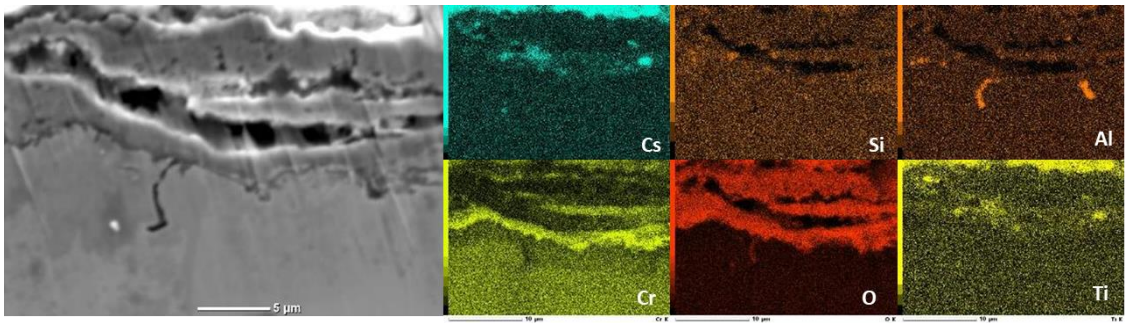

Figure 5.17. Ti-enriched Cs compounds are in cracks beside the surface of Inconel 600 treated at 900 °C.

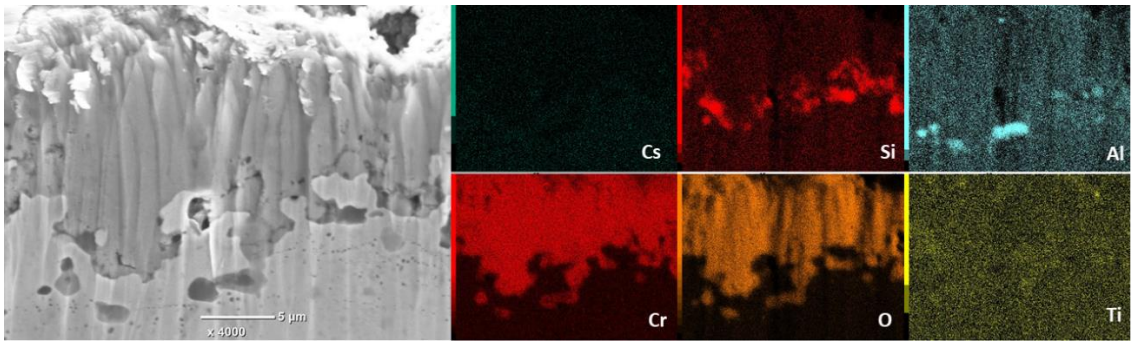

Figure 5.18. Cs elements almost completely disappeared from Inconel 600 treated at 1050 °C.

The formation of Cs compounds is almost undetectable from both surface and cross-sectional SEM/EDS observation of the specimens treated at 1050 °C. Although EDS mapping as shown in Figure 5.18 shows a color gradient for the Cs mapping, however, Cs-related EDS signals could not be detected, which indicates that Cs elements are under the detection limit of EDS. The formation of Al and Ti on the surface that had been observed from lower temperatures treatment is also undetectable. Cs-Al-Ti-O compounds must be largely evaporated when the specimen is treated at 1050 °C.

5.2.1.2.4 Post-soaked X-750

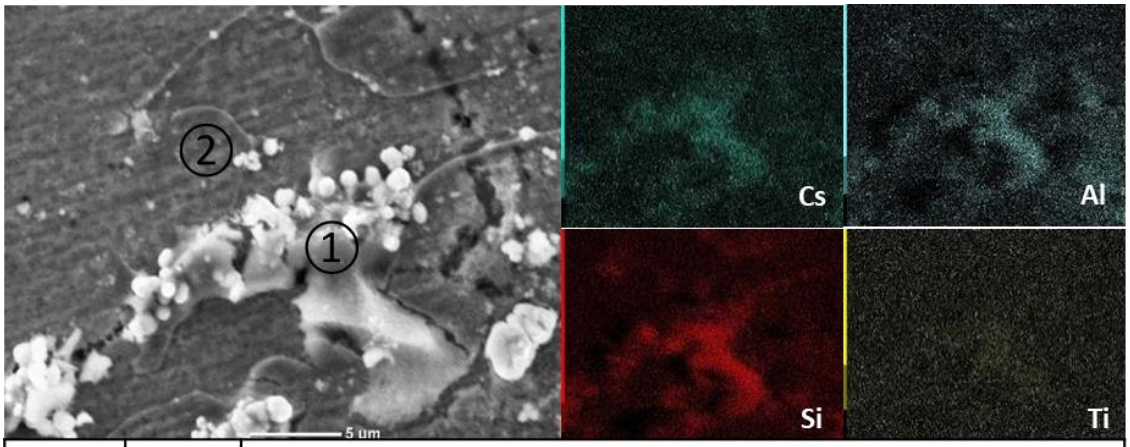

at.%	Point	Cs	Al	Si	Ti	Fe
X-750	①	3.99 ±0.20	4.46 ±0.26	0.14 ±0.08	18.18 ±0.08	3.23±0.16
	②	0.96±0.05	1.56±0.08	0.05±0.12	0.81±0.04	3.84±0.19

Figure 5.19. Cs-Al-Ti-Si-O particles on the surface of X-750 specimen treated at 450 °C.

X-750 shows some Cs retention similarities compared with Inconel 600. Some small Cs particles can be observed from both oxidized and unoxidized specimens treated at 300 and 450 °C. As shown in Figure 5.19, the observed particles indicate the formation of Cs-Al-Ti-Si-O compounds. Based on point analysis, the average atomic ratio between Cs, Al, Si, and Ti on these particles is around 2.80/3.13/0.10/12.76.

Overlapping between Cs, Al, Ti, and Si are still present in specimens treated at 600 and 750 °C. However, Cs compounds spread uniformly alongside the surface. Ti-enriched Cs compounds can be observed clearly from specimens treated at 900 °C as shown in Figure 5.20. Needle-like Cs-Ti-O compounds are formed on the surface, whereas Al and Si appear to form underneath.

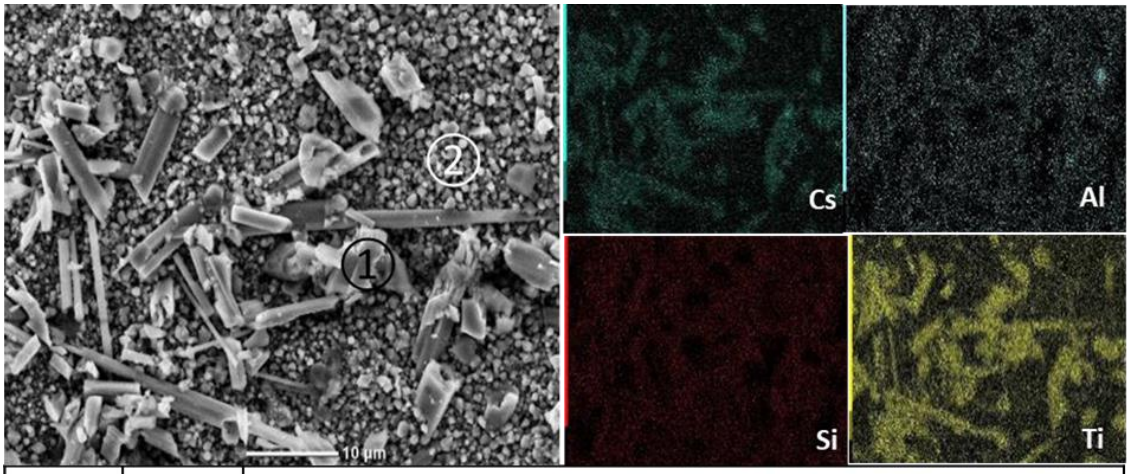

at.%	Point	Cs	Al	Si	Ti	Fe
X-750	①	4.54±0.23	0.90±0.05	0.09±0.01	21.12±1.06	1.09±0.05
	②	0.22±0.01	1.61±0.08	0.12±0.01	9.43±0.47	4.43±0.22

Figure 5.20. Needle-like Ti-enriched Cs compounds are chemisorbed on the surface of an X-750 specimen treated at 900 °C.

Cross-sectional SEM/EDS observation of post-soaked X-750 treated at 900 °C as shown in Figure 5.21 indicates Cs compounds are only chemisorbed in the outer layer. Although Si- and Al-enriched Cs compounds are expected from some areas, however, most Cs elements are overlapped with Ti confirming the formation of Cs-Ti-O compounds as identified from surface observation. The tendency of Cs to be reacted with Ti is related to the thick TiO_2 layer on the surface of X-750 while the concentration of Si is relatively low.

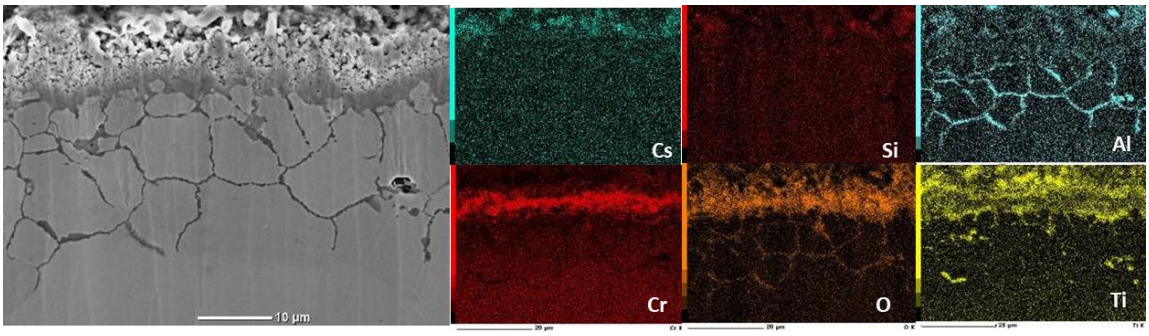

Figure 5.21. Chemisorbed Cs elements are strongly related to Ti on X-750 specimens treated at 900 °C.

As shown in Figure 5.22, SEM/EDS mapping of Cs still shows color gradients indicating overlap with Si. Even so, the intensity of the Cs-associated signal is very small.

So, it can be said the amount of Cs which are chemisorbed in the X-750 specimen treated at 1050 °C is negligible.

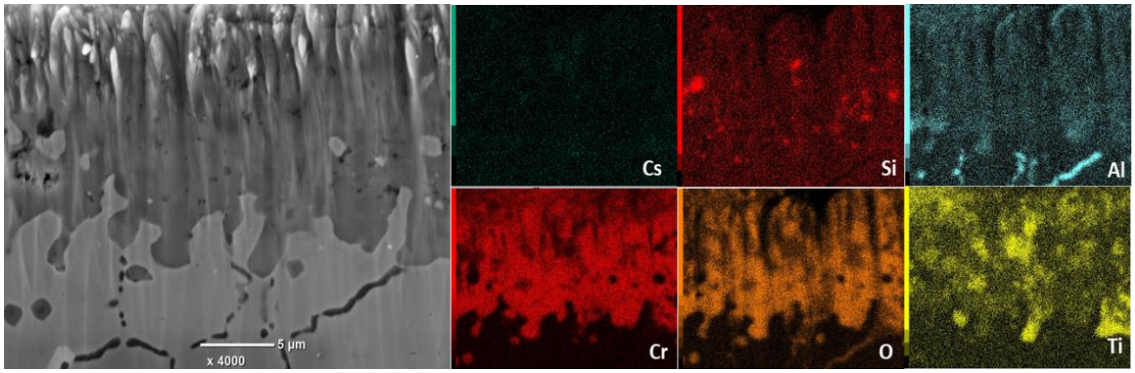

Figure 5.22. Cs retention in X-750 specimens treated at 1050 °C is negligible.

5.2.2 Prediction of Chemisorbed Cs-Al-Ti-Si-O Compounds

5.2.2.1 Cs Compounds Prediction in SS 304

As shown in Figure 5.23, the XRD analysis of simulated Cs compounds in SS 304 indicates some possibilities. The most possible formation which can be formed at all temperature treatments is $CsAlSiO_4$ which matches with ICDD card numbers 00-029-0405 and 00-047-0471. $CsAlSiO_4$ with $Pna2_1$ unit cells especially at 2θ = 26.9°, 27.7°, 29.9°, and 32.8° can be observed from all temperature treatments. Peaks that are strongly related to $CsAlSiO_4$ with Ia3d unit cells are formed from specimens treated at 900 °C and 1050 °C, especially at 2θ = 24.6°, 26.3°, 30.9°, 37.5°. Peaks that are strongly related to $CsAlO_2$ with ICDD card number 01-074-2291 appear at all temperature treatments especially can be identified at 2θ = 31.6°, 36.8°, and 44.7°. However, $CsAlO_2$-related peaks are small showing it must be available in limited quantities. Several other peaks at 2θ = 28.8°, 31.5°, and 34.2° also appear from specimens treated at 300 – 600 °C. These peaks are related to $Cs_2Al(OH)(SiO_4)_2$ with ICDD card number 00-037-0063. α-Al_2O_3-related peaks with ICDD card number 01-071-1125 also exist at 2θ = 25.7°, 35.3°, 38.0°, and 43.5°, indicating a part of the α-Al_2O_3 precursor is not well-reacted.

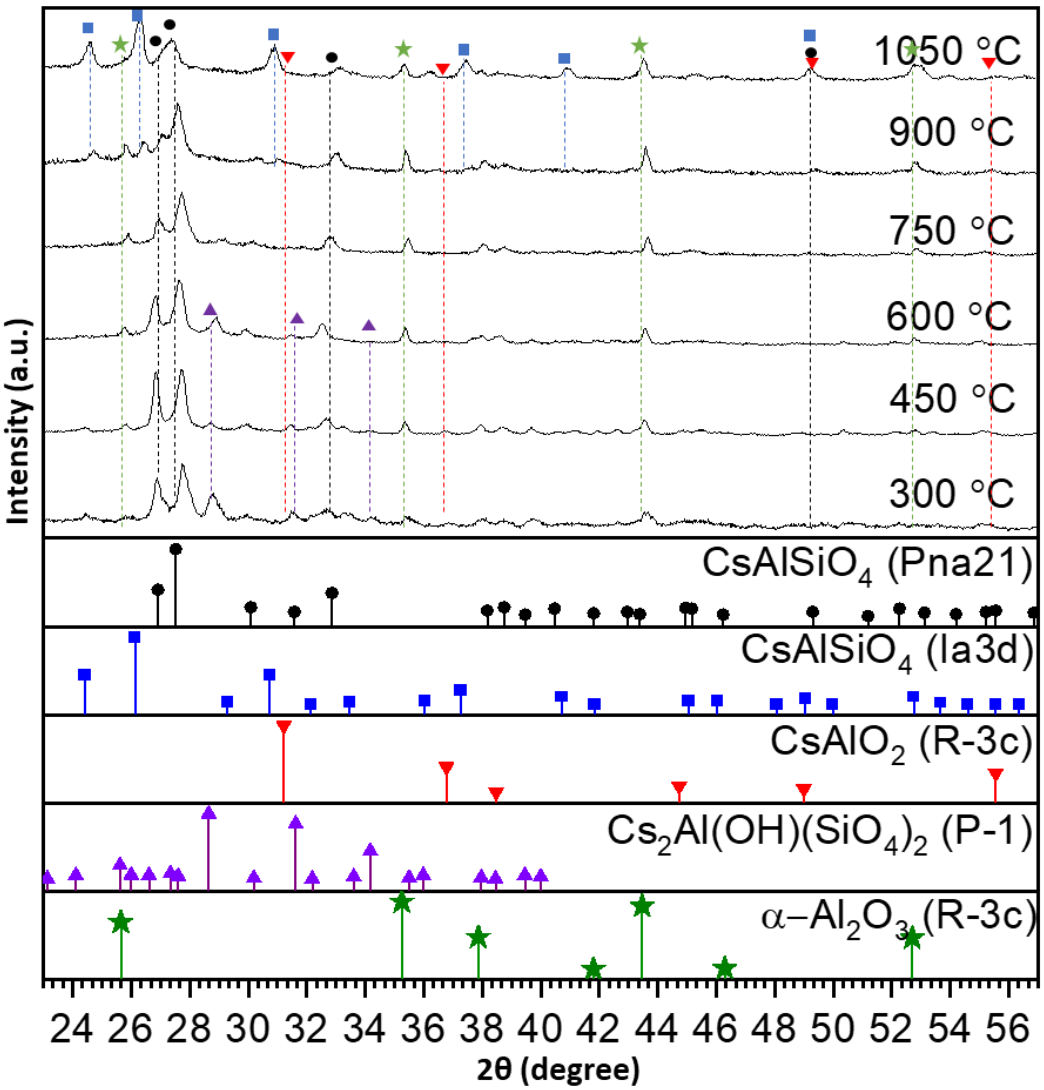

Figure 5.23. Identification of simulated chemisorbed Cs compounds in SS 304 indicates most of them are related to $CsAlSiO_4$ and excess Al_2O_3 precursor. The rest peaks may also correlate with $CsAlO_2$ and $Cs_2Al(OH)(SiO_4)_2$, especially at lower temperatures.

5.2.2.2 Cs Compounds Prediction in SS 321

Like the simulated Cs compounds in SS 304, Cs compounds in SS 321 are also mainly predicted as $CsAlSiO_4$. As shown in Figure 5.24, $CsAlSiO_4$ is identified in the same position and with two types of the unit cell as observed from simulated Cs compounds in SS 304. $Cs_2Al(OH)(SiO_4)_2$ -related peaks are also expected to be formed at the same temperature treatment. However, due to the existence of Ti, some peak variation existed from simulated Cs compounds in SS 321. The peaks especially at 2θ = 25.6°, 26.8°, and 31.0° are strongly related to $CsAlTiO_4$ with ICDD card number 01-079-0750. While from

specimens treated at 300 and 450 °C, especially at 2θ = 24.3°, 27.7°, 28.2°, 31.5°, and 42.6° related to the $Cs_2TiO_4{\cdot}H_2O$ with ICDD card number 00-019-0315.

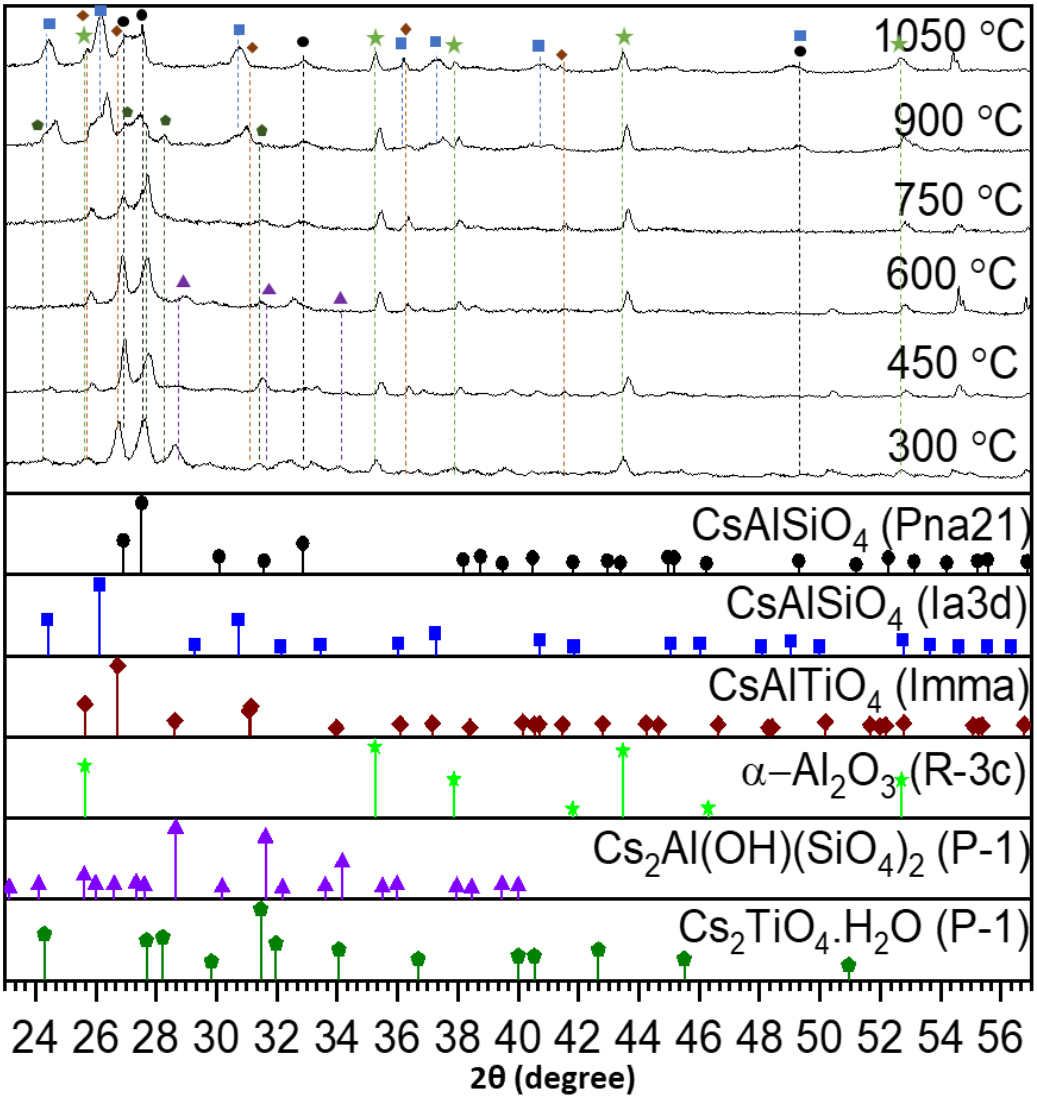

Figure 5.24. Identification of simulated chemisorbed Cs compounds in SS 321 shows the existence of $CsAlSiO_4$, $CsAlTiO_4$, and excess Al_2O_3 precursors at all temperature treatments. Other peaks may also relate to $Cs_2TiO_4{\cdot}H_2O$ and $Cs_2Al(OH)(SiO_4)_2$, particularly at 300-900 °C and 300-600 °C temperature treatment, respectively.

5.2.2.3 Cs Compounds Prediction in Inconel 600

Simulated Cs compounds in Inconel 600 consisted of the same elements as in SS 321 with slight differences. Due to that composition, XRD analysis as shown in Figure 5.25 indicates the formation of a similar compound as in SS 321 which is mainly related to

$CsAlSiO_4$, $CsAlTiO_4$, $Cs_2Al(OH)(SiO_4)_2$ and exceeds Al_2O_3 precursor. The topmost highest peaks in Inconel 600 are also consistent and closely related to $CsAlSiO_4$ which has two types of the different unit cells. Both $CsAlSiO_4$ and $CsAlTiO_4$ are expected at all temperature treatments. At 300 – 600 °C, strong peaks related to $Cs_2Al(OH)(SiO_4)_2$ can be observed. While some rest peaks may be related to $Cs_2Si_2O_5$. $Cs_2Si_2O_5$ is already considered to be one of the important species for Cs chemisorption onto stainless steel (Kobata *et al.*, 2018). Because of that, chemisorbed Cs particles on Inconel 600 must be mainly related to $CsAlSiO_4$, and the rest may relate to $Cs_2Al(OH)(SiO_4)_2$ and $CsAlTiO_4$.

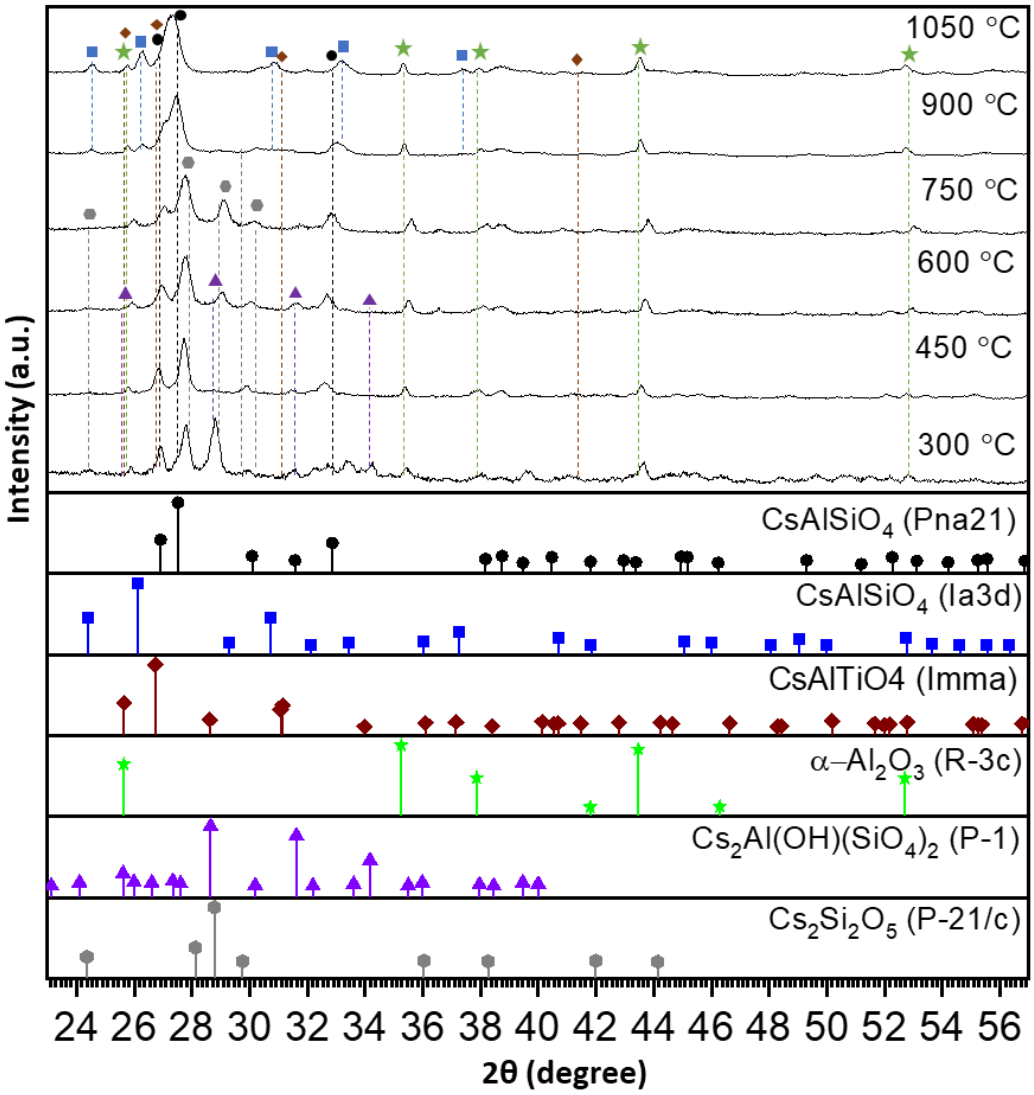

Figure 5.25. Simulated Cs compounds in Inconel 600 indicate most of them are $CsAlSiO_4$, $CsAlTiO_4$, and excess Al_2O_3 precursor. Peaks relate to $Cs_2Si_2O_5$, and $Cs_2Al(OH)(SiO_4)_2$ are also presented from some temperature treatments.

5.2.2.4 Cs Compounds Prediction in X-750

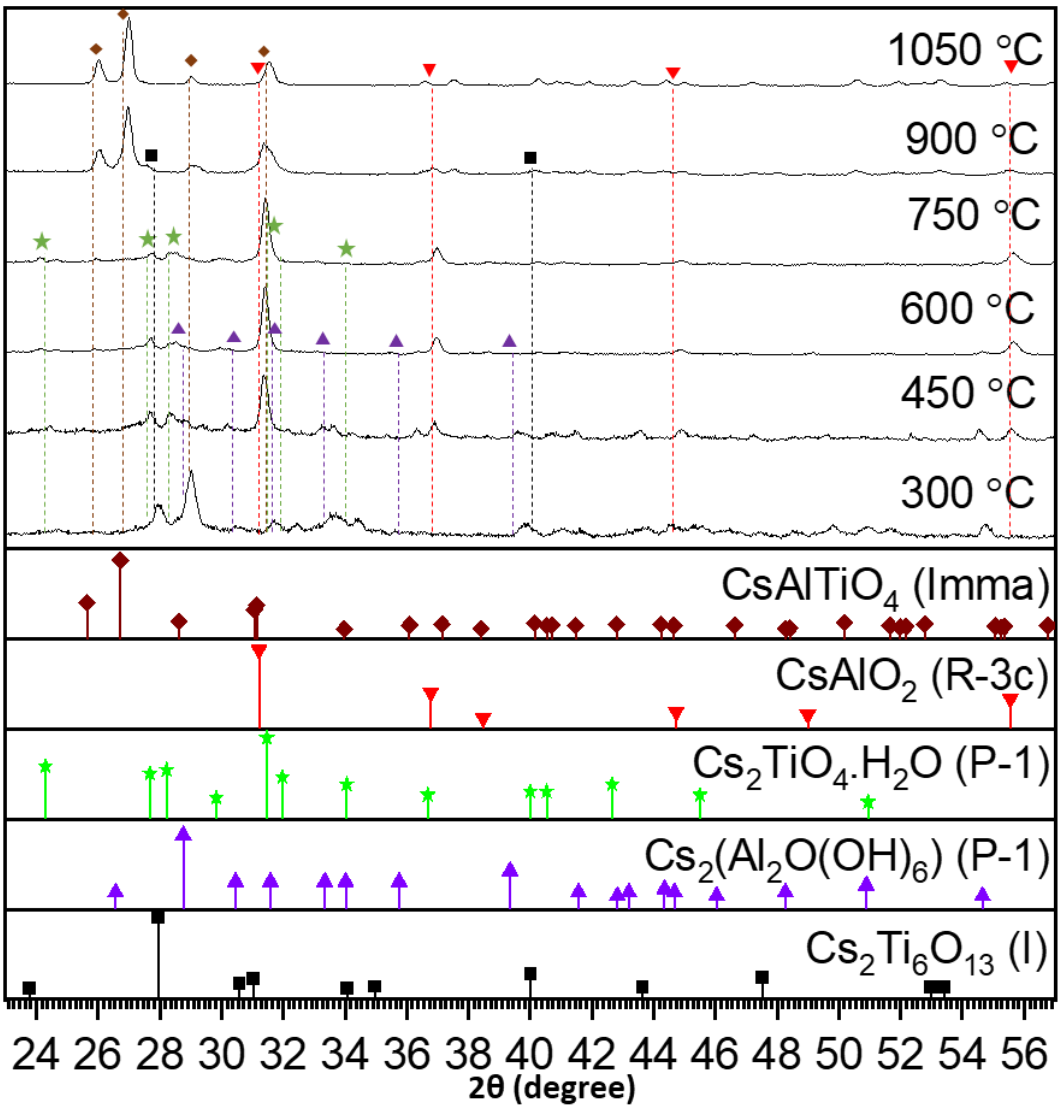

Figure 5.26. Simulated Cs compounds in X-750 indicate the existence of a relatively large amount of $CsAlTiO_4$ and $CsAlO_2$. While the rest peaks may also relate to $Cs_2Ti_6O_{13}$, $Cs_2TiO_4{\cdot}H_2O$, and $Cs_2(Al_2O(OH_6))$ at respective temperatures.

Although consists of the same elemental composition compared with Inconel 600, simulated Cs compounds in X-750 are poor of Si, which is only about a tenth. Si deficiency causes the XRD patterns from simulated Cs particles in X-750 to be different. As shown in Figure 5.26, instead of forming $CsAlSiO_4$ as can be observed from the other materials, the peaks of simulated Cs compounds in X-750 are mainly related to $CsAlTiO_4$, $CsAlO_2$, $Cs_2Ti_6O_{13}$, $Cs_2TiO_4{\cdot}H_2O$, and $Cs_2(Al_2O(OH_6))$. $CsAlTiO_4$- and $CsAlO_2$- related peaks can be observed at 2θ = 25.6°, 26.8°, and 31.0° as well as at 2θ = 31.6°, 36.8°, and

44.7° appear from all temperature treatment. $Cs_2Ti_6O_{13}$-related peaks which match with ICDD card 00-038-0170 can be seen from specimens treated at 300 – 900 °C, especially from 2θ = 27.7°, 40.1°, and 47.4°. While $Cs_2TiO_4{\cdot}H_2O$- and $Cs_2(Al_2O(OH_6))$-related peaks which match with ICDD card numbers 00-019-0315 and 00-036-0465, respectively are mainly appeared from specimens treated at 300 and 400 °C. $Cs_2TiO_4{\cdot}H_2O$-related peaks particularly at 2θ = 24.3°, 27.7°, 28.2°, 31.5° and 42.6°. While $Cs_2(Al_2O(OH_6))$-related peaks can be observed from 2θ = 28.9°, 30.3°, 31.6°, 33.3°, and 39.6°.

5.3 Discussion

5.3.1 Pre-oxidation and the Reactant Availability

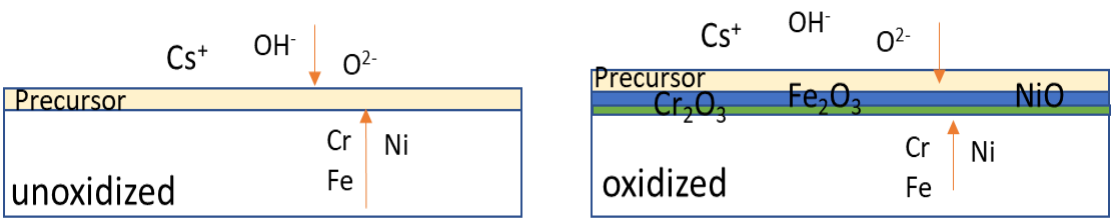

Figure 5.27. Pre-oxidation contributes to the availability of the reactants which furthermore affect the Cs retention.

Formation of pre-oxide film on the surface of specimens has a direct correlation with the Cs chemisorption. The amount of Cs on both unoxidized and oxidized specimens is almost similar when the oxide film is insignificant. However, the amount of Cs can be observed to become higher in oxidized specimens rather than in unoxidized specimens. The reduction of CsOH precursors due to evaporation must be the same when several specimens are treated at the same temperatures. However, variation in the quantity and quality of the formed compound of the pre-oxide film contributes to the different chemical reactions between unoxidized and oxidized specimens.

As illustrated in Figure 5.27, $CsOH{\cdot}H_2O$ precursor interaction starting points between unoxidized, and oxidized specimens are different. In unoxidized specimens, $CsOH{\cdot}H_2O$ interacts directly with the surface of alloys. While in oxidized specimens, $CsOH{\cdot}H_2O$ interacts with the formation of oxide films. Kinetically, during these

interactions' mechanisms, $CsOH{\cdot}H_2O$ must be decomposed and ionized to be Cs^+, OH^-, and H_2O. Besides the oxidation of material's elements (M) caused by the oxygen in the air by following $\frac{2\alpha}{\beta}M + O_2 = \frac{2}{\beta}M_\alpha O_\beta$ (Noguchi and Yakuwa, 2016; Yakuwa and Noguchi, 2017). OH^- ions may also accelerate the oxidation mechanism by following $M + \vartheta OH^- = M^{\vartheta+} + \vartheta O^{2-} + \frac{\vartheta}{2}H_2$ reaction (Chang *et al.*, 1992). As the positive ions, Cs^+ cannot reacts directly with $M^{\vartheta+}$, but may react with negative ions in the form of $M_\alpha O_\beta{}^{\gamma-}$. $M_\alpha O_\beta{}^{\gamma-}$ ions such as $Fe_2O_4^{2-}$, FeO_2^-, and $Cr_2O_4^{2-}$ which can be formed after the oxidation process occurs. Due to the availability of oxide film on oxidized specimens, the Cs^+ reaction may happen immediately, while in unoxidized specimens, the reaction must be started from the oxidation mechanism. By considering CsOH reduction on both specimens due to the same evaporation rate, as well as higher availability of $M_\alpha O_\beta{}^{\gamma-}$ reactants in oxidized specimens, then the newly formed Cs-*M*-O compounds in oxidized specimens should be higher. The higher formation of Cs-*M*-O compounds furthermore increases the possibility of Cs being chemisorbed in the specimens.

5.3.2 Elemental Composition and Oxide-film Thickness

Oxide compounds of some solute elements, especially Al, Ti, and Si contribute to the Cs chemisorption. High amount of chemisorbed Cs compounds in oxidized Inconel 600 and X-750 specimens treated at 450 ^oC is related to Al, Ti, and Si by forming such kinds of Cs-Al-Ti-Si-O compounds which are identified mainly as $CsAlSiO_4$, $CsAlTiO_4$, $CsAlO_2$, cesium titanate and the rest could be related to some of their hydrates. Both Inconel 600 and X-750 have higher solutes Al and Ti, while limited Al on SS 304 only can be expected as an impurity. Thermodynamically, as can be explained by using Ellingham's diagrams, Al and Ti are easy to be oxidized and migrate to the surface (Wei gao, 2008, p. 335; Stratton, 2013). Cs elements that may chemically react with Al, O, including Si, and Ti in the case of Inconel 600 and X-750 then physically and/or chemically stick on the surface. Cs amount on Inconel 600 and X-750 is relatively smaller compared with that in SS 304 and SS 321 when treated at 600 ^oC. The smaller amount of Cs in Inconel 600 and X-750 is caused by its oxide film formation. The outer oxide layer of SS 304, SS 321, Inconel 600, and X-750 consist of different compounds and concentrations. The outer

oxide layers of Inconel 600 and X-750 are relatively thin and dominated by NiO with the concentration increase in line with the annealing temperature. Cs element has a low tendency to react with Ni making its retention with Inconel 600 and X-750 become lower. In contrast, a higher amount of Cs in SS 304 and SS 321 is related to the silicon oxides-rich formation by forming well-chemisorbed Cs-Si-O compounds in the oxide layer.

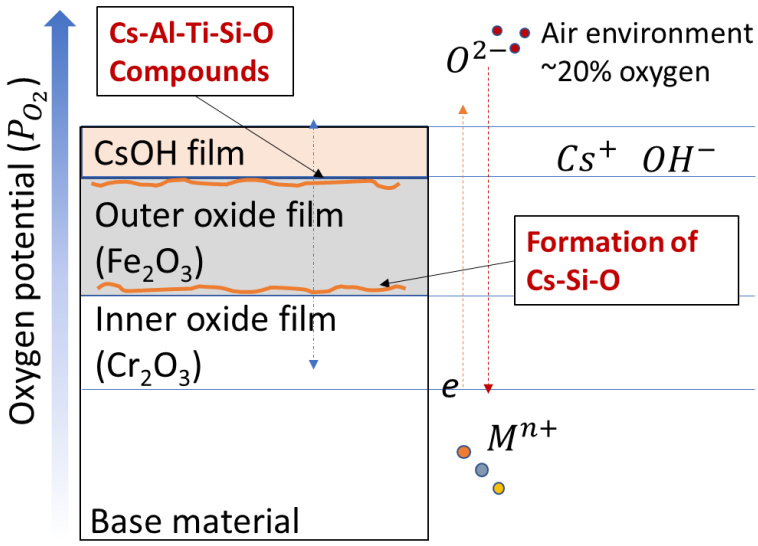

Figure 5.28. Oxidation growth and chemisorption mechanism happen together during the CsOH interactions.

As the Fe-based alloy, SS 304 oxide film grows faster compared with Ni-based alloys due to the characteristic of Fe that is thermodynamically less stable than Ni. Cs may firstly be retained on the surface of the existing oxide film and then overlapped by the growth of the outer oxide layer as illustrated in Figure 5.28. This mechanism must be the main reason why Cs- Si-O can be observed between the inner and outer oxide layer. Cs- Si-O cannot be found on or under the inner oxide layer since Cs diffusion throughout chromium oxides, and base material is negligible. The relatively thick outer oxide layer of SS 304 with Cs elements spread to ~10 μm depth or more, while electron penetration during EDS analysis is only ~300 nm also become a reason why the detected amount of Cs at 900 °C is relatively small although many spots of Cs can be found on the oxide layers. Actual Cs retention on the SS 304 treated at 900 °C and 1050 °C must be higher than that being measured.

Lower amount of chemisorbed Cs in the post-soaked SS 321 than in SS 304 when

treated at 300 °C and 450 °C is attributable to Ti. Oxide film of SS 304 is thicker than that of SS 321 with a higher amount of Al. Ti contributes to chromium oxide stabilization in SS 321. Moreover, stable chromium oxides reduce element migration, particularly that of Al, which further contributes to the lower amount of chemisorbed Al-enriched Cs compounds. At higher temperatures, the migration of SS 321 elements is slower than that of SS 304 which makes its oxide film thinner. However, the amounts of Cs, Al, and Si in SS 321 are consistently higher. The higher amounts of these elements are associated with the different oxidation characteristics of SS 304 and SS 321. The buried Si-enriched Cs compounds between the inner and outer layers of SS 304 are induced by the overlap of iron oxide arising from the fast growth of the outer layer. This mechanism furthermore results in most Cs compounds being overlapped by the relatively thick outer layer which is mainly composed of iron oxides. On the other side, the outer oxide layer growth of SS 321 is much slower compared with SS 304. This causes most of the Cs to remain in the relatively thinner outer oxide layer. Consequently, the Cs-related EDS signal intensity of SS 321 appeared higher than that of SS 304, although the cross-sectional observation shows the opposite result. The stabilization of chromium oxide by Ti decelerates the oxide film growth, which further limits the reaction rate between the CsOH precursor and oxide film. Owing to the slower reaction rate, the formed Cs compounds in SS 321—particularly those bound to Si—become fewer than those formed in SS 304.

The oxide layer of Inconel 600 and X-750 is well-maintained even at elevated temperatures, especially with relatively thick chromium oxides and the thin outer oxide layer. The thin outer oxide layer of Inconel 600 and X-750 furthermore contributes to the relatively small amount of Cs chemisorption. Inconel 600 also tends to form explosion-like cracks containing titanium oxides. Titanium oxides may react with Cs, which furthermore form cesium titanate that can be found trapped in the cracks beside the surface. Nevertheless, those cracks insignificantly affect the Cs retention since they consist of a very small amount of Ti. The high amount of Ti and Al in X-750 suppresses the oxygen diffusion and fills the formed cracks in the oxides, as also observed by (Warlimont, 2003). The relatively large amount of titanium and aluminum oxides furthermore involve the formation of Cs-Al-Ti-O compounds which make larger Cs to be chemisorbed. However, Cs chemisorption only occurs on/in the relatively thin outer oxide

layer and cannot happen on or below the inner oxide layer. Even at 1050 °C, when the migration of elements to the surface is going faster, oxygen can diffuse deeper forming Al-Ti-O grain boundaries below chromium oxides protective layer, but that layer is still well-maintained and Cs ions including their formed compounds on the outer layer are not capable to diffuse throughout it. The migration of Fe and Ni including the other elements to form the outer oxide layer is also much more limited compared with stainless steel. That condition makes the Cs compound's overlapping mechanism by forming the outer oxide layer becomes limited.

5.3.3 Cs-Al-Ti-Si-O Chemical Systems

The formation of compounds from observed Cs particles varies depending on the material and temperature treatment. Although variation exists, there are several dominant compounds present. Except for the simulated Cs compound of X-750, $CsAlSiO_4$ dominates the compound formation of specimens at all temperature treatments. However, there are pattern differences in $CsAlSiO_4$ between specimens treated at lower temperatures with it at 900 – 1050 °C. $CsAlSiO_4$ pattern of specimens treated at lower temperatures match with ICDD 00-029-0405 which has $Pna2_1$ unit cell. While $CsAlSiO_4$ pattern of samples treated at 900 – 1050 °C matched with ICDD 00-047-0471 with $Ia\bar{3}d$ unit cell. This observation contradicts the study of (Diego Gatta *et al.*, 2012) which concluded that the $CsAlSiO_4$ crystal structure is stable up to 1000 °C. Another experimental study may be needed to confirm this issue. Even so, $CsAlSiO_4$ is a strong candidate as the immobilizer matrix for the radioactive waste (Taylor, DeVaal and Owen, 1989; Diego Gatta *et al.*, 2012; Yang *et al.*, 2017; Jeon *et al.*, 2019).

Besides the peaks which are identified as $CsAlSiO_4$, several smaller peaks indicate the presence of other compounds. Some small peaks strongly related to $CsAlO_2$ are identified from all specimens treated at all temperatures. The intensity of $CsAlO_2$-related peaks is relatively high from the simulated Cs compound of X-750 compared with the other, indicating it is available in abundance. A relatively high abundance of $CsAlO_2$ in Si-lack specimens should be related to the stability of the compound. $CsAlSiO_4$ is more stable compared with $CsAlO_2$ as can also be identified from their energy formation. Energy formation of $CsAlSiO_4$ with $Pna2_1$ unit cells is about -3.197 eV while $CsAlO_2$ is

about -2.852 eV (Jain *et al.*, 2013). In the other words, the existence of Si tends to encourage the formation of $CsAlSiO_4$ rather than $CsAlO_2$.

The presence of Ti opens the possibility of the $CsAlTiO_4$ formation. Energy formation of $CsAlTiO_4$ is about -3.231 eV (Jain *et al.*, 2013). This formation is theoretically more stable compared with $CsAlSiO_4$ as well as $CsAlO_2$. Because of that, $CsAlTiO_4$ can be observed from all specimens except from simulated Cs compounds in Ti-deficient SS 304.

Besides those compounds which can be observed from all temperature treatments, there are several peaks, especially at lower temperature treatments that must be related to the other compounds. Those peaks are probably related to $Cs_2Si_2O_5$, $Cs_2Al(OH)SiO_4)_2$, $Cs_2(Al_2O(OH)_6)$, and $Cs_2TiO_4{\cdot}H_2O$. $Cs_2Al(OH)SiO_4)_2$ is identified from simulated Cs compounds in SS 304, SS 321, and Inconel 600 which consist of relatively rich Si. $Cs_2TiO_4{\cdot}H_2O$ is identified from simulated Cs compounds in SS 321 and X-750 which are rich in Ti. While $Cs_2(Al_2O(OH)_6)$-related peaks only can be observed from simulated Cs compounds in X-750 which consist of relatively rich Al. These compound formation differences indicate that $Cs_2Al(OH)SiO_4)_2$ should be more stable compared with $Cs_2TiO_4{\cdot}H_2O$ and $Cs_2(Al_2O(OH)_6)$.

5.4 Summary

Cs may react with several elements, especially Fe, Cr, Al, Ti, and Si to form such kinds of compounds. Due to their high availability in both SS and Inconel, cesium iron oxides and cesium chromium oxides in the form of Cs_2FeO_4, $CsFeO_{2.5}$, and Cs_2CrO_4 can be formed largely. It's just that these compounds are easily dissolved in water. While Cs-Al-Ti-Si-O compounds are found to be well-chemisorbed starting at low temperatures. From cross-sectional SEM/EDS observations of all materials, Cs can be found to be chemisorbed in the oxide layer with several variations. Cs-rich areas containing Si and Fe in SS 304 can be found alongside the outer oxide layer and concentrated especially between the outer and inner layers. Similar formation of Cs compounds, but also related to Ti are in/on the outer layer of SS 321, Inconel 600, and X-750. Although Ti can react with Cs and improve chemisorption on X-750, however, the ability of Ti to increase oxidation resistance affects the reduction of chemisorbed Cs. The fact that Cs can only

be found in the outer layer, indicates that Cs is not able to diffuse through the Cr-rich layer. The chemisorbed Cs in the oxide layer seems to be formed due to the growth mechanism of the outer layer.

Cs-Al-Ti-Si-O compounds which are observed as small particles on the surface of specimens are related to some main compounds depending on the elemental availability and the temperature treatment. The compounds in SS 304 treated at 300 - 600 °C are identified to be $CsAlSiO_4$, with the rest may relate to $Cs_2Al(OH)SiO_4)_2$, and $CsAlO_2$. While chemisorbed Cs compounds in SS 321 also relate to the same compounds but with an additional $CsAlTiO_4$ and $Cs_2TiO_4{\cdot}H_2O$ compounds. $CsAlSiO_4$, $Cs_2Al(OH)SiO_4)_2$, $CsAlTiO_4$ and $CsAlO_2$ are also expected from Inconel 600. Nevertheless, due to the lack of Si in X-750, only $CsAlTiO_4$, $CsAlO_2$, $Cs_2TiO_4{\cdot}H_2O$, and $Cs_2(Al_2O(OH)_6)$ are expected at lower temperature treatment. However, at higher temperatures, $Cs_2Al(OH)SiO_4)_2$, $Cs_2TiO_4{\cdot}H_2O$, and $Cs_2(Al_2O(OH)_6)$ compounds are decomposed and leaving $CsAlSiO_4$, $CsAlO_2$, and $CsAlTiO_4$ with the abundance depending on the elemental availability in each respective material.

5.5 References

Allen, G. C. et al. (1987) 'Surface studies of the interaction of cesium hydroxide vapor with 304 stainless steel', Oxidation of Metals, 28(1–2), pp. 33–59. doi: 10.1007/BF00666470.

Callister, W. D. and Rethwisch, D. G. (2013) Materials Science and Engineering 9th Edition. 9th Edition, Wiley. 9th Edition. Wiley. doi: 10.1016/j.str.2011.03.005.

Chang, S. J. et al. (1992) 'Corrosion of Austenitic Stainless Steel in Steam Containing Cesium Hydroxide', Journal of Nuclear Science and Technology, 29(8), pp. 753–761. doi: 10.3327/jnst.29.753.

Diego Gatta, G. et al. (2012) 'Phase stability and thermo-elastic behavior of CsAlSiO4 (ABW): A potential nuclear waste disposal material', Microporous and Mesoporous Materials, 163, pp. 147–152. doi: 10.1016/j.micromeso.2012.07.010.

Jain, A. et al. (2013) 'Commentary: The materials project: A materials genome approach to accelerating materials innovation', APL Materials, 1(1). doi: 10.1063/1.4812323.

Jeon, S. C. et al. (2019) ‘A comparative study on the cesium retention ability up to 1750 °C in Cs–Zr–Si–O, Cs–Al–Si–O, and Cs–Si–O’, Ceramics International. Elsevier Ltd and Techna Group S.r.l., 45(12), pp. 15754–15757. doi: 10.1016/j.ceramint.2019.05.038.

Kobata, M. et al. (2018) ‘Chemical form analysis of reaction products in Cs-adsorption on stainless steel by means of HAXPES and SEM/EDX’, Journal of Nuclear Materials. Elsevier B.V, 498, pp. 387–394. doi: 10.1016/j.jnucmat.2017.10.035.

Di Lemma, F. G. et al. (2017) ‘Experimental investigation of the influence of Mo contained in stainless steel on Cs chemisorption behavior’, Journal of Nuclear Materials, 484, pp. 174–182. doi: 10.1016/j.jnucmat.2016.11.031.

Miradji F.; et al. (2019) ‘Modelling of Cesium Chemisorption Under Nuclear Power Plant Severe Accident Conditions’, in The 9TH European Review Meeting on Severe Accident Research (ERMSAR2019). Prague.

Nakajima, K. et al. (2018) ‘An experimental investigation for atmospheric effects on Cs chemisorption onto stainless steel’, Progress in Nuclear Science and Technology, 5(0), pp. 168–170. doi: 10.15669/pnst.5.168.

Nakajima, K. et al. (2019) ‘Study on chemisorption model of cesium hydroxide onto stainless steel type 304’, International Conference on Nuclear Engineering, Proceedings, ICONE, 2019-May. doi: 10.1299/mej.19-00564.

Noguchi, M. and Yakuwa, H. (2016) ‘Lecture on Fundamental Aspects of High Temperature Corrosion and Corrosion Protection Part 1: Basic Theory’. Ebara Engineering Review, pp. 1–11. Available at: https://www.ebara.co.jp/about/technologies/abstract/detail/__icsFiles/afieldfile/2017/03/08/252_P31_1.pdf.

Osaka, M. et al. (2016) Results and Progress of Fundamental Research on Fission Product Chemistry - Progress Report in 2015. Tokai-mura. doi: 10.11484/jaea-review-2016-026.

Roki, F. Z. et al. (2008) ‘Thermodynamic study of the CsOH(s,l) vaporization by high temperature mass spectrometry’, The Journal of Chemical Thermodynamics, 40(3), pp. 401–416. doi: 10.1016/j.jct.2007.09.013.

Saĭto, M., Otšuka, K. and Furuya, H. (1983) ‘Penetration Behavior of Cesium in Oxide Film Growing on Surface of Stainless Steel under Condition of High Oxygen

Potential', Journal of Nuclear Science and Technology, 20(1), pp. 30–35. doi: 10.3327/jnst.20.30.

Stratton, P. (2013) 'Ellingham diagrams - their use and misuse', International Heat Treatment and Surface Engineering, 7(2), pp. 70–73. doi: 10.1179/1749514813Z.00000000053.

Taylor, P., DeVaal, S. D. and Owen, D. G. (1989) 'Stability relationships between solid cesium aluminosilicates in aqueous solutions at 200 °C', Canadian Journal of Chemistry, 67(1), pp. 76–81. doi: 10.1139/v89-013.

Walton, K. L. et al. (2014) 'Adsorption of iodine on graphite in High Temperature Gas-Cooled Reactor systems: A review', Progress in Nuclear Energy. Elsevier Ltd, 73, pp. 21–50. doi: 10.1016/j.pnucene.2014.01.005.

Warlimont, H. (2003) Titanium and Titanium Alloys, Springer Handbooks. Edited by C. Leyens and M. Peters. Cologne: Wiley. doi: 10.1002/3527602119.

Wei gao, Z. L. (2008) Developments in high-temperature corrosion and protection of materials. Edited by W. Gao and Zhengwei Li. Corwall: Woodhead Publishing Limited. Available at: https://www.sciencedirect.com/book/9781845692193/developments-in-high-temperature-corrosion-and-protection-of-materials.

Yakuwa, H. and Noguchi, M. (2017) 'Lecture on Fundamental Aspects of High Temperature Corrosion and Corrosion Protection Part 2: Corrosion Protection and Coatings', Ebara Engineering Review, (252), pp. 1–12.

Yang, J. H. et al. (2017) 'A new route to the stable capture and final immobilization of radioactive cesium', Journal of Hazardous Materials. Elsevier B.V., 339, pp. 73–81. doi: 10.1016/j.jhazmat.2017.05.062.

Chapter 6

Summary and Conclusion

(This page intentionally left blank)

Science, my lad, is made up of mistakes, but they are mistakes which it is useful to make because they lead little by little to the truth.

~Jules Verne

(This page intentionally left blank)

Chapter 6

Summary & Conclusion

6.1 Summary

Understanding source terms transport behavior is important both for normal operation and severe accident conditions of nuclear reactors. Source terms transport for each nuclear reactor vary, depending on the type of reactors and scenarios. Source terms transport of LWR, especially during a severe accident, has been well modeled. Nevertheless, chemistry is identified to contribute to the large modeling uncertainty. Several studies related to the chemistry aspect of source terms have been done for uncertainty improvement. Cs becomes one of the most interesting studies due to its abundance, long-half life, and volatility. Cs can react with some minor elements such as B, Mo, and Si which affect their volatility. Several Cs compounds are observed to be chemisorbed on the structural materials and largely influence their volatilities. Besides related some minor elements, Cs chemistry largely depends on the temperature. Several Cs chemisorption studies following gas phase and solid structural materials interaction at elevated temperatures have been done. Gaseous phase interaction of Cs with structural materials is important for the source terms transport prediction just after an accident. JAEA has succeeded in developing a chemical database based on several gas-phase interactions to increase the accuracy of severe accident prediction. However, insufficient knowledge exists related to liquid-solid interaction, especially at lower temperatures. Liquid-solid interaction phenomena are important to consider the decontamination factor through the leakage to the environment. These phenomena are important during the decommissioning period.

Generally, the effect of pre-oxide film on Cs chemisorption during gas-solid interaction is ruled out. Pre-oxide film's effect can be ruled out for the Cs release just after the accident because it should be thin and difficult to predict. However, the oxide film growth may become thick and stable after some period. On the other hand, the growth of oxide film is strongly related to the type of materials. Materials with different base and solute elements have oxide film characteristic variation. Those variations include the oxide film thickness, roughness, strength, as well as its oxides species. Species of oxide

directly interact with Cs source terms. That interaction may end up with the formation of new Cs compounds, that are strongly chemisorbed. It means besides contributing to the oxidation; elements of materials may also directly contribute to the Cs chemisorption.

By considering the abovementioned, this study aims to investigate the effect of oxidation related to solute elements on the Cs chemisorption behavior of nuclear structural materials by following a liquid-solid reaction. A new simplified method to simulate liquid Cs interaction with solid structural materials with the various pre-oxide films is developed. The method consisted of some main steps, starting from specimen selection and preparation, Cs exposure, and stability testing. Several specimens with various oxide films are prepared from well-polished SS 304, SS 321, Inconel 600, and X-750 materials controlled by temperature. These prepared specimens are then exposed to CsOH following a unique temperature setting on the furnace with an air environment without any flow. Cs exposure is started by dividing the specimens into 6 groups depending on the temperature treatment (300, 450, 600, 750, 900, and 1050 °C) for pre-oxide film growth. Each group consists of unoxidized specimens from each material and oxidized specimens from each annealing temperature. Around 0.5 g CsOH is carefully measured and placed directly on each group of specimens then put in the furnace. The temperature of the furnace is set to increase from RT to CsOH melting point (272 °C) for 30 minutes and maintained for 1 hour. The temperature is then increased again to the respective point depending on their group, which is like the pre-oxidation temperatures for 30 minutes and maintained for 6 hours. These specimens are furthermore soaked in the distilled water and ethanol using an ultrasonic cleaner for 180 seconds respectively then dipped in acetone for 2 seconds to remove any soluble compounds and impurities. The specimens are characterized for each step mainly using OM, XRD, and SEM/EDS for surface and cross-sectional observations. However, it must be noted that temperature treatment differences contribute to the reaction times and precursor availability variation. Based on preliminary tests, almost similar reaction times and CsOH availability are expected from specimens treated at 300, 450, and 600 °C. Reaction time still lasts for 6 hours at 750 °C and 900 °C, but only with CsOH availability of around 73.61% and 31.60% respectively. While for 1050 °C, the solid Cs reaction with the specimens lasts just after reaching the target temperature.

Base and solute element differences between materials contribute to the pre-oxide film variation between prepared specimens. Generally, the fastest pre-oxide film growth is observed from SS 304, then followed by SS 321, Inconel 600, and X-750. Detailed pre-oxide conditions of these specimens can be explained as follows.

In SS 304, the oxide film after annealing at 300 °C is thin, and it gradually becomes thicker with the increasing annealing temperature. The oxide film becomes several hundred nanometers thick under annealing at 600 °C and ~6 µm-thick under annealing at 900 °C. Chromium oxides and some spinel of Fe-Cr-Ni-Mn-O exist in the inner layer, while oxides of Fe, Ni, Cr, Mn, Al, and Si exist in the outer layer. The formation of silicon oxides is observed in some regions—particularly in grain boundary-like areas between the base material and the oxide layer, including between the inner and outer oxide layers. Thick and fragile oxide layers, up to ~700 µm, dominated by the formation of iron oxides, nickel-iron oxides, and iron-chromium oxides are observed from specimens annealed at 1050 °C.

SS 321 is developed to get better oxidation-resistant material compared to SS 304. A thin oxide layer that can be identified using Optical Microscope (OM) exists in both materials annealed at 300 °C. Subtle chromium oxide particles beside iron oxides compose the surface of the specimen annealed at 450 °C. Both specimens annealed at 600 and 450 °C are similar except for a coarser surface. Titanium oxide particles in the iron oxide-dominated areas appear from SS 321 annealed at 900 °C. Oxides layers of SS 321 annealed at 1050 °C are still robust, even though they have lost their Ti formation. While silicon oxides fill the grain boundary-like cracks and between the inner and outer layers.

In Inconel 600, after the pre-oxidation process, the oxides of Ni, Fe, and Cr are observed at 300 °C. Rich and thick oxide films consist of mainly chromium oxides, which exist as the inner layer, and oxides of Ni, Fe, Cr, Mn, Ti, Al, and Si exist as the outer layer. Explosion-like cracks containing a Ti formation below the oxide layer with a thickness of ~5 µm are observed—particularly from specimens annealed at 900 °C. A similar formation is observed at 1050 °C, but the oxide film is 5–6 times thicker and has a rougher surface.

Oxide formation of X-750 after the pre-oxidation process cannot be identified at 300 °C. Appropriate oxidation dominated by nickel oxides, chromium oxides, and iron oxides is observed from specimens annealed at 450 °C, which grows gradually in line

with the annealing temperature. From specimens annealed at 600 – 900 °C, X-750 exhibits robust oxide formation dominated by chromium titanium oxides and chromium oxides, with grain boundary-like formations as well as Al-Ti-O on the surface. The oxide-film formation of X-750 annealed at 1050 °C is robust, although the thickness increased to ~18 µm.

Specimens' characterization just after being exposed to CsOH indicates several things. The first indicator that can be observed easily is related to the oxidation acceleration. That oxidation acceleration is caused by the highly corrosive CsOH as previously also observed by (Chang *et al.*, 1992). Besides accelerating the oxidation, Cs is also observed to react mainly with Fe and Cr starting from 300 °C treated temperature but without indication to react with Ni. Cesium iron oxides in the form of Cs_2FeO_4 are detected from specimens treated at 300 to 600 °C. While cesium chromium oxides in the form of Cs_2CrO_4 are detected from all treated temperatures except at 1050 °C. The other Cs compounds that are strongly related to Al, Ti, and Si also exist as indicated by SEM/EDS observation. However, due to their measly amounts, these compounds cannot be detected by XRD. Interestingly, the Cs amount on the surface of oxidized specimens is consistently high compared with unoxidized specimens. That phenomenon proves the significance of the pre-oxide film to the Cs chemisorption.

Post-soaked specimens' characterization indicates both cesium iron oxides and cesium chromium oxides are highly water-soluble. The dissolution of those compounds is also followed by the partial erosion of the outer oxide layer, which is indicated by the oxide thickness reduction. Nevertheless, a small amount of Cs compounds remain and are chemisorbed in the oxide film. Cs particles containing Al and some also with Si are retained in the surface of SS 304 specimens treated at 300 and 450 °C. While in SS 321, Inconel 600, and X-750, these Cs particles are also related to Ti. Chemical compounds of these small particles are difficult to be identified directly using currently utilized techniques. Therefore, additional tests to simulate these small particles are conducted by reacting Al_2O_3, SiO_2, TiO_2, and $CsOH{\cdot}H_2O$. All these precursors are mixed with average atomic ratios of Cs particles observed by EDS point analysis and then treated in the same environment as the main experiment. As a result, the compounds in SS 304 are predicted mainly related to $CsAlSiO_4$, while the rest should be $CsAlO_2$, including $Cs_2Al(OH)SiO_4)_2$. XRD patterns of simulated Cs compounds in SS 321 and Inconel 600 are almost similar

except for their intensities, indicating the existence of similar compounds. Cs compounds in SS 321 are predicted to be the same as SS 304 with additional $CsAlTiO_4$, and $Cs_2TiO_4 \cdot H_2O$. Simulated Cs particles in Inconel 600 are like SS 321 but in the absence of $Cs_2TiO_4 \cdot H_2O$. While XRD peaks of X-750 are largely different due to the limited amount of Si. Most of the peaks of simulated Cs particles in X-750 are related to $CsAlO_2$ and $CsAlTiO_4$, with the rest related to $Cs_2TiO_4 \cdot H_2O$ and $Cs_2(Al_2O(OH)_6)$. These small particles which are stuck on the surface cannot be observed at 600 and 750 °C despite still showing similar overlapping tendencies. Surface SEM/EDS observation shows Cs elements are spread alongside oxide formation and overlap with Al, (including Ti in the case of SS 321, Inconel 600, and X-750) and some with Si. The trend changes when the specimens are treated at 900 and 1050 °C, where most of the Cs elements overlap with Si. By following the same approach which is used to predict retained compounds at lower temperatures, different Cs species are also identified at higher temperatures. $CsAlSiO_4$ is expected from all specimens but mostly within the different space groups between specimens treated at 300 – 750 °C and 900 – 1050 °C. The space group of $CsAlSiO_4$ treated at lower temperatures is $Pna2_1$, and became $Ia\bar{3}d$ when treated at 900 – 1050 °C. Some compounds identified at lower temperatures such as $Cs_2Al(OH)SiO_4)_2$, $Cs_2TiO_4 \cdot H_2O$, and $Cs_2(Al_2O(OH)_6)$ are decomposed at higher temperatures leaving $CsAlSiO_4$, $CsAlTiO_4$ and $CsAlO_2$.

Oxidation directly contributes to the Cs chemisorption. A comparison between unoxidized specimens and oxidized specimens that are exposed to CsOH shows the amount of Cs retained in the oxidized specimens is consistently higher compared with unoxidized specimens at all temperature treatments. A higher amount of Cs in oxidized specimens is related to oxide element availability, particularly oxide of Fe, Cr, Al, Ti, and Si. These oxides should be higher in oxidized specimens than that in unoxidized specimens. Cs chemisorption has an inverse correlation with oxidation-resistant properties. The highest amount of Cs is observed to be chemisorbed in SS 304, followed by SS 321, X-750, and Inconel 600 at all respective temperatures. Nevertheless, the amount of Cs in X-750 is higher compared with it in Inconel 600, despite having better oxidation resistance. This abnormality is raised due to a much higher amount of Ti on the surface of X-750 which triggers the formation of well-chemisorbed cesium titanates.

6.2 Concluding Remarks

The present study contributes to the Cs chemisorption understanding improvement, especially related to liquid-solid interaction that commonly happens particularly at lower temperatures areas in the leakage parts to the environment by using a novel method. Although the novel method is relatively simple, it is capable to simulate liquid-solid interaction at low temperatures and replicate some Cs chemisorption phenomena that are observed at high temperatures using conventional gas-solid interaction methods.

This study shows the importance of oxidation, which is directly correlated to the Cs chemisorption ability. To the best of the author's knowledge, the effect of oxidation has not been previously explored in detail. Thus, this study provides a new perspective on understanding Cs chemisorption by involving oxidation factors in addition to the influence of solute elements. Besides Si which has been well-known, solutes Al and Ti are confirmed could increase the amount of chemisorbed Cs elements. However, they also contribute to the oxidation resistance improvement which could reduce Cs chemisorption.

Cs element is observed to react mainly with Fe, Cr, Al, Ti, and Si to form several compounds. Cs_2FeO_4, $CsFeO_{2.5}$, and Cs_2CrO_4 are confirmed to be formed but easily dissolved in water. Cs-Al-(Ti)-(Fe)-Si-O chemical systems are well-chemisorbed on the specimens with the species depending on the temperature treatments and elemental availability. Some possible compounds that are observed at 300 – 450 °C, such as $CsAlSiO_4$, $CsAlO_2$, $CsAlTiO_4$, $Cs_2Al(OH)(SiO_4)_2$, $Cs_2TiO_4{\cdot}H_2O$ and $Cs_2(Al_2O(OH)_6)$. $CsAlSiO_4$, $CsAlTiO_4$ and $CsAlO_2$ (in case of Si deficiency) are found to be stable and exist up to 1050 °C.

6.3 Future Recommendation

Characterization in this study is conducted using relatively simple techniques which can contribute to some uncertainties. The quantification of elements in this study is carried out with EDS which has a detection limit of about 0.15 – 0.20 at.%. Some elements under certain conditions are characterized in the detection limit range and even lower. This indicates that several quantifications have a low level of accuracy. Therefore, future

experiments using better accuracy measurements such as WDS may be needed. Compounds formation in this study is mainly identified using XRD supported by SEM/EDS and OM. Although XRD is one of the best techniques for crystal identification, errors may occur due to the difficulty of identifying multi-crystal compounds especially related to the compounds which have isomorphic crystal structures. Therefore, validation using other techniques such as Raman spectra, TEM, etc. is needed to increase the confidence level of the results.

The thermodynamics data of some compounds identified in this study are still not well understood, i.e., related to the Cs-Fe-O system. Thermodynamic data of these compounds are important to improve source terms chemistry database. Therefore, further studies can be carried out by identifying the thermodynamic character of these compounds both experimentally and/or theoretically i.e., through quantum chemistry calculation.

(This page intentionally left blank)

Appendix

(This page intentionally left blank)

Appendix A

CsOH Precursor Residual and Its Reaction Times

A. Background

Evaporation of CsOH occurs from the low temperatures at a rate dependent on the evaporation pressure. Evaporation pressure generally increases with temperature. The difference in evaporation rate greatly affects the availability of CsOH on the surface of the specimens including its reaction time. Generally, differences in the availability of CsOH and reaction time can affect the type of compound that might be formed.

The change of CsOH from liquid to gas through the evaporation process, especially at high temperatures, may also change the type of chemical reaction. Because this study focuses on liquid-solid reactions, it is necessary to determine the type of reaction at each temperature. These preliminary test results are useful to avoid errors during analysis.

B. Procedure

Preliminary tests are conducted using similar apparatus and methods to those intended for the main experiment.

Reaction times and Cs availability are predicted by putting ~2 g of CsOH precursor on the Pt plate and then treating at some target temperatures (in this test only at 600, 750, 900, and 1050 °C) for 6 hours. Mass of CsOH is measured during heating periodically every 1 minute for the first 15 minutes, every 10 minutes for the first 1 h, and then every 1 h.

Due to the high evaporation rate at 1050 °C, the effect of gas-solid reaction at this temperature is tested by comparing 2 dummy specimens made by well-polished SS 304. The first specimen is coated with CsOH and the second specimen without CsOH coating. The uncoated specimen is set at about 10 mm neighborhood of Pt crucible containing 0.5 g CsOH as illustrated in Figure A.1. Both coated and uncoated specimens with separated CsOH are then treated at 1050 °C in an air environment without any flow. The specimens furthermore are observed using surface SEM/EDS.

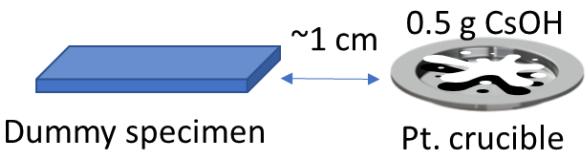

Figure A.1. Effect of gas-solid interaction identification from the utilized heater at 1050 °C temperature treatment.

TG-DTA analysis for CsOH precursors is also conducted in the air environment with a heating speed of 5 °C/minute between RT to 1050 °C.

C. Results

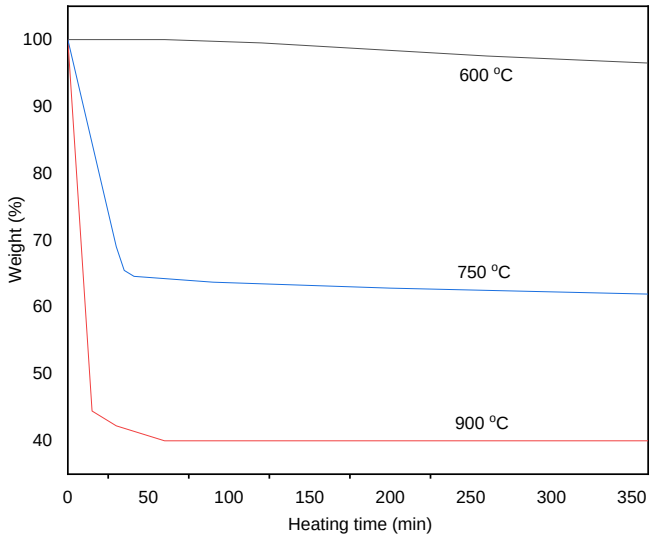

Figure A.2. Remain CsOH on the Pt plate when treated at 600, 750, and 900°C.

As shown in Figure A.2, the weight of CsOH precursor residual is measured at more than 92% when treated at 600 ºC while only ~36% and ~24% when treated at 750 ºC and 900 ºC for 6 hours respectively, and it was completely evaporated just a minute after reaching 1050 ºC. However, it should be noted that these percentages also include surface water and hydride contents of $CsOH{\cdot}H_2O$. TG-DTA furthermore is conducted to provide detailed characteristics of the $CsOH{\cdot}H_2O$ precursor.

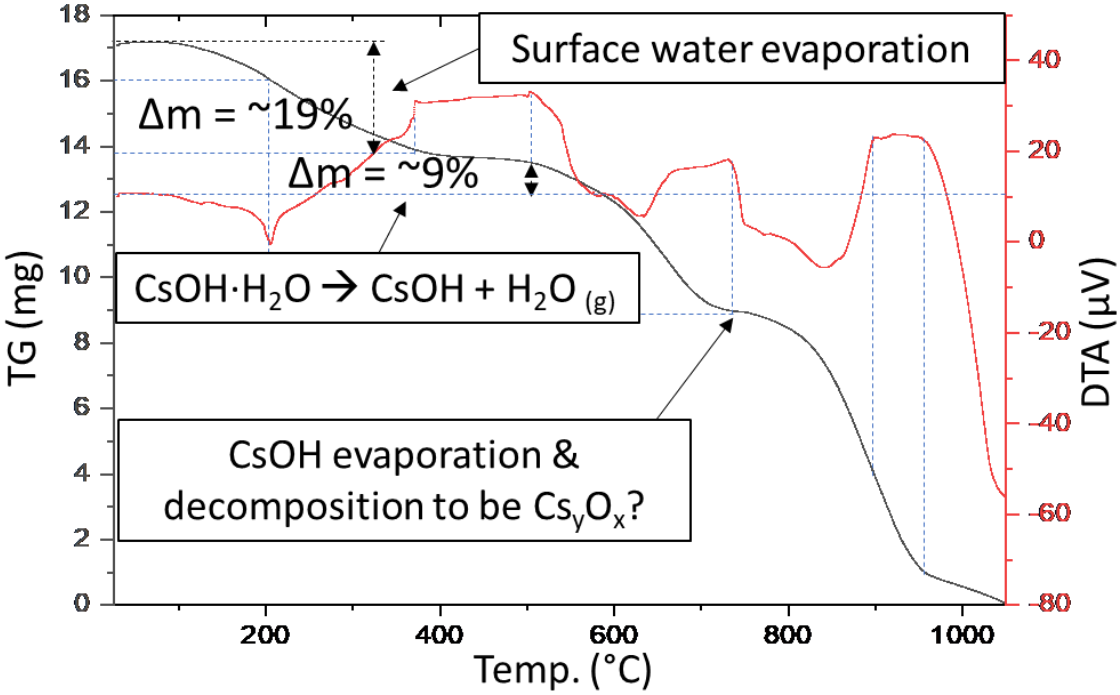

Figure A.3. TG-DTA analysis of $CsOH{\cdot}H_2O$ precursor

TG-DTA analysis of CsOH precursor as shown in Figure A.3 indicates some physical and chemical phenomena during the heating treatment that could correct rough estimation as shown in Figure A.2. Water evaporation is detected from CsOH precursors treated at 100 – 372 °C indicating the release of surface water caused by hygroscopicity of the precursor. At 500 – 670 °C, the $CsOH{\cdot}H_2O$ precursor is decomposed to be CsOH. While starting from 730 °C CsOH is rapidly decomposed and evaporated. From TG-DTA, it can be said that almost 100% of Cs are still present on the surface when the specimens were treated at 300 – 600 °C. However rapid Cs evaporation is expected when specimens are treated at 750 °C and above. Because of that, although rough measurement as shown in Figure A.2 indicates the weight of CsOH precursor treated at 600 °C is reduced to be ~92%, however, the weight reduction is related to moisture evaporation with the Cs evaporation rate could be ruled out. So, it can be said that the amount of Cs on the specimens treated at 300 – 600 °C should be almost 100 % during 6 hours of reaction time. The same reaction time is also happening when specimens are treated at 750 °C and 900 °C, but with different Cs reactant residuals. Cs residual of 750 °C and 900 °C treatment is calculated to be 73.61% and 31.60% respectively. While at 1050 °C, the liquid-solid reaction only happens in a relatively short period, around 1 hour during the

coating process, 0.5 hours transition period from coating to 1050 °C, and just after reaching the target temperature.

Characterization of Cs retention on dummy specimens as shown in Figure A.3 indicates Cs cannot be detected on uncoated dummy specimens. While some Cs particles can be observed from CsOH coated specimens. That test indicated gas-solid interaction is limited due to the large volume of the furnace.

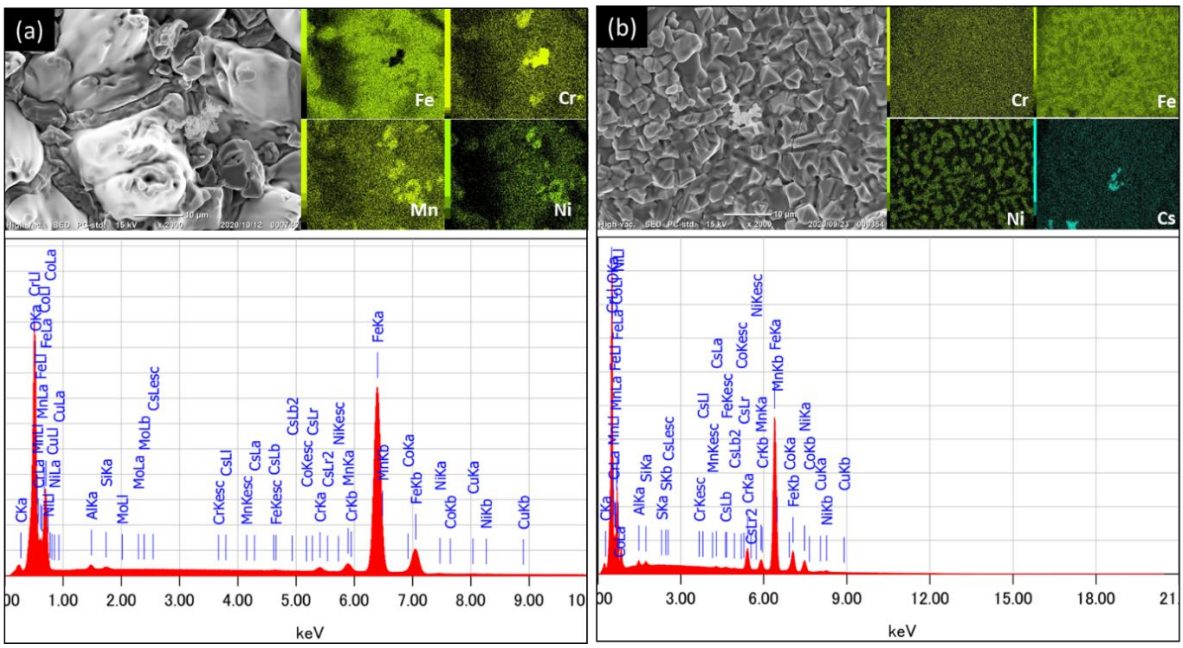

Figure A.4. Surface SEM/EDS observation of (a) uncoated and (b) CsOH-coated specimens.

Appendix B

Thermal Characteristics of Fe_3O_4 and Cr_2O_3 Precursor

A. Background

Fe_3O_4 and Cr_2O_3 are used to do analytical experiments during the additional tests of Cs-Fe-Cr-O compounds. Both precursors are reacted with the CsOH precursor during the analytical test. However, a part of them might remain and chemically change with the temperature during the annealing process. Physicochemical changing identification that may occur could be important to minimize the errors during the XRD analysis.

B. Procedure

Identification is performed by following 2 techniques, XRD analysis, and TG-DTA.

Specimens for XRD analysis are prepared under 3 conditions, measuring as received Fe_3O_4 and Cr_2O_3 without any treatment, and annealing procedure at 750 and 1050 °C for 6 hours on the air in the same environment as the main experiment. These specimens are then measured and analyzed to identify the chemical compounds changing that might be happening.

TG-DTA is performed to identify the detailed physical and chemical transformation according to temperature changes. As received Fe_3O_4 and Cr_2O_3 are analyzed in TG-DTA on the air environment with a heating rate of 5 °C/minutes.

C. Results

As shown in Figure B.1, XRD analysis of Fe_3O_4 which matches with ICDD 01-088-0315, indicates that this compound is oxidized to be Fe_2O_3 which matches with ICDD 01-084-0307 when heated at 750 and 1050 °C. A more detailed oxidation mechanism of Fe_3O_4 furthermore can be observed from TG-DTA as shown in Figure B.2. Mass of Fe_3O_4 increased starting from ~140 °C and became stable at ~ 570 °C when all Fe_3O_4 transformed to be Fe_2O_3 by absorbing oxygen following an exothermic reaction.

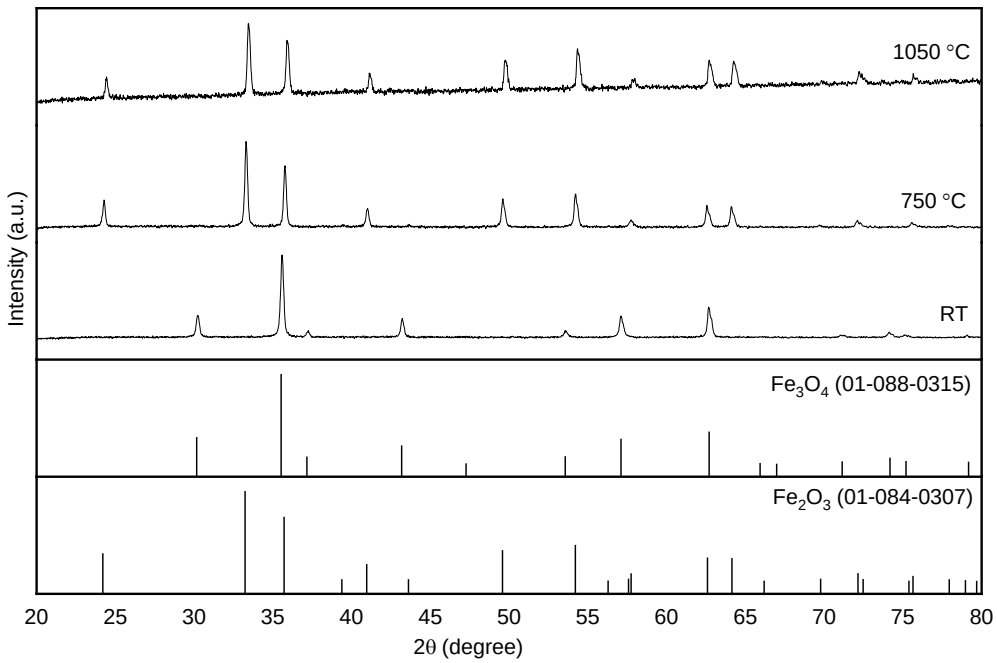

Figure B.1 XRD analysis indicating the oxidation of Fe_3O_4 when heated at 750 and 1050 °C in the air environment

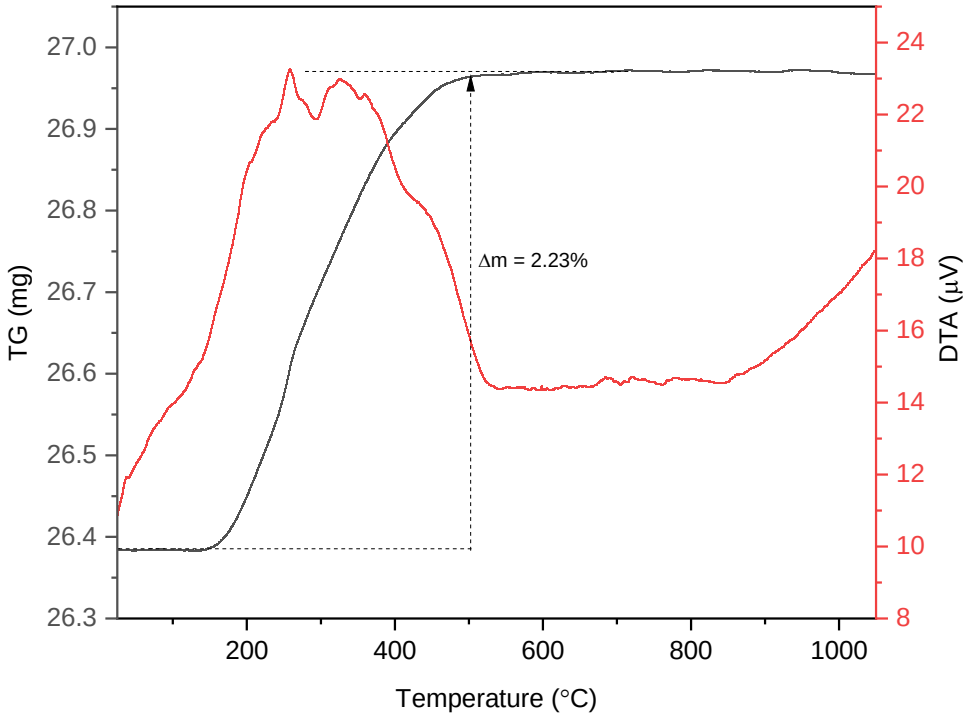

Figure B.2. TG-DTA analysis indicates Fe_3O_4 is oxidized to be Fe_2O_3, starting from 150 ºC.

As shown in Figure B.3, Cr_2O_3 is stable and does not undergo chemical changes. XRD analysis of all Cr_2O_3 specimens annealed at RT, 750, and 1050 °C show the same patterns. All these patterns correspond to Cr_2O_3 which matches ICDD card number 01-

084-0321. TG-DTA measurement for Cr_2O_3 is also conducted and it is concluded that Cr_2O_3 does not experience physical change.

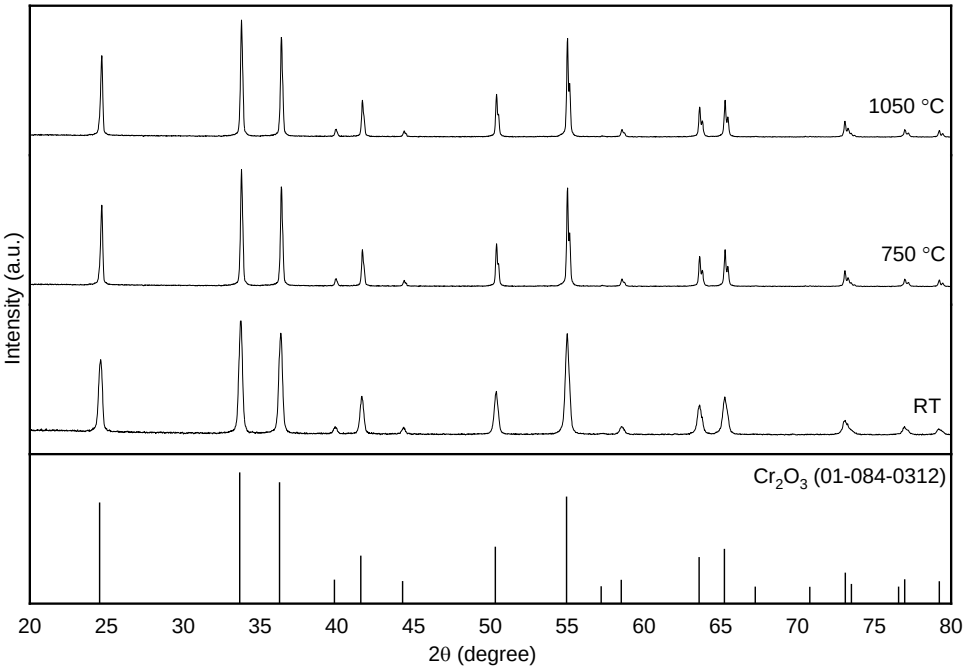

Figure B3. XRD analysis indicates the chemical compound of Cr_2O_3 precursor is not changed when annealed up to 1050 ºC in an open-air environment.

-END-